Titre: Title:	Investigation of Different Numerical Modellings of Transient Flows in Storm Water Systems
Auteur: Author:	Ilian Tosan
Date:	2021
Type:	Mémoire ou thèse / Dissertation or Thesis
Référence: Citation:	Tosan, I. (2021). Investigation of Different Numerical Modellings of Transient Flows in Storm Water Systems [Mémoire de maîtrise, Polytechnique Montréal]. PolyPublie. https://publications.polymtl.ca/5622/

URL de PolyPublie: PolyPublie URL:	https://publications.polymtl.ca/5622/
Directeurs de recherche: Advisors:	Musandji Fuamba
Programme: Program:	Génie civil

POLYTECHNIQUE MONTRÉAL

affiliée à l'Université de Montréal

Investigation of different numerical modellings of transient flows in storm water systems

ILIAN TOSAN

Département des génies civil, géologique et des mines

Mémoire présenté en vue de l'obtention du diplôme de *maîtrise ès sciences appliquées*

Génie civil

Mars 2021

POLYTECHNIQUE MONTRÉAL

affiliée à l'Université de Montréal

Ce mémoire intitulé:

Investigation of different numerical modellings of transient flows in storm water systems

présenté par **Ilian TOSAN**

en vue de l'obtention du diplôme de *Maîtrise ès sciences appliquées*

a été dûment accepté par le jury d'examen constitué de :

MAHDI TewFik, président

FUAMBA Musandji, membre et directeur de recherche

SHAKIBAEINIA Ahmad, membre

ACKNOWLEDGEMENTS

I thank my director of research Dr., Professor, Musandji Fuamba for proposing me this interesting and challenging topic of transient flows and supervising me during this project. I am also grateful for his interest in me, his listening skills, his numerous offers for various projects, the several letters of recommendation he wrote me.

I would also like to express my gratitude to Arman Rokhzadi for his incredible help during my Master of research and the countless advice he gave me.

I include Rolando-Yezid Perez-Pulido in my acknowledgements because it was a pleasure to work with him.

Finally, I thank my family and any person who supported me in my various endeavours during my life.

RÉSUMÉ

Le transport des eaux pluviales dans des conditions de surface libre est le but des systèmes d'eaux pluviales (SWS). La nature du remplissage rapide des SWS ou de la maintenance aux limites peut conduire à la propagation des ondes et à l'altération de l'écoulement à surface libre en un écoulement partiellement pressurisé et au piégeage des poches d'air qui peuvent alors conduire à de graves problèmes tels que des geysers, des dommages aux infrastructures publiques et privées, des explosions de regards de recouvrement, des débordements, des inondations de rues, des accidents de la circulation, de graves problèmes électriques, etc. Afin de prévoir avec précision ces types de problèmes et de prévenir de telles conséquences causées par des flux transitoires, les modèles mathématiques doivent être améliorés et la modélisation numérique est désormais devenue incontournable.

L'objectif principal de ce projet est d'étudier des modèles numériques d'écoulements transitoires suivis du piégeage des poches d'air dans les SWS. L'étude de cas est la même tout au long du projet et il s'agit d'une conduite reliée à un réservoir à l'extrémité amont et en contact avec l'air atmosphérique à l'extrémité aval. Une partie amont du tuyau contient un écoulement sous pression et le reste contient un écoulement à surface libre. L'extrémité aval est fermée soudainement par une valve et la poche d'air est formée et piégée.

Tout d'abord, afin d'analyser la contribution du terme de perte par frottement, les modèles populaires de la colonne rigide et de la méthode des caractéristiques, sont utilisés avec un coefficient de frottement en régime permanent d'une part et avec un coefficient de frottement additionnel d'autre part. Les résultats numériques ont été comparés à des données expérimentales issues des essais réalisés au laboratoire d'hydraulique de l'École Polytechnique de Montréal ou de la littérature. Les modèles de la colonne rigide et de la méthode des caractéristiques avec le facteur de frottement de Darcy-Weisbach en régime permanent surestiment les pics de pression et ne capturent pas l'atténuation de la pression avec précision. Ensuite, la calibration du coefficient de frottement additionnel, qui est ajouté au facteur de frottement en régime permanent est discutée et il sera montré que le facteur de frottement additionnel calibré permet d'améliorer les résultats numériques.

Dans un second temps, l'approche d'amortissement, qui combine les équations du coup de bélier appliquées à l'écoulement sous pression et les équations de Saint-Venant appliquées à

l'écoulement à surface libre, est étudiée en simulation du même problème. L'approche d'amortissement avec l'application du facteur de frottement en régime permanent peut donner des résultats légèrement plus précis que ceux obtenus par les modèles de la colonne rigide et de la méthode des caractéristiques. Malheureusement, l'approche d'amortissement a une durée de simulation très longue, de sorte que la colonne rigide ou la méthode du modèle de caractéristiques est plus pratique pour modéliser le problème de piégeage des poches d'air. En outre, il a été constaté que les critères communs de pressurisation et de dépressurisation dans la méthode des volumes finis, qui sont basés sur la pression, provoquent une instabilité et peuvent conduire à un arrêt du programme. Au lieu de considérer des seuils de pression pour distinguer les parties à canal ouvert et sous pression de l'écoulement comme ce qui est fait dans la méthode des volumes finis proposée par León et al. (2010), l'approche d'amortissement proposée dans ce projet considère que le processus de pressurisation-dépressurisation est déterminé par la position de l'interface entre la surface libre et les écoulements sous pression. Ce critère basé sur le calcul de la position de l'interface évite un arrêt du programme et les instabilités survenues avec les critères communs basés sur des seuils.

Enfin, les modèles de la colonne rigide et de la méthode des caractéristiques appliqués avec le facteur de frottement en régime stationnaire seront implémentés dans le logiciel bien connu SWMM (Storm Water Management Model) pour ajouter l'option de simulation de piégeage de poches d'air à la liste des caractéristiques de ce logiciel. En effet, ces modèles sont capables de prédire les caractéristiques générales du problème telles que la pression de la poche d'air et le refoulement dans la canalisation. L'intérêt d'ajouter des modèles de piégeage des poches d'air dans SWMM est de mettre à niveau le logiciel populaire, qui ne peut pas actuellement modéliser le phénomène de piégeage des poches d'air.

Mots clés: Coups de bélier; Écoulements transitoires; Frottement non-permanent; Modèles numériques; Poche d’air emprisonnée.

ABSTRACT

Conveying storm water under free-surface conditions is the purpose of Storm Water Systems (SWSs). The nature of rapid filling in SWSs or maintenance at boundaries can lead to surge propagation and alteration of the free-surface flow to a partially pressurized flow and forming air pocket entrapment which can then lead to severe problems such as geysers, damage of public and private infrastructures, blowing off of covering manholes, overflows, street inundations, traffic accidents, severe electrical problems, and so forth. In order to accurately predict these kinds of problems and prevent such consequences caused by transient flows, mathematical models need to be improved and numerical modelling has now become unavoidable.

The main objective of this project is to study numerical models of transient flows followed by the air pocket entrapment in SWSs. The case study is the same all along the project and it is a pipe connected to a reservoir at the upstream end and has contact with the atmospheric air at the downstream end. An upstream part of the pipe contains a pressurized flow and the rest contains a free-surface flow. The downstream end is suddenly closed with a valve and the air pocket is formed and entrapped.

Firstly, in order to analyze the contribution of friction loss term, the common rigid column model and the method of characteristics model, are used with a steady-state friction factor on one hand and with an additional friction factor on the other hand. The numerical results were compared with experimental data which come from the tests carried out at the Hydraulics Laboratory of "École Polytechnique de Montreal" or from the literature. Both the rigid column and the method of characteristics model with the steady-state Darcy-Weisbach friction factor overestimate the pressure peaks and do not capture the pressure attenuation accurately. Then, calibration of an additional friction factor, which is added to the steady-state friction factor, is discussed and it will be shown that the calibrated additional friction factor allows to improve the numerical results.

Secondly, the shock-fitting approach, which combines the water hammer equations applied to the pressurized flow and Saint-Venant equations applied to the free-surface flow, is studied in simulation of the same problem. The shock-fitting approach with the application of the steady-state friction factor can give slightly more accurate results than those obtained by the models, the rigid column model, and the method of characteristics. Unfortunately, the shock-fitting approach has very long simulation duration so that the rigid column or the method of characteristics model

is more practical for modelling air pocket entrapment problem. In addition, it was found that the common criteria for pressurization and depressurization in Finite Volume method, which is based on pressure, causes instability and can lead to program abortion. Instead of considering pressure thresholds to distinguish the open-channel and pressurized portions of the flow like what is done in the finite volume method proposed by León et al. (2010), the shock-fitting approach proposed in this project considers that the pressurization-depressurization process is determined by the position of the interface between the free-surface and the pressurized flows. This criteria based on the calculation of the position of the interface prevents program abortion and instabilities that occurred with the common criteria based on thresholds.

Finally, the models, the rigid column and the method of characteristics models applied with the steady-state friction factor will be implemented in the well-known software SWMM (Storm Water Management Model) to add the air pocket entrapment simulation option to the list of features of this software. Indeed, these models are able to predict the general features of the problem such as the air pocket pressure and the discharge in the pipe. The interest in adding air pocket entrapment models in SWMM is to upgrade the popular software, which can currently not model the air pocket entrapment phenomenon.

Keywords: Air pocket entrapment; Numerical models; Pressure surges; Transient flows; Unsteady friction.

TABLE OF CONTENTS

LIST OF TABLES

LIST OF FIGURES

LIST OF SYMBOLS AND ABBREVIATIONS

A Cross-sectional area of the pipe

A_{flow} Cross-sectional flow area

A_0 Cross-sectional area of the orifice

A_1 Cross-sectional area of the free-surface zone

A_2 Cross-sectional area of the pressurized zone

a Speed of the pressure wave

a_{air} Air velocity

B Top water surface

C Calibration factor

C^+ Positive characteristic

C^- Negative characteristic

C_1^+ Positive characteristic of the free-surface zone

C_1^- Negative characteristic of the free-surface zone

C_2^+ Positive characteristic of the pressurized zone

C_2^- Negative characteristic of the pressurized zone

C_d Discharge coefficient

CFL Courant number

c Gravity wave speed

d Orifice diameter

D Pipe diameter or vertical conduit dimension

D_n A value useful to calculate the flow discharge and pressure with the Method of Characteristics

D_q A value useful to calculate the flow discharge and pressure with the Method of Characteristics

e Thickness of the pipe

E Elasticity modulus of the PVC

f Steady friction factor

f' Additional friction factor

f_{q-l} Quasi-steady friction factor

$\vec{F}$ Flux vector

Fr Froude number

g Gravitational acceleration

H Piezometric head

H^* Absolute air pressure

H_b^* Absolute initial air pocket pressure head

H_0 Piezometric head of the first node of the pressurized zone

H_i^n Pressure of node i of the pressurized zone at time n in the Method of Characteristics

H_{air} Pressure head of the air pocket

H_{air}^n Pressure head of the air pocket at time n

H_{atm} Atmospheric pressure head

H_{res} Water level in the reservoir

h_f Head loss

h_{pe} Positive experimental pressure peak

h_{ve} Negative experimental pressure peak

h_p Positive numerical pressure peak

h_v Negative numerical pressure peak

h_c Distance between the free-surface and the centroid of the flow crosssectional area

h_s Surcharge head

J Hydraulic resistance

J_q Quasi-steady flow pipeline resistance

J_u Pipeline inertance

K Volume modulus

k Polytropic coefficient

K Absolute pipe roughness

K_{loss} Summation of local losses

L Length of the rigid column

L_{pipe} Length of the pipe

L_u Position of the interface in the Shock-fitting approach

m Air content occupied in mixed fluid

N Number of nodes in the pressurized zone

n_M Roughness coefficient

n_u Number of experiments

P Absolute pressure

P_r Reservoir absolute pressure

P_0 Atmospheric absolute pressure

p_{ref} Reference pressure

Q Flow discharge

Q_a Air discharge out of the orifice

Q_i^n Flow discharge of node i of the pressurized zone at time n in the Method of Characteristics

Q^* Dimensionless flow discharge

Q^{*0} Dimensionless flow discharge in the initial conditions

R Gas constant

r Ratio of air mass to water mass

Re Reynolds number

R_c Critical Reynolds number

R_p Hydraulic radius

T Absolute temperature

r_i Least squares

S Sum of squared residuals

$\vec{S}$ Term vector

S_0 Slope of the conduit

S_f Slope of the energy grade

t Time variable

t^* Dimensionless time parameter

Δt Time step

$\Delta t'$ Time step used in the pressurized flow computation

$\Delta t''$ Time step used in the open channel flow computation

t_c Time to close the valve

T_{max} Maximum time of calculation

$\vec{U}$ Vector variable

V_a Air pocket volume

V_a^n Air pocket volume at time n

V_a^* Dimensionless air pocket volume

V_a^{*0} Dimensionless air pocket volume in the initial conditions

V Flow velocity in general or flow velocity of the free-surface zone (in the shock-fitting chapter)

V_u Flow velocity of the pressurized zone

v_1 Flow velocity in the free-surface zone

v_2 Flow velocity in the pressurized zone

v_0 Flow velocity the first node of the pressurized zone, next to the reservoir (in the shock-fitting chapter)

v_n Flow velocity of the last node of the free-surface zone, at the downstream end (in the shock-fitting chapter)

Y Expansion factor

W Interface velocity

x Space variable

Δx Space step

y Free-surface depth

y_n Depth of the last node of the free-surface zone

ρ Mass density

ρ_w Density of water

ρ_a Density of air

ρ_f Fluid density

ρ_{ref} Reference density

λ Darcy-Weisbach friction factor

ν Kinematic viscosity coefficient

τ_w Wall shear stress

ψ Dependant variable

ε Relative error

MOC Method of characteristics

RC Rigid Column

LIST OF APPENDICES

CHAPTER 1 INTRODUCTION

The purpose of Storm Water Systems (SWSs) is to convey storm water under free-surface conditions without surcharging the sewer. The nature of rapid filling in SWSs or maintenance at boundaries can lead to severe problems such as geysers, damage of public and private infrastructures, blowing off of covering manholes, overflows, street inundations, traffic accidents, sever electrical problems, loss of storage capacity … (Vasconcelos and Wright, 2011a and 2011b; Vasconcelos and Chosie, 2013; Hatcher et al., 2015). Indeed, during intense rainfalls or operational maintenance, the free-surface flow alters to a partially pressurized flow and flow behaviors become complex and the prediction of transient flows, including the pressurized and free-surface flows, and the transition zone, will be more complicated. Note that the flow is a transient flow (or unsteady flow) when the pressure and flow rate vary over time in pipelines.

The pressure surges generated by entrapped air pockets during unsteady flows have been studied by Martin (1976) with his pioneer work on air-water interactions during compression-expansion cycles. Later on, this area has also been studied by different authors such as Zhou et al. (2002), De Martino et al. (2008), Vasconcelos and Leite (2012), Hatcher et al. (2015). During intense rain events, stormwaters systems may undergo rapid filling which can trigger the entrapment of air pockets within deep storage tunnel, trunk sewers, and more generally closed conduits. Rapid filling can cause geyser formation associated with the release of trapped air pockets through partially filled vertical shafts (Guo and Song, 1991; Wright et al., 2011). Release of large air pockets through water filled vertical shafts can cause geysering (Vasconcelos et al., 2011b). The article of Vasconcelos and Leite (2012) presents a photo of a geyser occurring in Chicago on June 23rd, 2010, and a photo of the geyser which happened in Montreal on Monday July 18th, 2011, at the location of a manhole located on Wolfe Street, between the streets René-Levesque and Sainte-Catherine. The car parked on the manhole metal cover was violently raised repeatedly. This geyser was due to the escape of the pressurized air that was blocked in the storm sewer, taking large amounts of storm water with it.

This clearly demonstrates that the design of SWS must be improved because it is a matter of public health and public safety. Contaminated water can be released to the ground surface which can lead to flooding of roads, pollution and environmental issues. A better design of SWSs according to sustainable criteria is also expected to reduce the costs and save significant money.

Numerical modelling has now become unavoidable in order to prevent the eventual problems caused by transient flows. There exists commercial software such as SWMM (Storm Water Management Model) which has been used by clients and designers to numerically simulate a closed conduit transient flow. However, such existing numerical models for sewer drainage excessively simplify the problem. The current software and models need to be improved in order to accurately simulate the phenomenon for a better design of SWSs.

The main objective of this project is to study the available numerical models of transient flows in stormwater systems and in particular the ones that cause air pocket entrapment in stormwater systems SWS and to address some improving solutions. The case study is reservoir-pipe system containing an entrapped air pocket. The upstream part of the pipe contains a pressurized flow whereas the downstream part contains a free-surface flow. The downstream end is suddenly closed with a valve and the air pocket is entrapped.

CHAPTER 2 CRITICAL LITERATURE REVIEW

2.1 Literature review

A literature review will be done in this Chapter 2 in order to be able to understand what has been done in the broad research topic that is the modelling of transient flows in stormwater systems. Bousso et al. (2013) have done a critical literature review on the numerical modelling of mixed flows in storm water systems. Mixed flows can be divided into four phases: Free-surface flow, transition open channel-pressurized flow, pressurized flow, and transitional pressurized-free surface flow (Bousso et al., 2014a).

Similar to Bousso et al. (2013), Different numerical models such as the Priessmann slot method, the two-component pressure approach, the shock-fitting approach, the finite-volume method, the rigid column model, the method of characteristics model will also be presented in the literature review of this thesis because these models are important to present to have a global view of what has already been done in the numerical modelling of transient flows in stormwater systems. The literature review can provide ideas of what can be done to achieve the objective of improving the existing numerical models of transient flows causing air pocket entrapment or introducing different approaches.

2.1.1 Priessmann Slot Method:

Transient flows in pipes are governed by the Saint-Venant equations, referred as the continuity equation (2-1) and the momentum equation (2-2):

$$\frac{\partial A}{\partial t} + \frac{\partial Q}{\partial x} = 0, \tag{2-1}$$

$$\frac{\partial Q}{\partial t} + \frac{\partial}{\partial x}\left(\frac{Q^2}{A} + gAh_c\right) + gA(S_f - S_0) = 0, \tag{2-2}$$

where Q is the flow rate, A is the flow area, h_c is the distance between the free-surface and the centroid of the flow cross-sectional area, S_0 is the pipe slope and S_f is the friction slope.

Equations (2-1), and (2-2) can also be written as equations (2-3), and (2-4), respectively:

$$\frac{\partial y}{\partial t} + V\frac{\partial y}{\partial x} + \frac{A}{B}\frac{\partial V}{\partial x} = 0, \tag{2-3}$$

$$g\frac{\partial y}{\partial x} + \frac{\partial V}{\partial t} + V\frac{\partial V}{\partial x} = g(S_0 - S_f), \tag{2-4}$$

where V is the velocity, y is the flow depth, hydrostatic pressure, A is the flow area, B is the top water surface width, S_0 is the channel bottom slope, S_f is the slope of the energy grade line, x is the distance along the channel length, t is the time and g is the gravitational acceleration, equal to $9.81 ms^{-2}$.

As equations (2-3) and (2-4) give indefinite results when the depth of the water reaches the crown, Cunge and Wegner (1964) were the first to suggest a hypothetical slot, called Preissmann slot, on the crown to allow pipe pressurization. Indeed, when the depth of the water reaches the crown, the top water surface width B is close to 0 and $\frac{A}{B}$ tends to infinity. Assuming that the pipe does not have a limit at the top allows to use the same equations (2-3) and (2-4) for the free-surface and the pressurized zones (see Figure 2.1) because this avoids the top water surface width to be close to 0. To allow using the same equations in the surcharged portions of the pipe and to obtain much faster speed of the pressure wave required in the those portions, the width of the Preissmann slot need to be selected accordingly (Vasconcelos et al., 2006c).

$$T_{slot} = \frac{gA}{a^2}, \tag{2-5}$$

where T_{slot} is the width of the Preissmann slot and a is the speed of the pressure wave.

The Preissmann slot method is considered as a shock-capturing model because it employs a single equation in both free-surface and pressurized flows so that the discontinuity at the interface is not solved explicitly and it is captured by solving the governing equations.The shock-capturing approach captures shocks in the solution automatically without tracking explicitly shocks (León et al., 2010) whereas the shock-fitting approach tracks explicitly the shock.

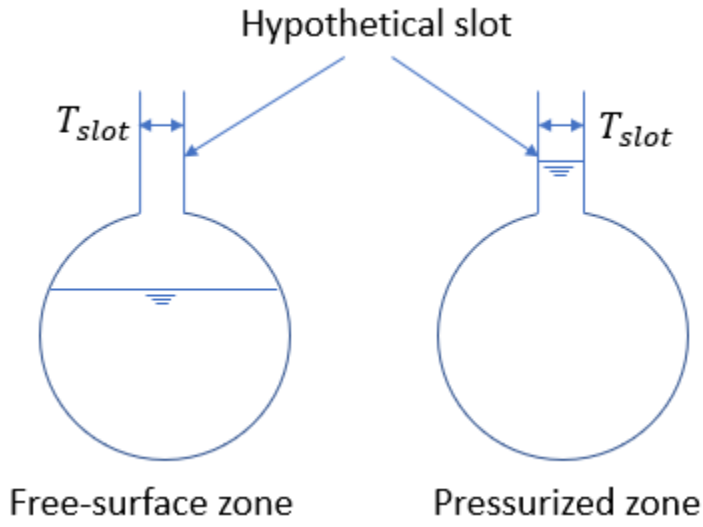

Figure 2.1 The Preissmann slot of combination of a free-surface, and a pressurized flows

It is difficult to choose the right value of the Preissmann slot width T_{slot} because the acoustic wave speed a in actual systems is hard to estimate since it depends on the air content of the water, which is itself unknown (Vasconcelos et al., 2006c). A sufficient narrow slot width will allow to minimize the volume of water stored in the slot's cross section in order to obtain an adequate acoustic wave speed a (Daynou, 2012). For example, a dynamic model based on the Preissmann slot approach is implemented in the software SWMM and uses "the Sjöberg equation (Jackson et al., 1986) to create a smooth transition from the pipe crown to the final slot width of 1% of link diameter" (quote from Pachaly et al., 2020). The width slot cannot be too narrow because spurious numerical oscillations can appear in the solutions (Trajkovic, 1999; Vasconcelos et al., 2006c).

The advantages of the Preissmann slot approach are its simplicity, homogeneity, and ability to simulate gradual transition between the free-surface and pressurized-flows, which may occur far from the wavefront. The disadvantages of this approach are the existence of spurious numerical oscillations when the flow transition coincides with the bore, the instabilities, the inability to simulate pressurized flows with a piezometric head below the pipe crown, and the inaccuracies of the solutions that could be caused by the choice of the slot width (Vasconcelos et al., 2006c; Bousso et al., 2013).

2.1.2 Two-Component Pressure approach (TPA)

As mentioned, the main disadvantage of the Preissmann slot method is that when the piezometric head drops below the crown in the pressurized zone, the free-surface flow is regenerated. In order to handle pressurized flows with sub-atmospheric heads, Vasconcelos (2006c, 2006d) proposed the two-component pressure approach (TPA) as an alternative to the Preissmann slot approach. It considers two components in a modified version of the Saint-Venant equations: the hydrostatic pressure represented by the term h_c (inferior to $D/2$) and the overpressure represented by the term h_s (that can be either positive when the section is full or negative in depressurized flow, for example, in the case of a siphon). The TPA approach gives the following modified version of the Saint-Venant equations (2-6), and (2-7):

$$\frac{\partial A}{\partial t} + \frac{\partial Q}{\partial x} = 0, \tag{2-6}$$

$$\frac{\partial Q}{\partial t} + \frac{\partial}{\partial x}\left(\frac{Q^2}{A} + gA(h_s + h_c)\right) + gA(S_f - S_0) = 0, \tag{2-7}$$

where h_s is the surcharge head.

The TPA assumes the pipe elastic and uses equations (2-8), and (2-9) from Wylie and Streeter (1993) to calculate the acoustic wave speed a and the over-pressurization term h_s:

$$a = \sqrt{\left(\frac{A}{\rho}\right)\left(\frac{\Delta p}{\Delta A}\right)}, \tag{2-8}$$

$$h_s = \left(\frac{a^2}{g}\right)\left(\frac{\Delta A}{A}\right), \tag{2-9}$$

where ΔA is the flow area variation, Δp is the pressure variation and p is the pressure.

More details on the calculations of the TPA can be found in the articles of Vasconcelos (2007, 2009, 2011b). The over-pressurization term h_s is equal to 0 when there is ventilation and is negative when there is no ventilation (Vasconcelos, 2006c). The flow area variation ΔA is positive in the case of a surcharge bore and is negative in low pressure regions. The TPA approach belongs to the category of single-equation models like the Preissmann slot method.

Vasconcelos et al. (2011b) used the rigid column model and the TPA approach to model the rapid filling of closed conduits with entrapped air. They found that the compression-expansion cycles of the air pocket were replicated with reasonable accuracy by both models. As seen in the article of Vasconcelos et al. (2011b), the results of the rigid column approach and the TPA with a steady-state friction factor f are close.

The TPA has the advantages of being simple but is subject to spurious numerical when the acoustic wave speed is high (Sanders and Bradford, 2011). Instabilities can appear when realistic values of the acoustic wave speed are calculated from geometric and elastic characteristics of the pipe (Vasconcelos 2011b; Bousso et al. 2013). Oscillations can occur near open-channel-pressurized flow interfaces (León et al., 2010; Vasconcelos et al., 2006a). The modelling of the air pocket entrapment phenomenon with the TPA approach considering the steady-state friction factor f only has been studied by Vasconcelos et al. (2011). An overestimation of pressure peaks was observed with the use of a steady-state friction factor.

2.1.3 Rigid Column model

Rigid column models belong to the family of two-model equations models and can incorporate air pressurization effects (Bousso et al., 2013). In the original rigid column approach proposed by McCorquodale and Hamam (1983), the air bubble formed during the transient flow is assumed stationary and goes through a compression and expansion process. An approach considering a rigid column was used by Liou and Hunt (1996) to model the filling of pipelines with undulating elevation profiles.

An extension and refinement of the initial rigid column approach was proposed by Li and McCorquodale (1999) in order to simulate the air release transients. It accounts for the transport and the release of the trapped air bubble. Hatcher et al. (2015), Vasconcelos and Leite (2012), Vasconcelos et al. (2011b), and Zhou et al. (2002) are works that used the rigid column model.

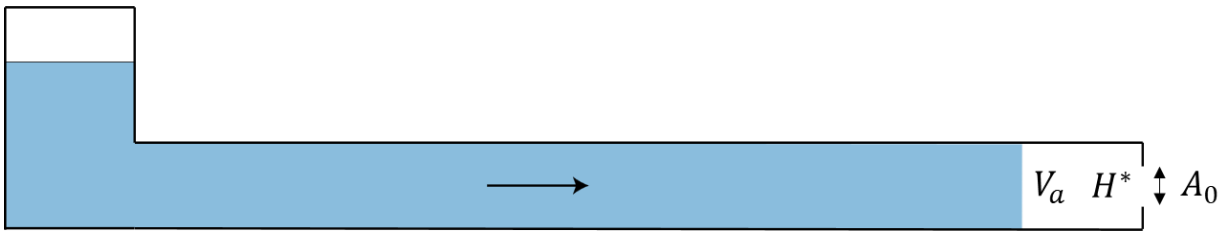

Figure 2.2 A sketch for air release pressure in rigid column model

Equation (2-10) by Martin (1976) is often used by authors like Zhou et al. (2002) as the governing equation for the air phase when there is air release:

$$\frac{dH^*}{dt} = -k\frac{H^*}{V_a}\frac{dV_a}{dt} - k\frac{H^*}{V_a}Q_a, \tag{2-10}$$

where Q_a is the discharge out of the orifice, k is the polytropic coefficient, V_a is the air volume, t is the time and H^* is the absolute air pressure. Q_a is calculated using the following formula,

$$Q_a = C_d A_0 Y \sqrt{2g\frac{\rho_w}{\rho_a} \times \frac{\rho_{a0}}{\rho_a}(H^* - H_b^*)}, \tag{2-11}$$

where H_b^* is the absolute initial air pocket pressure head, A_0 is the cross-sectional area of the orifice, C_d is the discharge coefficient, Y is the expansion factor, ρ_a is the air density, ρ_w is the water density. The expansion factor can be expressed as (Martin 1976),

$$Y = \left[\frac{k}{k-1} \times \left(\frac{H_b^*}{H^*}\right)^{2/k} \times \frac{1 - (H_b^*/H^*)^{(k-1)/k}}{1 - H_b^*/H^*}\right]^{1/2}. \tag{2-12}$$

If $H^*/H_b^* > 1.89$, the orifice is choked (Martin 1976) and the discharge can be calculated as,

$$Q_a = C_d A_0 Y \sqrt{g\frac{\rho_w}{\rho_a}H^*}\sqrt{k\left(\frac{2}{k+1}\right)^{(k+1)/(k-1)}}. \tag{2-13}$$

When the downstream end is closed, there is no air release, thus, Q_a is equal to zero and the last term on the right hand side of equation (2-10) is also zero. The governing equation for the air phase when there is no air release is as,

$$\frac{dH^*}{dt} = -k \times \frac{H^*}{V_a} \times \frac{dV_a}{dt}. \tag{2-14}$$

This will be the case in the problem studied all along this project. The details of the rigid column model will be provided in next chapters.

The modelling of the air pocket entrapment phenomenon with the rigid column model considering the steady-state friction factor (f) only has been studied by Hatcher et al. (2015) and Vasconcelos and Leite (2012). An overestimation of pressure peaks was observed with the use of a steady-state friction factor.

2.1.4 Method of characteristics model

It consists in solving the water hammer problem, which is the Saint-Venant equations, in which instead of gravity wave speed the acoustic wave speed is used. These equations can be used to solved the pressurized flow instead of rigid column model and similarly the entrapped air pocket can be simulated. These equations are solved using a numerical tool called method of characteristics, which is a very common technique used by many authors (Wylie and Streeter 1993; Lohrasbi and Attarnejad 2008; Chaudhry 2014). Thus, in this thesis, the Saint-Venant equations are solved with the method of characteristics called MOC. This approach can take into account air pressurization effects. The method of characteristics will be used and detailed in future chapters. The modelling of the air pocket entrapment phenomenon with the method of characteristics considering the steady-state friction factor f only has been studied by Hatcher et al. (2015). An overestimation of pressure peaks was observed with the use of a steady-state friction factor.

2.1.5 Shock-fitting approach

The shock-fitting approach belongs to the family of two-equation models, in which the interface between pressurized and free-surface flow is tracked explicitly. It is a dynamic model which consists in treating separately the pressurized and the free-surface portions of the flow. According to Bousso et al. (2013), there are usually three ways in which the shock-fitting approach is used:

1. The MOC approach is used to solve the Saint-Venant equations applied to both pressurized and free-surface flows;
2. The rigid column approach is used to model both flow regimes (pressurized and free-surface);
3. The rigid column approach is used to model the pressurized flow and the MOC approach is used to model the free-surface flow.

Wiggert (1972), Politano et al. (2007), Cardle (1984), Rokhzadi and Fuamba (2019, 2020b) are a list of authors who used an interface tracking model. Usually, the shock-fitting approaches consider only one surge front.

2.1.6 Finite-Volume method

The finite-volume model that will be discussed below is the model by León (2007). There is also the model of Bourdarias and Gerbi (2007) that is a finite-volume model but it will not be presented here. The Illinois transient model (ITM), which was initially developed in 2004 using a modified Preissmann slot, has been improved over the years and uses currently a multipurpose finite-volume shock-capturing model developed by León (2007) ranging from dry-bed flows to gravity flows, to partly gravity-partly surcharged flows (mixed flows) to fully pressurized flows (waterhammer flows) (León et al., 2011; 2015). The reason for the change from the modified Preissmann slot model to the finite-volume model in the ITM is the inability of the Preissmann slot model to simulate subatmospheric pressures in pressurized flow conditions contrary to the finite-volume model.

According to León et al. (2007), to simplify the governing equations of two-phase flows (air and water) in closed conduits when the amount of gas in the conduit is small, both phases can be treated as a "single-equivalent fluid" with average properties (Wylie and Streeter 1993) by assuming that there is no relative motion or slip between the gas and the liquid. The "single-equivalent fluid" is governed by the mass and momentum equations which can be expressed in their conservative form as follows (León et al., 2007; 2010):

$$\frac{\partial \vec{U}}{\partial t} + \frac{\partial \vec{F}}{\partial x} = \vec{S}, \tag{2-15}$$

where $\vec{U}$ is the vector of variables, $\vec{F}$ is the flux vector and $\vec{S}$ is the vector of source terms, and x is the spatial variable.

For open-channel flows, $\vec{U}$, $\vec{F}$ and $\vec{S}$ can be written as equations (2-16), (2-17), and (2-18) (León et al., 2007; 2010):

$$\vec{U} = \begin{bmatrix} \rho A_{flow} \\ \rho Q \end{bmatrix}, \tag{2-16}$$

$$\vec{F} = \begin{bmatrix} \rho Q \\ \rho \frac{Q^2}{A} + A_{flow}\bar{p} + \rho g A H_{air} \end{bmatrix}, \tag{2-17}$$

$$\vec{S} = \begin{bmatrix} 0 \\ (S_0 - S_e)\rho g A_{flow} \end{bmatrix}. \tag{2-18}$$

For compressible water hammer flows, $\vec{U}$, $\vec{F}$, and $\vec{S}$ can be written as equations (2-19), (2-20), and (2-21) (León et al., 2007; 2010):

$$U = \begin{bmatrix} \rho_f A \\ \rho_f Q \end{bmatrix}, \tag{2-19}$$

$$F = \begin{bmatrix} \rho_f Q \\ \rho_f \frac{Q^2}{A_f} + Ap \end{bmatrix}, \tag{2-20}$$

$$S = \begin{bmatrix} 0 \\ (S_0 - S_f)\rho_f g A \end{bmatrix}, \tag{2-21}$$

where Q is the flow discharge, A_{flow} is the cross-sectional flow area, A is the full cross-sectional area, $\bar{p}$ is the average pressure of water-column over the cross-sectional area, , H_{air} is the gauge air pressure head,. In compressible water hammer flows, p is the pressure acting on gravity centre of A_f, ρ_f is the fluid density for compressible water hammer flows (León et al. 2010) and p, p_{ref}, a, ρ_f and ρ_{ref} are related with equation (2-22):

$$p = p_{ref} + a^2(\rho - \rho_{ref}), \tag{2-22}$$

where ρ_{ref} and p_{ref} are the reference density and reference pressure, respectively (León et al., 2010).

The finite-volume method of León et al. (2007) can realistically simulate the acoustic wave speed. The air phase pressure equation used in the finite-volume method is either equation (2-10) for air release or equation (2-14) for no air release.

The disadvantage of the finite-volume method is that it can require complex scheme and solvers. The finite-volume method can for example be formulated with Godunov-type scheme (León et al. 2008; Bousso and Fuamba, 2013, Seck et al. 2017).

The modelling of the air pocket entrapment phenomenon with and without air release with the finite-volume method considering only the steady-state friction factor f has been studied by León et al. (2010). An overestimation of pressure peaks can be observed for the case of air pocket entrapment without air release.

2.1.7 2D mathematical models

The previous models presented are one-dimensional. However, it is legitimate to wonder whether 2D models are more accurate than 1D models. This section discusses this point.

Pezzinga (1999) proposed a quasi-2D mathematical model, based on the continuity and momentum equations written for an elastic pipe with circular cross section, for unsteady turbulent flow in pipe and pipe networks. The results of the study show that his quasi-2D model improves the prediction of high-frequency transients in simple pipes and pipe networks with respect to a classical 1D model. By taking into account the velocity profiles, the calculation of the wall shear stress helps improve the evaluation of resistances obtained by the quasi-2D model. However, the simulation duration of the quasi-2D model of Pezzinga (1999) is very long and is about three hours on an IBM RISC System/6000 340, which is about 35 times that needed for 1D models. The computational burden is one the main disadvantages of quasi-2D water hammer models (Jang et al. 2016).

Brunone et al. (1995) also studied a quasi-2D model applied to a water-hammer phenomenon caused by a valve closing and found that two-dimensional models require a higher computational burden than the one, which is necessary in the simulation with a more traditional model. Other difficulties arise with the use of a two-dimensional model such as the definition of boundary conditions in complex pipe networks, in the case of cavitation phenomena.

According to Pezzinga (1999), the more exact evaluation of pressure head oscillation by the quasi-2D model seldom justifies the higher computation time required by the quasi-2D model. This is the reason why, only 1D model will be studied in this Master thesis, namely the models based on the rigid column, the method of characteristics and the shock-fitting approaches.

2.1.8 Quasi-steady and unsteady friction factors

The Darcy-Weisbach steady-state friction factor has usually been used to model the pipe friction during transient events. A literature review of the unsteady friction factor will also be done because the consideration of an additional friction factor in the numerical models is expected to improve the results.

Adamkowski and Lewandowski (2004) compared different friction models to simulate a transient flow in a pipe using the method of characteristics. The frictions models were: frictionless, quasi-steady, Zielke, Trikha, Vardy-Brown, Zarzycki, Brunone et al. (k_3 experimental), and Brunone et al. (k_3 analytical). Among those models, they found that the Zielke and Zarzycki models gave the most reliable results for both laminar and turbulent flows.

The governing equations (continuity and momentum equations) of the unsteady flow in closed conduits are:

$$\frac{\partial H}{\partial t} + \frac{a^2}{g} \times \frac{\partial V}{\partial x} = 0, \tag{2-23}$$

$$\frac{\partial V}{\partial t} + g\frac{\partial H}{\partial x} + g \times J = 0, \tag{2-24}$$

where J, the head loss per length unit of pipe, represents the hydraulic resistance and can be expressed as follows (Adam and Lewandowski, 2004; 2006):

$$J = J_q + J_u, \tag{2-25}$$

where J_q is the quasi-steady flow pipeline resistance (active resistance resulting from viscous friction at the pipe wall) and J_u is the pipeline inertance (reactance accounting for liquid inertia).

In most engineering applications, the slope term in the momentum equation is often small and can be neglected (Chaudhry, 2014).

In the quasi-steady model, the pipeline inertance $J_u = 0$ and the pipeline resistance J_q is equal to:

$$J_q = \frac{f_{q-l}}{gD} \times \frac{V|V|}{2}, \tag{2-26}$$

where D is the diameter and f_{q-l} is the quasi-steady friction factor.

According to Adam and Lewandowski (2004, 2006), the quasi-steady friction factor f_{q-l} (Darcy friction factor) is calculated with the Hagen-Poiseuille law for laminar flows, $Re \leq Re_{c-s}$, in which $Re_{c-s} = 2320$, and the Colebrook-White formula for turbulent flows ($Re > Re_{c-s}$):

$$\begin{cases} f_{q-l} = \dfrac{64}{Re} & Re \leq Re_{c-s} \\ \dfrac{1}{\sqrt{f_{q-l}}} = -2\log\left(\dfrac{2.51}{Re\sqrt{f_{q-l}}} + \dfrac{\frac{K}{D}}{3.71}\right) & Re > Re_{c-s} \end{cases}$$

where K/D represents the pipe-wall roughness. Note that various unsteady frictions factors are presented in Table 2.1.

Table 2.1 Various unsteady friction models

Unsteady friction factors	**Description**
Zielke (1968)	$J_u = \dfrac{16\upsilon}{gD^2}\int_0^t \dfrac{\partial V}{\partial t}(u).W(t-u)du,$ where $W(\tau) = \begin{cases} \sum_{i=1}^{6} B_i \times \tau^{(i-2)/2} & \tau < 0.02 \\ \sum_{i=1}^{6} e^{-A_i \times i} & \tau \geq 0.02 \end{cases}$ $A_i = \{26.3744;\ 70.8493;\ 135.0198;\ 218.9216;\ 322.5544\}$ $B_i = \{0.282095;\ -1.25;\ 1.057855;\ 0.9375;\ 0.396696;\ -0.351563\}$
Trikha (1975)	$J_u = \dfrac{16\upsilon}{gD^2}(y_1 + y_2 + y_3),$ where $y_i(t+\Delta t) = y_i(t) \times e^{-n_i \times \frac{4\upsilon.\Delta t}{D^2}} + m_i[V(t+\Delta t) - V(t)]$ $W_{app}(\tau) = \sum_{i=1}^{3} m_i\, e^{-n_i \tau}$ $m_i = \{40; 8.1; 1\};\quad n_i = \{8000; 200; 26.4\};\quad \tau > 0.00005$

Table 2.2 Various unsteady friction models (cont'd)

Vardy-Brown (2003)	For $Re < 10^5$ $$W(t) \approx W_{app} = (\frac{A^*}{\sqrt{\tau}})\exp(-\frac{\tau}{C^*})$$ $$A^* = \frac{1}{2\sqrt{\pi}}$$ $$C^* = \frac{7.41}{\log_{10}(14.38/Re^{0.05})}$$
Zarzycki (2000)	For laminar flows ($Re \leq Re_{c-u}$): $$W(t) \approx W_{app} = C_1\tau^{-0.5} + C_2.e^{-m\tau}$$ $\tau = \frac{4\upsilon t}{D^2}$; $C_1 = 0.2812$; $C_2 = -1.5821$; $m = 8.8553$ For turbulent flows ($Re > Re_{c-u}$) $$W(t) \approx W_{app} = (\frac{C}{\sqrt{\tau}}.Re^n)$$ $\tau = \frac{4\upsilon t}{D^2}$; $C = 0.299635$; $n = -0.005535$ The critical value of Reynolds number is given by: $$R_{c-u} = 800\sqrt{\frac{\pi D^2 a}{8L\upsilon}}$$

Table 2.3 Various unsteady friction models (cont'd 2)

Brunone et al. (1991)	k_3 found by trial-and-error	$$J_u = \frac{k_3}{g}\left(\frac{\partial V}{\partial t} - a\frac{\partial V}{\partial x}\right),$$ where k_3 is obtained by means of trial-and-error method by matching the computational and experimental results (Brunone et al., 1991; Bergant et al., 1994; Adam and Lewandowski, 2004)
	k_3 found analytically	$$J_u = \frac{k_3}{g}\left(\frac{\partial V}{\partial t} - a\frac{\partial V}{\partial x}\right)$$ An empirical formula was proposed by Vardy and Brown (1996, 2003) to derive k_3 analytically: $$k_3 = \frac{\sqrt{C^*}}{2}$$ where $C^* = 0.00476$ for laminar flow and $C^* = \frac{12.86}{Re^{\log_{10}(15.29/Re^{0.0567})}}$ for turbulent flow.

More details of different unsteady friction models and their comparison can be found in the articles of Adam and Lewandowski (2004, 2006) and Bergant et al. (1994, 2001).

There are many other unsteady friction factors models different than those presented in Table 2.1. Landry et al. (2012) developed a new unsteady model for viscoelastic damping in piping systems without cavitation implemented in the SIMSEN software Nicolet (2007).

For the sake of simplicity (easier to implement and more practical), the additional friction term that will be used in the future chapter will have a form similar to the Darcy-Weisbach factor, i.e. proportional to $LV^2/(2gD)$.

CHAPTER 3 PROCESS FOR THE RESEARCH PROJECT AS A WHOLE AND GENERAL ORGANIZATION OF THE DOCUMENT INDICATING THE COHERENCE OF THE ARTICLES IN RELATION TO THE RESEARCH GOALS

First of all, a literature review was done in Chapter 2 in order to be able to understand what has been done in the broad research topic that is the modelling of transient flows in stormwater systems. Chapter 4, which constitutes the article, will deal with two well-known models: the rigid column model, which will be called RC model, and the method of characteristics model, which will be called MOC model. In both models a steady and an additional friction factors will be used. These models will be compared to relevant experimental data obtained in the Hydraulic laboratory of the University of Polytechnic Montreal. In Chapter 5, these models will be adapted to compare the numerical results with experimental data provided by Hatcher et al. (2015). In Chapter 6, the shock-fitting approach, which includes the water hammer equations equations applied to the pressurized flow, and the Saint-Venant equations, applied to the free-surface flow, is used to solve the air pocket entrapment problem. Finally, in Chapter 7 the implementation of the RC and MOC models using a steady friction factor in the well-known software SWMM (Storm Water Management Model) will be discussed.

It is worth mentioning that all numerical codes, used in this project, which are the RC and MOC models, the shock-fitting approach, and the computational engine, and the GUI (Graphical User Interface) interface of the modified version of SWMM, are gathered in the following public link (google drive):

https://drive.google.com/file/d/1hiRNDYFqVX6_Eyr7mYeEMUr863-bEJF4/view?usp=sharing

CHAPTER 4 ARTICLE 1 : ADDITIONAL FRICTION FACTOR OPTIMIZED TO MODEL TRANSIENT FLOWS FOLLOWING AIR POCKET ENTRAPMENT IN STORMWATER SYSTEMS

ILIAN TOSAN, Master Student, Department of Civil, Geological and Mining Engineering, University of Polytechnique Montréal, C.P. 6079, succ. Centre-ville Montréal, QC, H3C 3A7, Canada, Email: ilian.tosan@polymtl.ca (Corresponding author)

ROLANDO-YEZID PEREZ-PULIDO, Master Student, Department of Civil, Geological and Mining Engineering, University of Polytechnique Montréal, C.P. 6079, succ. Centre-ville Montréal, QC, H3C 3A7, Canada, Email: rolando-yezid.perez-pulido@polymtl.ca

ARMAN ROKHZADI, Ph.D., Postdoctoral Researcher, Department of Civil, Geological and Mining Engineering, University of Polytechnique Montréal, C.P. 6079, succ. Centre-ville Montréal, QC, H3C 3A7, Canada, Email: arman.rokhzadi@polymtl.ca

MUSANDJI FUAMBA, Ph.D., Professor, Department of Civil, Geological and Mining Engineering, University of Polytechnique Montréal, C.P. 6079, succ. Centre-ville Montréal, QC, H3C 3A7, Canada, E-mail: musandji.fuamba@polymtl.ca

ABSTRACT

In partially pressurized transient flows following air pocket entrapment, the frictional force similar to other variables can be affected by the unsteady behavior of the flow and by the air pocket size. Therefore, using a constant steady-state friction factor for the numerical simulation is a simplistic approximation. In this study, an additional friction factor, affected by the size of the air pocket, is introduced. This additional friction, which has the same form as the steady-state Darcy-Weisbach friction factor, has been analyzed and relevant formulas, which were calibrated by experimental data, will be presented. For further discussion, two well-known mathematical models, the rigid column and the method of characteristics models, have been used for the numerical simulation. It was found that, compared to a constant steady-state friction factor, the variable friction factor can significantly improve the numerical results, including the overestimation of the pressure peak values as well as predicting the attenuation behavior.

Besides, it was found that the magnitude of the additional friction factor is inversely affected by the size of the entrapped air pocket. It was shown that using the proposed friction factor calibrated for certain air pocket sizes can also yield good results for other problems with different air pocket sizes.

Keywords: Air pocket entrapment; Numerical models; Laboratory experiments; Pressure surges; Unsteady friction

4.1 INTRODUCTION

Transient flows in Stormwater Systems (SWSs) may occur due to boundary condition disturbances. These disturbances generate wavefronts, which can move upstream or downstream, and cause several problems including geysering, manhole cover displacement, and damage to hydraulic infrastructures. As described by Li and McCorquodale (1999), these disturbances can be caused by rapid filling during intense rainfalls that exceed the network design capacity or by hydraulic equipment failures or by the presence of a drop inlet that suddenly changes flow conditions. The disturbances can cause the free-surface flow to change to a partially pressurized flow, in which the air can be entrapped (Vasconcelos and Wright, 2006a). Vasconcelos and Wright (2006b) experimentally observed five mechanisms for air pocket entrapment in rapidly filling pipelines including an inadequate amount of ventilation, geometrically misplaced ventilation, interface breakdown, shear flow instability, and gradual flow regime transition. They found that the system geometry and the inflow configuration are the key factors for the air pocket entrapment. The problems caused by air entrapment include deterioration of pipelines, joints or valves, oscillations, hydraulic jump, and reduction of the pipe cross-section (Pozos et al., 2010) or more serious operational problems such as severe geysering, loss of storage capacity, and infrastructure damage (Vasconcelos and Chosie, 2013). Geyser events were analyzed in several laboratory studies, exemplified by Vasconcelos and Wright (2005 & 2008). The observations suggest that geysers are formed from the expulsion of large entrapped air through vertical shafts. Wright et al. (2011) indicated that the “only plausible explanation for the geyser formation is the interaction of trapped air with water initially standing in the manhole shaft due to the existence of surcharge conditions”. They also concluded that trapped air within the tunnel system must be included in system design to avoid geyser formation.

The air pocket entrapment phenomenon has been extensively studied and analyzed theoretically and experimentally. Zhou and Hicks (2002) conducted experiments in a rapidly filling horizontal pipe containing trapped air. They indicated that the air entrapped in sewer networks can induce high pressure peaks. De Martino et al. (2008), by varying the driving pressure, the initial size of the air pocket, and the orifice diameter, studied the transient flow caused by the expulsion of a trapped air pocket through an orifice at the downstream end of a pipe. They found that when the upstream head and orifice size increase, the magnitude of peak pressure increases as well. Zhou et al. (2011) conducted experiments in which an air pocket is entrapped at the dead-end downstream of a filling undulating pipeline. They concluded from their tests that the first maximum pressure has an inverse relationship with the initial air volume.

Vasconcelos and Leite (2012) experimentally studied partially pressurized transient flow in a reservoir-pipe system to assess the effects of the air pocket entrapment caused by closing a valve located at the downstream end of the pipe. They observed that when the valve is totally closed, high-pressure peaks are induced followed by damping oscillations. The partially closed valve results in reducing the magnitude of the pressure peaks and shorter pressure oscillation patterns, in fact, only one pressure peak was observed. Hatcher et al. (2015) conducted experiments of air pocket entrapment in a closed conduit transient partially pressurized flow. These tests were carried out in order to analyze the performances of the rigid column and the method of characteristics models. The pressure peak magnitudes were consistently overestimated by both numerical models for total valve closures. Vasconcelos and Leite (2012) acknowledged that the assumption of a constant friction factor limits the abilities of the mathematical models. In addition, by quoting Hatcher et al. (2015):

> "A number of relevant factors may play a role in defining the actual energy damping of these flows including frequency dependent friction (Wylie and Streeter, 1993), viscoelastic effects in plastic pipes (Soares et al., 2008) and thermofluid dynamics effects (Lee, 2005)."

Hence, one objective of this article is to propose an additional friction factor that accounts for energy damping so that the performance of the mathematical models, used for simulating partially pressurized transient flows following air pocket entrapment, is improved.

Many authors have developed expressions to describe damping energy caused by head losses in transient flows (Ghidaoui et al., 2005). The expressions are based on the idea that the wall shear

stress in pipes plays an important role in the loss of energy when the water hammer occurs. In these equations, the instantaneous wall shear stress is decomposed by the contribution of the wall shear stress in steady-state flow and the wall shear stress in unsteady-state flow. Some unsteady friction models were developed from both theoretical and laboratory experiments.. Wan et al. (2010) presents a compound mathematical model to simulate the attenuation of hydraulic transients in valve closing process, which considers the laminar and the turbulent friction resistance. It is worth mentioning that Wan et al did not take into account the effects of entrapped air pocket. The simulation of hydraulic transients of the valve closing process was expressed by the method of characteristics. The maximum and minimum transient pressures and the general attenuation behavior were accurately simulated by the compound mathematical model. Zhang et al. (2018) introduced a supplementary friction function to evaluate the effect of the air entrainment on transient pressure attenuation caused by the water hammer wave. In this methodology the additional friction function depends on a coefficient (C), which is necessary to calibrate experimentally. In addition to the steady-state friction factor, the supplementary friction function improves the approximation of the pressure attenuation of the water hammer wave. However, the study from Zhang et al. (2018) was done in the case of water hammer with continuous air entrainment. The air content was not measured directly but estimated from the measured value of the acoustic wave speed (a). From Wylie and Streeter (1993), the air entrainment is determined assuming that the gas bubbles (air) are distributed uniformly throughout the liquid (water). In the present article, the effects of air pocket with different sizes are studied to further analyze the effects of an air pocket, which is separated from the liquid. Bousso and Fuamba (2013), using the Godunov finite volume method, numerically simulated transient flows caused by valve closing. They applied an unsteady friction factor, which is decomposed into static friction and unsteady friction components. The unsteady friction component was determined by considering local and convective instantaneous accelerations, which is similar to the model proposed by Brunone et al. (1995, 2000). However, Bousso and Fuamba did not study the air pocket entrapment problem, while they integrated the presence of a low volume of air distributed in the water. In addition, the variable friction factor of Bousso and Fuamba (2013) is more difficult to calculate than the one presented in this article which has a similar form to the Darcy-Weisbach friction factor. The role of the supplementary unsteady

friction factor is to evaluate more accurately the loss in energy, compared to the steady-state friction factor alone. An unsteady friction factor is a friction factor that varies over time.

The present paper discusses the effect of frictional force in simulating transient partially pressurized flows caused by air pocket entrapment within SWSs. In the literature, it is common to calculate the frictional force with a pressurized flow using a steady-state Darcy-Weisbach friction factor. However, as will be shown, a variable friction factor can significantly improve the behavior of the numerical solutions. In this regard, an additional friction factor, which depends on the flow parameter, will be introduced. By using experimental data, this friction factor is calibrated for two different initial air volumes. In addition, two well-known mathematical models, the rigid column model, and the method of characteristics model that solves the Saint-Venant governing equations, are employed to numerically simulate some test cases for which the experimental data are available. It will be shown that the proposed variable friction factor can help to improve the numerical solutions, compared to the steady-state friction factor.

4.2 Material and methods

The rigid column and the method of characteristics models are used to solve a closed conduit transient partially pressurized flow following an air pocket entrapment. For the undertaken examples, experimental tests were carried out to produce the flow variables in the presence of different initial air pocket volumes. The numerical models were also tested on experimental data from the literature. The Buckingham π theorem of dimensional analysis is employed to derive a formula for the additional friction factor, in which the effects of different variables, including the ratio of the air to water masses and the acoustic wave speed, are taken into account. Following Zhang et al. (2018), by using the numerical results and the experimental data, an optimization algorithm is implemented to calibrate the additional friction factor for two different (small and large) initial air pocket volumes to show how the air pocket volume can affect the friction factor. The optimized additional friction factor corresponds to the value which minimizes the sum of differences between the experimental and numerical pressure peaks. Afterward, the proposed additional friction factor is used to solve other examples to discuss the effects of additional friction factor on the closed conduit transient flows as well as to show how this additional friction factor can help mathematical models to more accurately calculate numerical solutions.

4.2.1 Description of the Polytechnique Montréal experiments

The experimental tests were carried out in the hydraulics laboratory of Polytechnique Montréal. As shown in Figure 4.1, the assembly consists of a supply tank (R1), with the dimensions of 1.01 m (length) × 1.01 m (width) × 1.04 m (height), an intermediate cylindrical tank (R3), with the dimeter of 0.355 m and height of 1.775 m, and a transparent PVC horizontal pipe (C_1), which connects R_1 and R_3. The pipe sizes are schedule 40, diameter D = 100 mm, and length L_{pipe} = 5.06 m. After the flow passes the cylindrical tank, the water is transferred to another tank where it is pumped back to the supply tank. A valve (VA_1) at the inlet of the supply tank was installed to control the water inflow. Also, at the downstream end of the pipe C_1, a valve (V_2) is installed by which the pipe's end can be completely blocked.

For measuring flow variables, six pressure sensors Omega are installed on the pipe C_1, four of which are Omega type PX409-2.5G5V accuracy ±0.08% (C1P2, C1P3, C1P4, and C1P5), one is Hoskin type P9-1H1-DN1C0-3PSI-15V accuracy ±0.5% (C1P1), and the last one is type AB (P) 15V (C1P6). In addition, two pressure sensors, Omega type PX-603-015G5V accuracy ±0.4 %, are installed on R_1 and R_3, called R1P1, and R3P1, respectively. An Arkon electromagnetic flowmeter (DME) type MAG910E with accuracy of 1.0% is installed to measure the water flow inlet to the tank R_1 and a Hedland ultrasonic flowmeter (DMU) type HTTF with accuracy of 1.0% is located on the pipe C_1 at $0.783L_{pipe}$.

The experiments were recorded by a SVSi StreamView LR High-Speed camera, 60 frames per second (FPS), 1280×1024 resolution and a conventional video camera Canon VIXIA HFS200 HD. The pressure data from pressure sensors were collected in two data-acquisition cards by means of National Instruments' LabVIEW data acquisition software. The time to close the valve (t_c) was in the range of $0.2-0.5$ s, which was obtained by recording the valve closure by means of a camera of 30 FPS.

The inlet to the tank R_1, controlled by the valve VA_1, was opened to the point of obtaining steady flow in the conduit C_1, which contained a pressurized flow at upstream and a free-surface at downstream, and a stable cavity formed on top of the free-surface flow (Figure 4.2). The photos of the flow were used in AutoCAD software to draw the water profiles and to obtain the initial water and air volumes (Figure 4.2). The LabVIEW software was initialized to read the pressure in the initial conditions and to read the variation of the measured pressure with sensors placed in the

pipe and reservoirs, as described before. Then, the valve V_2 downstream of pipe C_1 was closed completely and the air pocket was entrapped. The valve VA_1 was also closed to prevent increasing the water level in the supply tank. Thus, the water level in the reservoir R_1 remained constant during the experiment. Consequently, the surge pressure was generated by which the air pocket was compressed and expanded. Note that the tests were carried out repeatedly for different flow rates in the pipe and for three different water levels in reservoir R_1 and the most consistent test results were kept for further analyses.

(a)

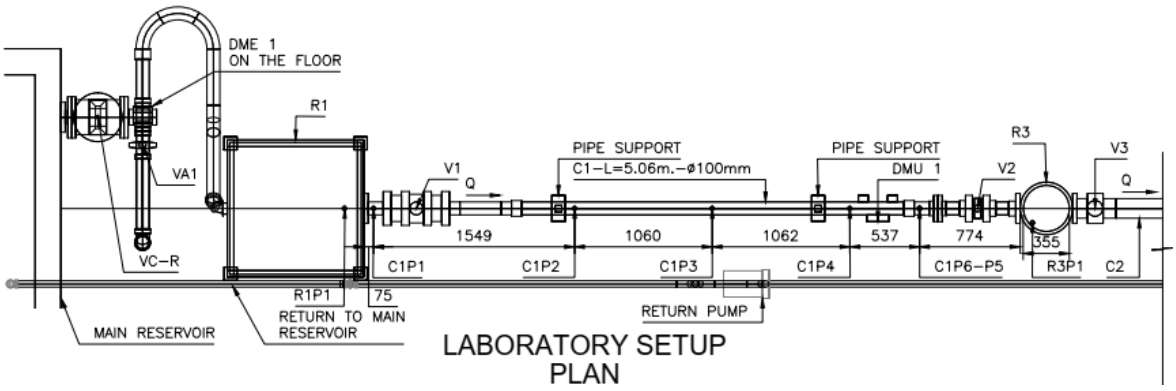

(b)

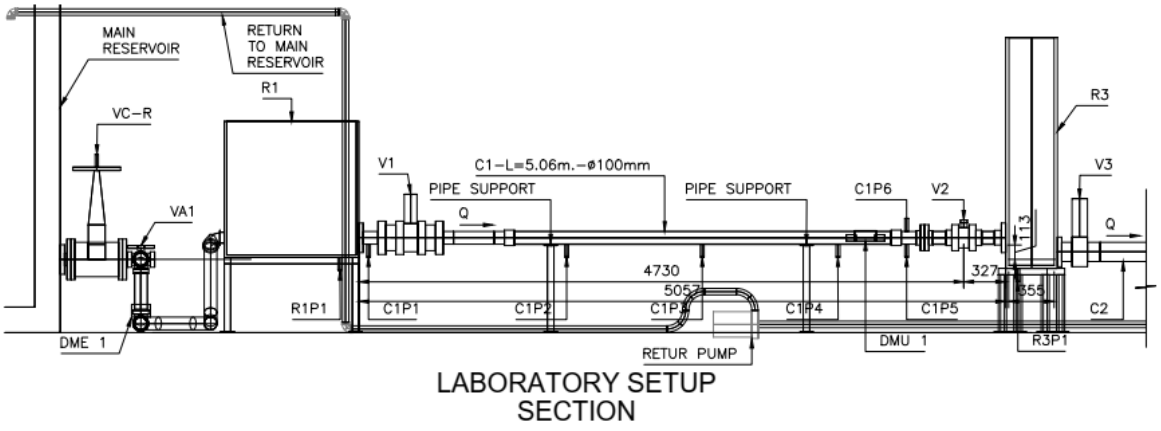

Figure 4.1 The laboratory setup; a) Plan view, and b) Section view

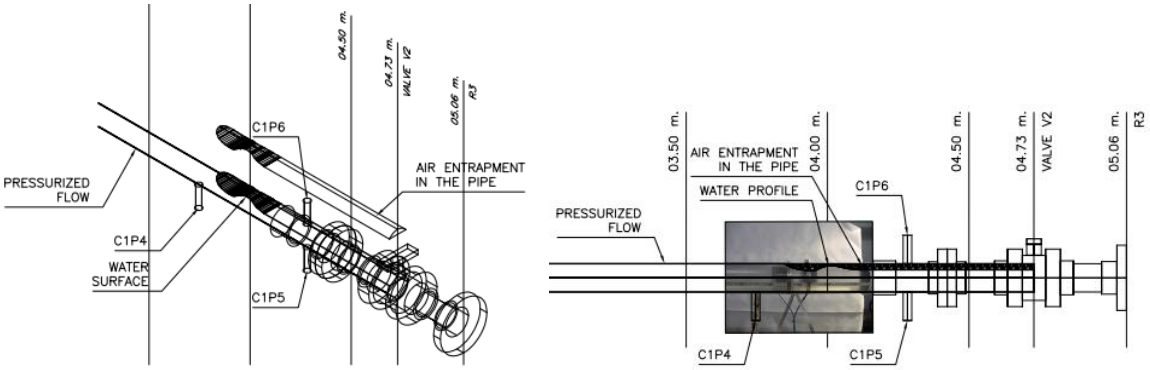

(a) (b)

Figure 4.2 The profile obtained from the design software in initial conditions. (a) Isometric and (b) Section pipe view

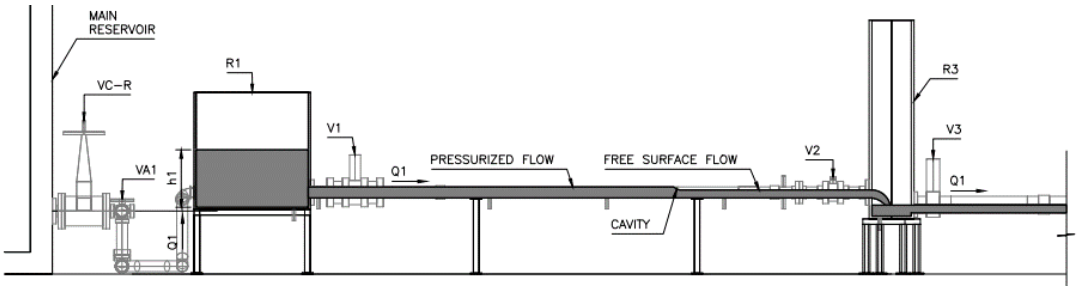

Figure 4.3 The initial steady flow conditions

To calculate the constant Darcy-Weisbach friction factor, the steady-state partially pressurized flow with different flow rates were experimentally developed and the pressure head loss within the pipe, between the C1P1 and C1P5 sensors, which are located upstream and downstream, respectively, were measured (see Figure 4.1). The Darcy-Weisbach formula using the steady-state friction factor (f), is:

$$h_{fi} = f\frac{L_{pipe}}{D}\frac{V_i^2}{2g} \tag{4-1}$$

where the subscript (i) represents the number of experiments, D is the pipe diameter, h_{fi} is the head loss, L_{pipe} is the length of the pipe, V_i is the flow velocity, g is the gravitational acceleration, which is set to 9.81 $m.s^{-2}$. By using the experimental setup dimensions, equation (4-1) can be simplified as:

$$h_{fi} = K_f V_i^2, \tag{4-2}$$

where $K_f = 2.1448 \times f$.

The least square method is used to minimize the summation of the squared differences between the pressure heads measured by experiments and the pressure heads calculated by equation (4-2), in which the experimental velocities are used. Therefore,

$$r_i^2(K_f) = \left[h_{fi} - K_f V_i^2\right]^2, \tag{4-3}$$

$$S_r(K_f) = \sum_{i=1}^{n_u} r_i^2(K_f), \tag{4-4}$$

where n_u is the number of experiments, r_i is the residual and S_r is the summation of residuals. Substituting the experimental data yields:

$$S_r(K_f) = 0.055 - 0.1906K_f + 1.6515{K_f}^2. \tag{4-5}$$

Note that the minimum value of S_r can be found through setting the first derivative of equation (4-5), in terms of K_f, to zero. Thus, K_f is around 0.0579 (see Figure 6.4), and substituting K_f in equation (4-2) results in $f = 0.0269$.

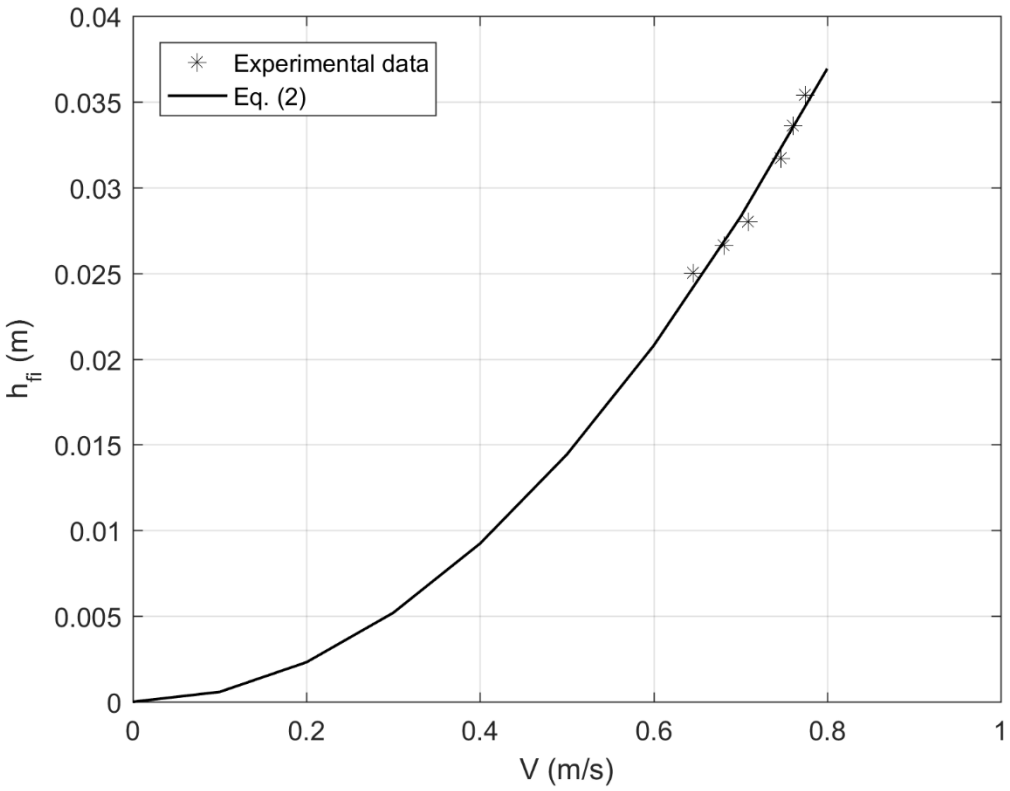

Figure 4.4 The determination of the steady-state friction factor (f)

4.2.2 Other experiments from Zhou (2020) and Hatcher et al. (2015)

Some experiments from Zhou (2000) and Hatcher et al. (2015) are similar to those done in the laboratory of Polytechnic Montréal. To not overload the paper with too many examples, only a few experimental data from these references will be taken for comparison. The characteristics of these experiments will be given in the results and discussions section.

4.2.3 Numerical model and calculation

4.2.3.1 Rigid column model

The concept of the rigid column model is based on neglecting the water compressibility so that the velocity and pressure are space-invariant variables throughout the pressurized flow, which is assumed as a rigid water column.

Following other references, exemplified by Hatcher et al. (2015), Vasconcelos and Leite (2012), Vasconcelos et al. (2011b), and Zhou et al. (2002), by using the rigid column model, the air-

water interface is assumed to be vertical so that the free-surface flow zone is neglected. Thus, the governing equations include the momentum equation of the water column, equation (4-5), and the continuity equation, equation (4-6), and the time derivative of the polytropic process relationship of the ideal gas law, equation (4-7), applied to the air pocket.

$$\frac{dQ}{dt} = \frac{gA}{L}\left[H_{res} - (H_{air} - H_{atm}) - \left(\left(f\frac{L}{D} + K_{loss}\right)\frac{Q|Q|}{2gA^2}\right)\right], \tag{4-6}$$

$$\frac{dV_a}{dt} = -Q, \tag{4-7}$$

$$\frac{dH_{air}}{dt} = -k\frac{H_{air}}{V_a} \times \frac{dV_a}{dt}, \tag{4-8}$$

where t is the time variable, Q is the discharge, V_a is the air pocket volume, H_{air} is the air phase absolute pressure head, H_{atm} is the atmospheric absolute pressure head, which is set to 10.33 m, L is the equivalent water column length, which is explained later. In addition, D is the pipe diameter, A is the cross-sectional area of the pipe, f is the Darcy-Weisbach steady-state friction factor, K_{loss} is the summation of local losses, and k is the polytropic coefficient. Following Lee (2005), the polytropic coefficient k is set equal to $k = \gamma = 1.4$, in which γ represents the adiabatic constant of the air.

Note that the equivalent water column length is calculated as:

$$L = \frac{L_{pipe}A - V_a}{A}, \tag{4-9}$$

to compensate for the water volume of the free-surface flow, which is neglected in applying the rigid column model.

The set of equations (4-6), (4-7), and (4-8) of the rigid column model is solved by using the classical 4th order Runge-Kutta method as described in other references (e.g. Rokhzadi and Fuamba 2020a; Press et al. 2007).

4.2.3.2 Method of characteristics model

The governing equations for one-dimensional flow in closed conduits constitute a pair of partial differential equations (PDEs), which are the continuity and momentum equations, respectively, (Wylie and Streeter, 1993; Chaudhry. 2014):

$$\begin{cases} \dfrac{\partial V}{\partial t} + g\dfrac{\partial H}{\partial x} + \dfrac{f|V|V}{2D} = 0 \\ \dfrac{\partial H}{\partial t} + \dfrac{a^2}{g}\dfrac{\partial V}{\partial x} = 0 \end{cases}, \tag{4-10}$$

where V is the water velocity, H is the piezometric head, a is the acoustic wave speed, and x is the spatial variable along the pipe axis with the positive direction from the upstream to the downstream.

The method of characteristics is a numerical method with first order of accuracy, which has been commonly used to solve the water hammer equations. The method of characteristics allows to transform the pair of PDEs, equation (4-10), into two ODEs along two positive and negative characteristics as presented below. Note that further details of this method can be found in other references (e.g. Wylie and Streeter 1993).

Boundary conditions:

For the first node of the pressurized flow zone at the upstream (the one near the reservoir), only the negative characteristic C^-, which originates somewhere between the first and second nodes, can be used for the calculation. Thus, for the first node, the energy equation between the reservoir and the first node of the pressurized zone is used instead of the equation along the positive characteristic:

$$H_1^{n+1} = (H_{res} + H_{atm}) - (1 + K_{loss}) \times \frac{Q_1^n|Q_1^n|}{2gA^2}, \tag{4-11}$$

where the subscript (1) denotes the first node of the pressurized flow zone.

The unsteady term in the Bernoulli equation is neglected since the reservoir area is much larger than the pipe area (MIT OpenCourseWare 2013).

For the last node of the pressurized flow zone (the one near the air pocket), only the equation along the positive characteristic C^+ can be used. Therefore, instead of the negative characteristic line, the energy equation between the last node of the pressurized zone and the air pocket is used:

$$H_N^{n+1} = H_{air}^{n+1} - \frac{Q_N^{n+1}|Q_N^{n+1}|}{2gA^2}, \tag{4-12}$$

where N represents the last node of the pressurized flow zone.

The air pocket pressure was also calculated using the polytropic process relationship of the ideal gas law.

4.2.3.3 Friction factor analysis

In this paper, an extra friction factor will be proposed to properly calculate the energy dissipation, which cannot be predicted only by the steady friction factor. Thus, the friction term in the governing equations forms as:

$$h_f = (f + f')\frac{L}{D}\frac{V^2}{2g}. \tag{4-13}$$

Following Lee (2005), the flow velocity (V) is assumed to be a function of all effective parameters of a transient flow in a reservoir-pipe system with one end side blocked and followed by the air entrapment:

$$V = V(P_{res}, P_0, L_a, L, a_{air}, a, \rho_a, \rho, \tau_w, D) \tag{4-14}$$

where P_{res} is the reservoir absolute pressure, P_0 is the atmospheric absolute pressure, L_a is the air pocket length, L the water column length, a_{air} and a are the acoustic wave speeds in air and water phases, respectively. ρ_a is the air density, ρ is the water density, τ_w is the wall shear stress. The Buckingham π theorem of dimensional analysis can result in:

$$\frac{\tau_w}{P_{res}} = F\left(\frac{L_w}{L_a}, \frac{\rho V^2}{P_{res}}, \frac{\rho_a V^2}{P_{res}}, \frac{D}{L_a}, \frac{a}{V}, \frac{a_{air}}{V}\right) \tag{4-15}$$

It is known that the friction factor (f) is defined as:

$$f \propto \frac{\tau_w}{\frac{1}{2}\rho V^2} \tag{4-16}$$

Thus, in this study, based on the dimensional analysis, it is assumed that the additional friction factor (f') is a function of the main parameters including $\frac{P_{res}}{P_0}$, $\frac{\rho_a}{\rho}$, $\frac{L_a}{L}$, $\frac{a}{\sqrt{gD}}$, and $\frac{1}{V}$ as:

$$f' = f'\left(\frac{P_{res}}{P_0}, \frac{\rho_a}{\rho}, \frac{L_a}{L}, \frac{a}{\sqrt{gD}}, \frac{1}{V}\right), \tag{4-17}$$

In order to include the type of flow regime (laminar or turbulent flow), the term $\frac{1}{V}$ is replaced with λ, which is the steady-state friction factor and will be defined later. The formula for the additional friction factor (f') becomes:

$$f' = f'\left(\frac{P_{res}}{P_0}, \frac{\rho_a}{\rho}, \frac{L_a}{L}, \frac{a}{\sqrt{gD}}, \lambda\right), \tag{4-18}$$

This leads to the following formula for the additional friction factor:

$$f' = C' \times \frac{H_{res} + H_{atm}}{H_{atm}} \times \frac{\rho_a}{\rho} \times \frac{L_a}{L} \times \frac{a}{\sqrt{gD}} \times \lambda, \tag{4-19}$$

where C' is the calibration factor. Following Wan et al. (2010) and Zhang et al. (2018), λ can be described as $\lambda = \frac{64\nu}{VD}$ for laminar flow regimes, in which ν represents the kinematic viscosity. In addition, for turbulent flow regimes $\lambda = \frac{8gn_M^2}{\sqrt[3]{R_p}}$, in which n_M is the roughness coefficient and R_p is the hydraulic radius. Therefore, a compound model can be used depending on the critical Reynolds number (Re_c) as:

$$\lambda = \begin{cases} \frac{64\nu}{VD} & Re \leq Re_c \text{ (Laminar)} \\ \frac{8g(n_M)^2}{\sqrt[3]{R_p}} & Re > Re_c \text{ (Turbulent)} \end{cases}, \tag{4-20}$$

where $\mathrm{Re_c}$ is set to 2320 (Eckhardt, 2009) and $\mathrm{R_p}$ for circular pipe can be calculated as $D/4$. As can be seen in equation (4-20), the steady-state friction factor for turbulent flow is a function of the roughness parameter only.

Note that during the simulation when $\mathrm{V} = 0$, since the coefficient λ is not defined, the additional friction factor f' is set to zero.

In order to facilitate the optimization procedure, C' is replaced with $C \times 10^3$ and the coefficient of C is moved to the denominator of the ratio $\frac{\rho_a}{\rho}$. Thus:

$$f' = C \times \frac{H_{res}+H_{atm}}{H_{atm}} \times \frac{\rho_a}{10^{-3}\rho} \times \frac{L_a}{L} \times \frac{a}{\sqrt{gD}} \times \lambda. \tag{4-21}$$

The presence of the term $\frac{H_{res}+H_{atm}}{H_{atm}}$ in the formula of f' is coherent with the result found by Rokhzadi and Fuamba (2021) that the damping is a function of the reservoir pressure ratio ($\frac{P_{res}}{P_0} = \frac{H_{res}+H_{atm}}{H_{atm}}$).

Following Hatcher and Vasconcelos (2017) and Wylie and Streeter (1993), the acoustic wave speed in a conduit containing water and air is calculated as:

$$a = \sqrt{\frac{K/\rho}{1+KD/Ee+mRT(K/P_0-1)/P_0}}, \tag{4-22}$$

where R is the gas constant equal to $8.314\, J.K^{-1}.mol^{-1}$, T is the absolute temperature set to $293\,°K$, m is the air content, K is the volume modulus equal to $2.15\, GPa$, P_0 is the atmospheric absolute pressure, calculated as $\rho g H_{atm}$, e is the thickness of the PVC pipe equal to $7\, mm$, E is the elasticity modulus of the PVC pipe equal to $2.5\, GPa$ and ρ is the liquid density equal to $998\, kg/m^3$.

Equation (4-22) of the acoustic wave speed is normally used when air is assumed to be distributed as small discrete bubbles (Wylie and Streeter, 1993). Since, the precise value of the acoustic wave speed is not necessary in the models used in this article, the assumption is made that this equation can be used to approximate the acoustic wave speed in the case of air pockets. The authors acknowledge that calculating the acoustic wave speed in the pipe with the entrapped air pocket using Equation (4-22) leads to some slight errors, but only an approximation of the

acoustic wave speed is needed because the friction factor in Equation (4-22) is not sensitive to the acoustic wave speed.

Note that to take into account the effect of the additional friction factor, in the governing equations provided in the previous subsections, f is replaced with $f + f'$. The optimum C value, proposed for different ranges of air pocket size (small and large), is calculated as explained in the following paragraph.

The governing equations are solved for different C values and the pressure distributions calculated by both the rigid column and the method of characteristics models are compared to the relevant experimental data and the sum of squared residuals (S), provided in Equation (4-23), is calculated.

$$S = \sum_{i=1}^{np} \left(\left[h_{pe}(i) - h_p(i) \right]^2 + \left[h_{ve}(i) - h_v(i) \right]^2 \right), \tag{4-23}$$

where np is the number of peak values, h_{pe} , and h_{ve} correspond to the experimental positive and negative peaks, respectively, and h_p, and h_v correspond to the numerical positive and negative peaks, respectively. Finally, the value of the calibration factor (C) that corresponds to the minimum S value is considered to yield the optimized additional friction factor (f'). Note that the results of this optimization will be presented in the next section. It is worth mentioning that the additional friction factor (f') is calculated in a similar way for both rigid column and the method of characteristics models.

4.3 Results and discussions

4.3.1 Polytechnique Montréal experimental data

The summation of local losses K_{loss} is assumed equal to 0. Note that the discharge and air volume are introduced in non-dimensional forms as $Q^* = Q/\sqrt{gD^5}$ and $V_a^* = V_a/D^3$. As mentioned in the previous section, the calibration factor was optimized for two different test cases representing problems with small and large air pocket volumes. After examining different test cases for which experimental data were available, for the first case, which is considered as a representative for problems with small air pocket size, the water level in the upstream reservoir is

$H_{res} = 0.30\,m$, the pipe diameter $D = 0.1\,m$, and the initial values of air pocket volume (V_a^{*0}), and discharge (Q^{*0}) are 1.11 and 0.422, respectively. For this test case, the air pocket length is $L_a = 0.14\,m$, the water column length is $L = 4.92\,m$ and the acoustic wave speed is $a = 408\,m/s$. In addition, the time for valve closure was measured as $t_c = 0.50\,s$. As shown in Figure 4.5, the optimized calibration factor is calculated as $C = 13$ and it was obtained by the compound model, which was presented in Equation (4-24). Therefore, the additional friction factor for small air pocket sizes can be calculated as:

$$f' = \begin{cases} 13 \times \dfrac{H_{res} + H_{atm}}{H_{atm}} \times \dfrac{\rho_a}{10^{-3}\rho} \times \dfrac{L_a}{L} \times \dfrac{a}{\sqrt{gD}} \left(\dfrac{64\nu}{VD}\right) & Re \le Re_c \ \ (Laminar) \\ 13 \times \dfrac{H_{res} + H_{atm}}{H_{atm}} \times \dfrac{\rho_a}{10^{-3}\rho} \times \dfrac{L_a}{L} \times \dfrac{a}{\sqrt{gD}} \left(\dfrac{8gn^2}{\sqrt[3]{R_p}}\right) & Re > Re_c\ (Turbulent) \end{cases} \tag{4-24}$$

Similarly, for another example, which, based on the available experimental data, was found as an appropriate representative for the problem with large air pocket sizes, the water level in the reservoir is $H_{res} = 0.11\,m$, the pipe diameter is $D = 0.1\,m$ and V_a^{*0}, and Q^{*0} are 1.83 and 0.406, respectively. The air pocket length is $L_a = 0.233\,m$, the water column length $L = 4.83\,m$ and the acoustic wave speed $a = 401\,m/s$. For this example, the time of valve closure is $t_c = 0.33\,s$. As can be seen in

(a) (b)

Figure 4.6, the optimized calibration factor is calculated as $C = 4$. Therefore, for large air pocket sizes, the additional friction factor can be calculated as:

$$f' = \begin{cases} 4 \times \dfrac{H_{res} + H_{atm}}{H_{atm}} \times \dfrac{\rho_a}{10^{-3}\rho} \times \dfrac{L_a}{L} \left(\dfrac{64\nu}{VD}\right) & Re \le Re_c \ \ (Laminar) \\ 4 \times \dfrac{H_{res} + H_{atm}}{H_{atm}} \times \dfrac{\rho_a}{10^{-3}\rho} \times \dfrac{L_a}{L} \left(\dfrac{8gn^2}{\sqrt[3]{R_p}}\right) & Re > Re_c\ (Turbulent) \end{cases} \tag{4-25}$$

Equations (4-24) and (4-25) will be used to further discuss the effects of additional friction factor on the transient flow following the air pocket entrapment. Note that comparing the coefficient C in Equations (4-24) and (4-25), for the problems described above, reveals that the additional friction factor for problems with smaller air pocket sizes is larger.

It is worth mentioning that the acoustic wave speed (a), calculated by Equation (4-22), is in the range of 400, while it does not have much influence on the results of both numerical models (rigid column and method of characteristics models) with or without the additional friction factor.

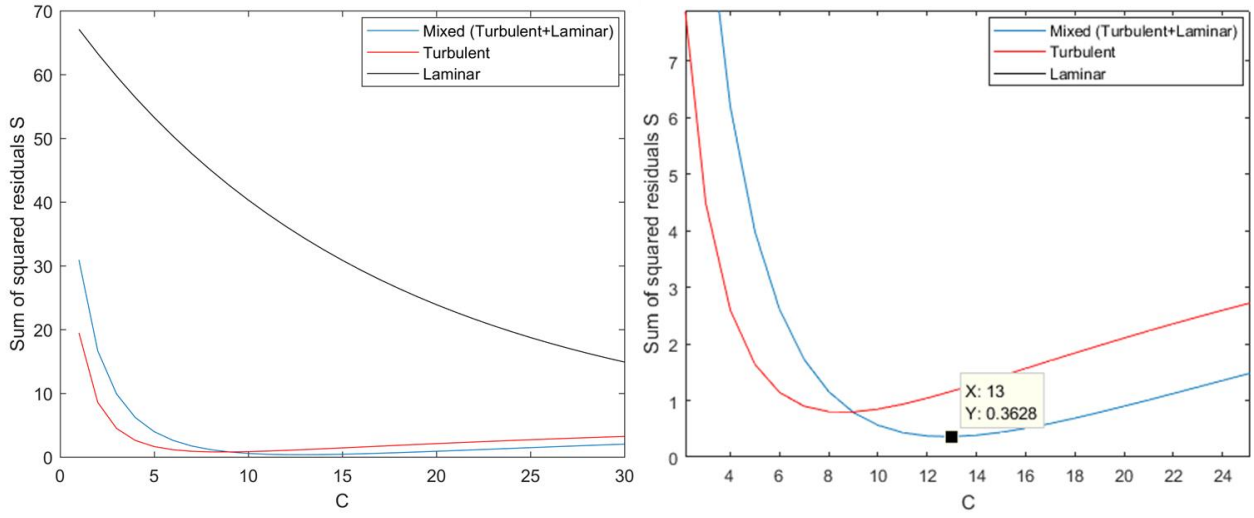

(a) (b)

Figure 4.5 a) The determination of the calibration factor (C), and b) zoom in view with Polytechnic Montreal experimental data ($V_a^{*0} = 1.11$, $Q^{*0} = 0.422$, $t_c = 0.50\ s$, $k = 1.4$ and $H_{res} = 0.30$)

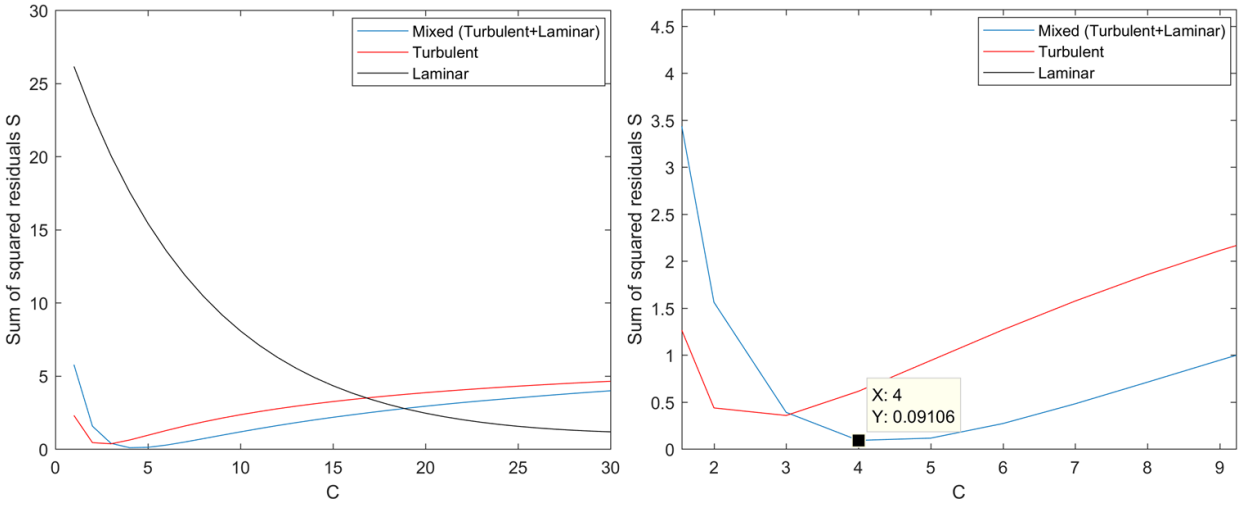

(a) (b)

Figure 4.6 The determination of the calibration factor (C), and b) zoom in view with Polytechnic Montreal experimental data ($V_a^{*0} = 1.83$, $Q^{*0} = 0.406$, $t_c = 0.33\ s$, $k = 1.4$ and $H_{res} = 0.11$)

In this paper, the effects of additional friction factor on the numerical solutions of a transient partially pressurized flow following air pocket entrapment have been studied by using the rigid column and the method of characteristics models. Hereafter, the results calculated by the rigid column model is called RC, and the results of the method of characteristics model, is called MOC. Figure 4.7 shows the pressure distribution for a test case, which was calculated by both

models using the constant steady-state (f), and the friction factors ($f + f'$). In this test case, for which the calibration factor is optimized, the variables (V_a^{*0}, Q^{*0}) are (1.11,0.422), and the water level in the upstream reservoir is $H_{res} = 0.30\,m$. Note that the air pocket behavior is simulated using the polytropic process of an ideal gas in which the polytropic coefficient is $k = 1.4$.

As can be seen in Figure 4.7, compared to the steady-state constant friction factor, the additional friction factor can significantly improve the quality of the numerical solutions calculated by both models. This improvement includes predicting the attenuation behavior of the pressure variation as well as calculating the peak values. Therefore, it can be claimed that the additional friction factor help simulate the energy dissipation more properly. It is worth mentioning that for this test case, which is a representative of examples with small air pocket sizes, the phase shift between the experimental data and the numerical results is almost insignificant.

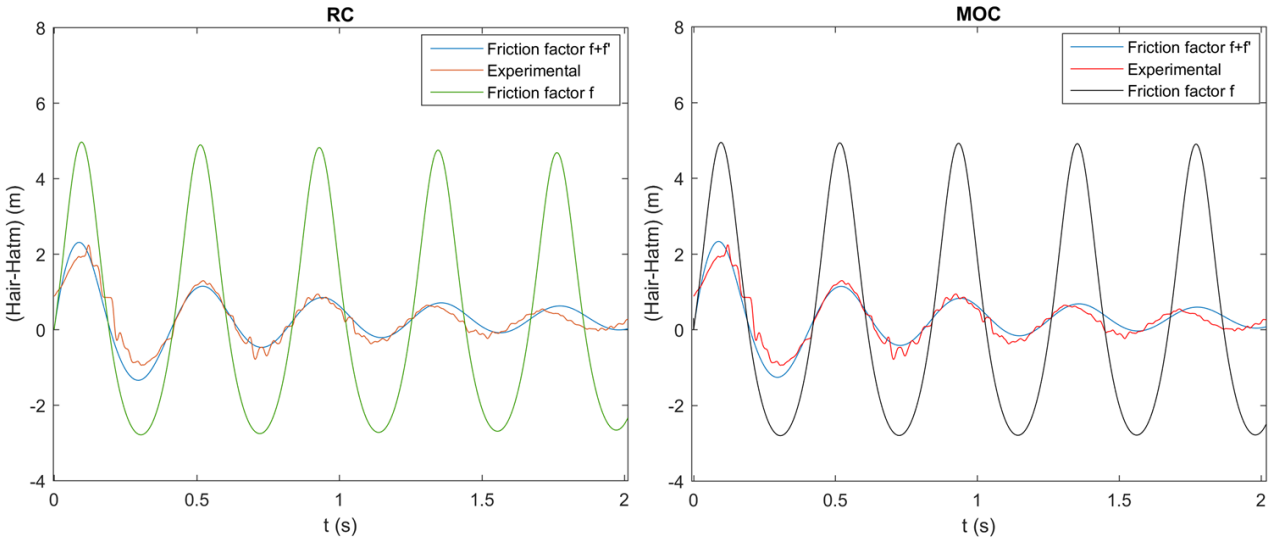

Figure 4.7 The pressure distribution of the air pocket against time for (a) RC, and (b) MOC with Polytechnic Montreal experimental data ($V_a^{*0} = 1.11$, $Q^{*0} = 0.422$, $t_c = 0.50\,s$, $k = 1.4$, $H_{res} = 0.30\,m$ and $C_1 = 13$)

The effect of additional friction factor is further examined by solving two other test cases, in which Equation (4-24) is used for the friction factor. In these examples, the variables (V_a^{*0}, Q^{*0}) are $(1.05, 0.423)$, and $(0.94, 0.437)$, respectively. The results of these two examples are illustrated in Figures 4.8 and 4.9, respectively. As can be seen, in these test cases, compared to

the constant friction factor, the additional friction factor can help improve calculating the peak values and predicting the attenuation behavior similar to the previous example. Thus, these results can confirm that the proposed additional friction factor also offers benefits to other test cases.

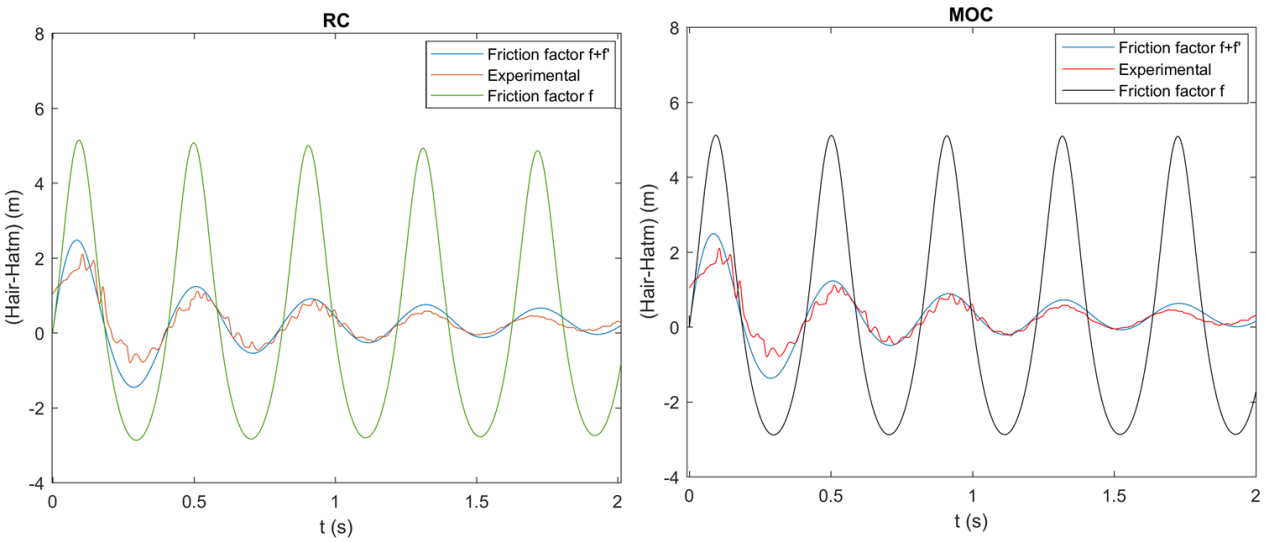

(a) (b)

Figure 4.8 The pressure distribution of the air pocket against time for (a) RC, and (b) MOC with Polytechnic Montreal experimental data ($V_a^{*0} = 1.05$, $Q^{*0} = 0.423$, $t_c = 0.44\ s$, $k = 1.4$, $H_{res} = 0.30\ m$ and $C_1 = 13$)

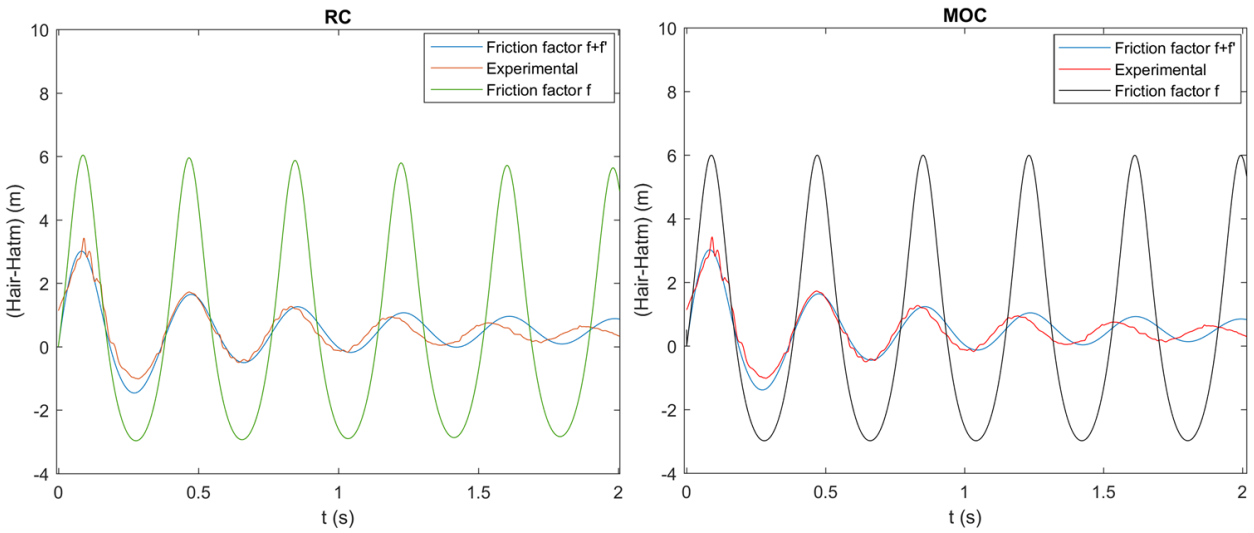

(a) (b)

Figure 4.9 The pressure distribution of the air pocket against time for (a) RC, and (b) MOC with Polytechnic Montreal experimental data ($V_a^{*0} = 0.94$, $Q^{*0} = 0.437$, $t_c = 0.40\ s, k = 1.4$, $H_{res} = 0.51\ m\ C_1 = 13$)

Equation (4-25) proposes the optimized value of the additional friction factor for a test case with (V_a^{*0}, Q^{*0}) equal to $(1.83, 0.406)$. This test case is considered as a representative for examples with large air pocket sizes. The relevant numerical pressure variation calculated by both the rigid column and the method of characteristics models are shown in Figure 4.10. As can be seen, compared to the steady-state friction factor, the additional friction factor can help both models capture the experimental data more accurately.

To show that the additional friction factor can improve the numerical solutions in other examples, Equation (4-25) is used to apply the additional friction factor to another example, in which the variables (V_a^{*0}, Q^{*0}) are $(1.68, 0.386)$. As shown in Figure 4.11, the additional friction factor effectively improves the numerical solutions of this example as well. Therefore, it can be claimed that the proposed formula for the additional friction factor can help in other examples as well. As can be seen, in these examples, in which the air pocket volume is larger, the phase shift between the numerical results and the experimental data is more significant than the test cases with smaller air pocket volume. The reason for this difference will be explained later.

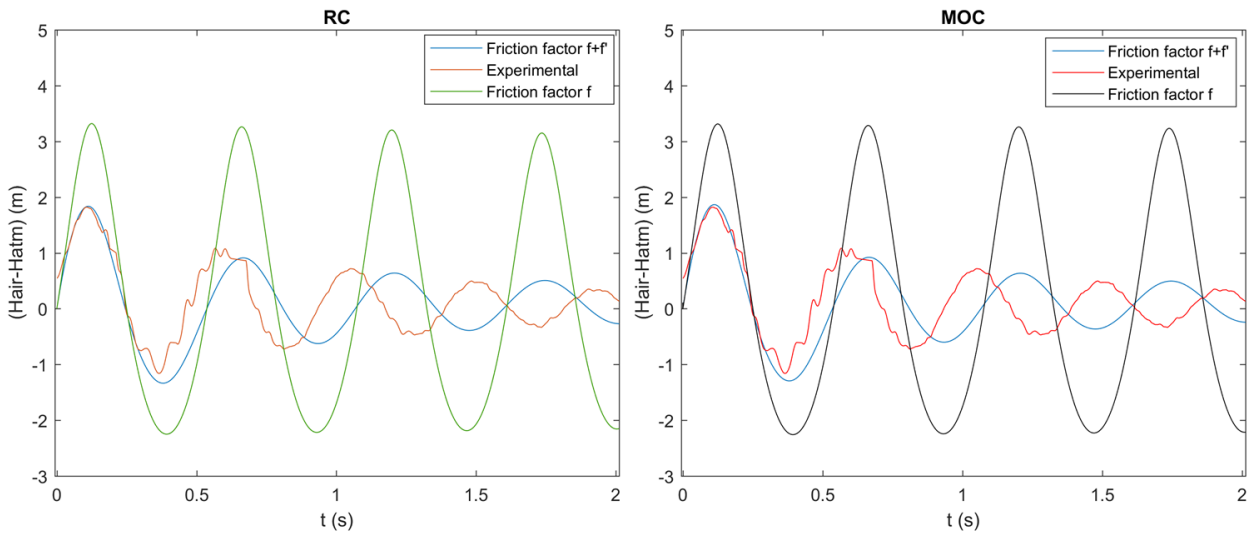

Figure 4.10 The pressure distribution of the air pocket against time for (a) RC, and (b) MOC with Polytechnic Montreal experimental data ($V_a^{*0} = 1.83$, $Q^{*0} = 0.406$, $t_c = 0.33\ s$, $k = 1.4$, $H_{res} = 0.11\ m$ and $C_2 = 4$)

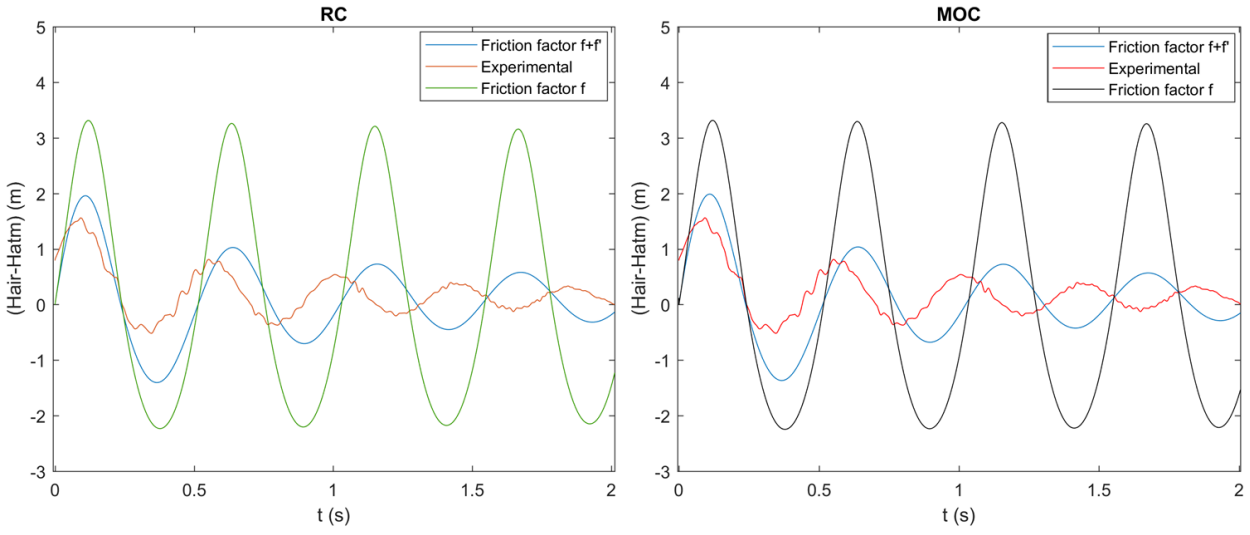

Figure 4.11 The pressure distribution of the air pocket against time for (a) RC, and (b) MOC with Polytechnic Montreal experimental data ($V_a^{*0} = 1.68$, $Q^{*0} = 0.386$, $t_c = 0.32\ s$, $k = 1.4$, $H_{res} = 0.12\ m$ and $C_2 = 4$)

In order to numerically evaluate the improvement provided by the additional friction factor, the percentage of the numerical error (ε) of each model was calculated as:

$$\varepsilon = \left| \frac{\sum_{i=1}^{np} \left(\left| h_p(i) \right| + |h_v(i)| - \left| h_{pe}(i) \right| - |h_{ve}(i)| \right)}{\sum_{i=1}^{np} \left(\left| h_{pe}(i) \right| + |h_{ve}(i)| \right)} \right|. \quad (4\text{-}26)$$

As shown in Table 4.1, for each test case, which was previously presented, the relative error with the friction factor $(f + f')$ is inferior to the relative error with only a steady-state friction factor (f) for both RC and MOC models.

Table 4.1 The relative error (ε) of the RC and MOC models with the steady-state friction factor and the additional friction factor

Test case	Relative error RC		Relative error MOC	
	$(f + f')$	(f)	$(f + f')$	(f)
$V_a^{*0} = 1.11$, $Q^{*0} = 0.422$, $t_c = 0.50\ s$, $k = 1.4$, $H_{res} = 0.30m$ and $C_1 = 13$ (shown in Figure 4.7)	4 %	307 %	8 %	314 %
$V_a^{*0} = 1.05$, $Q^{*0} = 0.423$, $t_c = 0.44\ s$, $k = 1.4$, $H_{res} = 0.30\ m$ and $C_1 = 13$ (shown in Figure 4.8)	25 %	405 %	20 %	413 %
$V_a^{*0} = 0.94$, $Q^{*0} = 0.437$, $t_c = 0.40\ s$, $k = 1.4$, $H_{res} = 0.51\ m$ $C_1 = 13$ (shown in Figure 4.9)	1 %	288 %	2 %	295 %
$V_a^{*0} = 1.83$, $Q^{*0} = 0.406$, $t_c = 0.33\ s$, $k = 1.4$, $H_{res} = 0.11\ m$ and $C_2 = 4$ (shown in Figure 4.10)	4 %	219 %	5 %	224 %
$V_a^{*0} = 1.68$, $Q^{*0} = 0.386$, $t_c = 0.32\ s$, $k = 1.4$, $H_{res} = 0.12\ m$ and $C_2 = 4$ (shown in Figure 4.11)	58 %	379 %	57 %	387 %

It should be noted that compared to the test cases with smaller air pocket sizes (Figures 4.7, 4.8, 4.9), for the test cases with larger air pocket sizes (Figures 4.10 & 4.11), the phase shift between the numerical solutions and experimental data is more obvious. The reason for this phase shift is not clearly determined yet. It could be due to the time lapse, which the valve takes to completely obstruct the pipe end. However, as can be seen in previous figures, the time lapse for all examples are almost in the same range, while the phase shift is more obvious for cases with larger air pocket sizes. Also, it was observed that the additional friction factor only affects the amplitude of the pressure oscillations not the phase shift. In addition, Wan et al. (2010) found that the friction resistances did not have much influence on the frequency of the hydraulic transient wave. Thus, this phase shift is more likely to occur due to the polytropic coefficient because Lee (2005) indicated that the frequency of the pressure distribution is affected by the polytropic coefficient. To further clarify this issue, in the test case with $V_a^{*0} = 1.83$, and $Q^{*0} = 0.406$, the polytropic coefficient was changed manually so that the phase shift can be removed. The results are shown in Figure 4.12. As can be seen, with a larger polytropic coefficient ($k = 1.9$), the phase shift between experimental data and numerical results of both models can be removed. It is also worth mentioning that similar phase shift was reported in other studies (e.g. Rokhzadi and Fuamba, 2020b; Hatcher et al., 2015; Vasconcelos et al., 2011). Another reason could be due to neglecting the free-surface flow zone. Indeed, it can specifically be seen in Eq. (40) of Rokhzadi and Fuamba, 2020b, that the phase of the general solutions (terms under the root square), depends on the water column length (L_u). Note that the water column length is equal to $L_t - L_a$, in which L_a is the air pocket length or, equivalently, free-surface flow length.

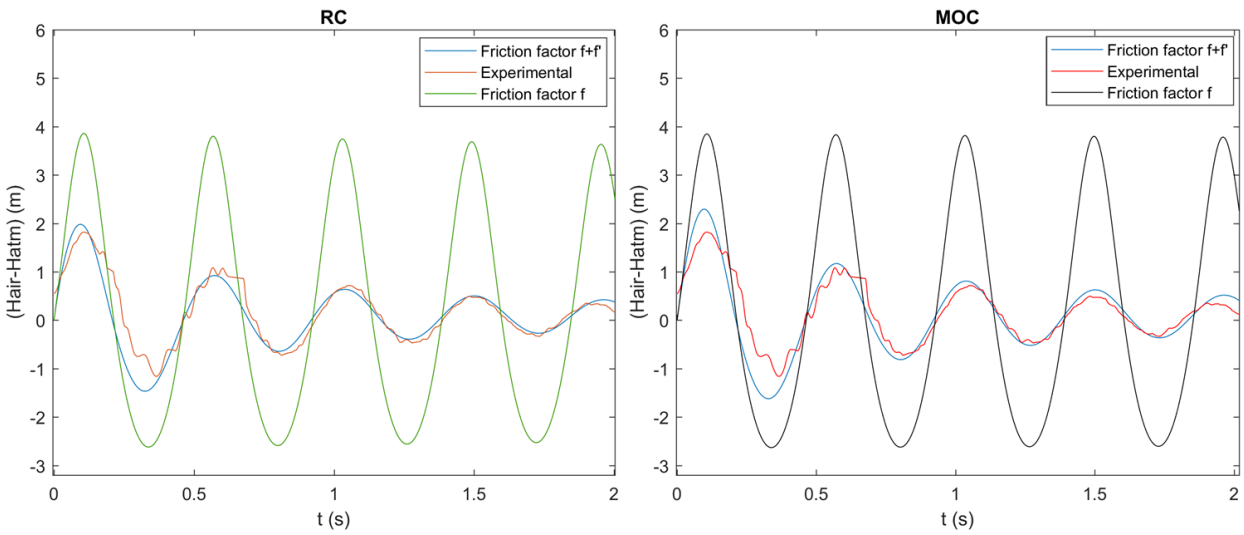

Figure 4.12 The pressure of the air pocket against time for (a) RC, and (b) MOC with Polytechnic Montreal experimental data ($V_a^{*0} = 1.83$, $Q^{*0} = 0.406$, $t_c = 0.33\ s$, $k = 1.9$ and $H_{res} = 0.11\ m$)

Since the experimental data of the discharge and air volume are not available, only the numerical results calculated by the rigid column model are plotted against the time and shown in Figure 4.13 for the first test case ($V_a^{*0} = 1.11$, $Q^{*0} = 0.422$, $t_c = 0.50\ s$, $k = 1.4$ and $H_{res} = 0.30\ m$). In this figure, the positive effects of the additional friction factor on the discharge and the air volume can be seen. It can be noticed that the behavior of the air pocket volume is opposite of the air pressure, which can be explained by the polytropic equation. The graph of the air volume also shows that the air pocket undergoes cycles of compression and expansion.

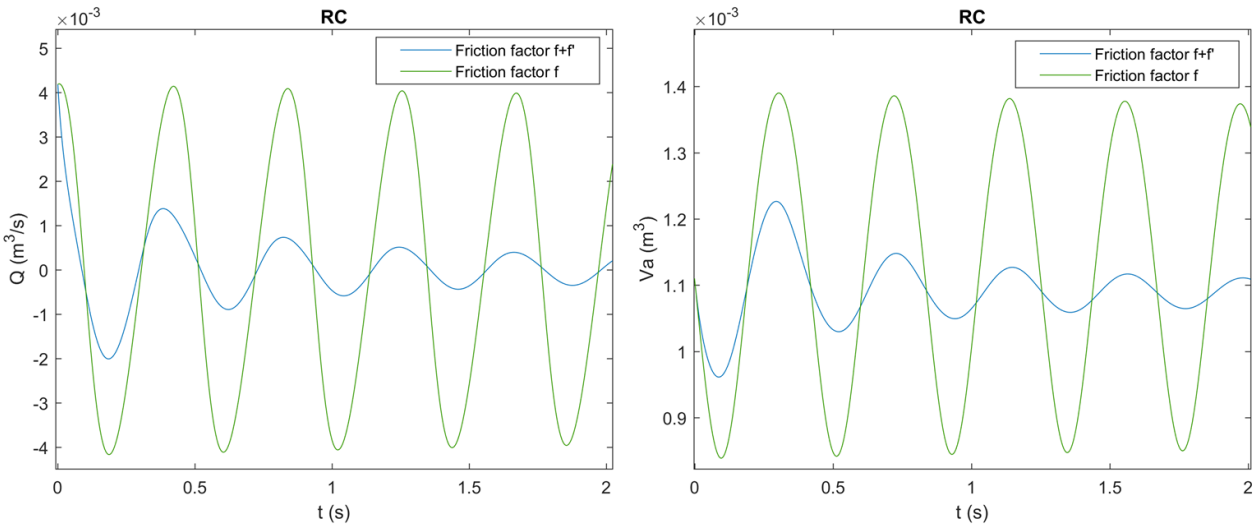

(a) (b)

Figure 4.13 (a) the discharge, and (b) the air volume against time, calculated by the rigid column model with Polytechnic Montreal experimental data ($V_a^{*0} = 1.11$, $Q^{*0} = 0.422$, $t_c = 0.50\ s$, $k = 1.4$ and $H_{res} = 0.30\ m$)

The method used in the article is based on the calibration of an additional friction factor f' which has a form similar to the Darcy-Weisbach friction factor. The calibration of the factor C allows to consider without distinction all types of energy loss: pipe friction, air-water interaction, turbulence, eventual heat transfer, viscoelastic effect, etc. Therefore, it seems to be more practical and easy to implement.

It is worth mentioning that in the method used in this article, the optimal calibration factor was obtained by using the experimental data for specific examples, which are considered as representatives of other examples. However, in future studies, an analytical formula may be obtained for the optimal factor C without having to calibrate it experimentally.

4.3.2 Zhou (2000) experimental data

Some experiments of Zhou (2000) are also similar to those done in the laboratory of Polytechnic Montréal, besides other cases, in which the air release problems and the effects of orifice size d were studied. Thus, two cases of Zhou (2000) will be analyzed in this article, in which the air pocket is entrapped, i.e. $d = 0$.

The supply pressure tank is 120 cm high and 42 cm in diameter. The pipe is horizontal and 8.96 m long and consisted of two galvanized steel sections and one Plexiglas pipe section. Initially, the water and air occupying upstream and downstream, respectively, are separated by a valve. In both experiments, the non-dimensional reservoir pressure is $H_0^*/H_b^* = 2.43$, in which H_0^* represents the absolute reservoir pressure head equal to $H_{res} + H_{atm}$ and H_b^* represents the absolute atmospheric pressure head equal to H_{atm}. Zhou (2000) assumes a polytropic coefficient $k = 1.4$ so the same value will be assumed for numerical comparison with Zhou (2000) test cases.

The first test case is characterized by a relative water column length of $\lambda_0 = L/L_t = 0.56$ (or a water column length $L = 5\,m$), an acoustic wave speed of $a = 200\,m/s$, a steady-state friction factor of $f = 0.035$ and a local head loss coefficient as $K_{loss} = 0.093$.

The second test case is characterized by a relative water column length of $\lambda_0 = 0.89$ (or a water column length $L = 8\,m$), an acoustic wave speed of $a = 700\,m/s$, a steady-state friction factor of $f = 0.035$ and $K_{loss} = 0.093$.

As shown in Figures 4.14 and 4.15, the additional friction factor helps to better approximate the pressure attenuation. A slight phase shift is observed and the reason for that was already discussed in the previous section.

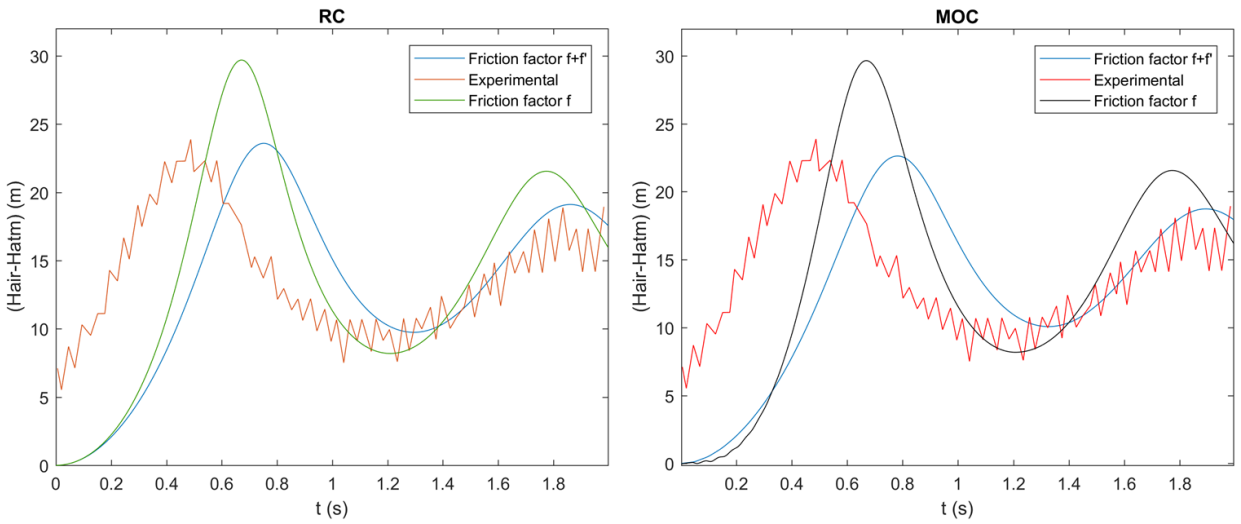

Figure 4.14 The pressure of the air pocket against time for (a) RC, and (b) MOC with Zhou (2000) ($V_a^{*0} = 88.4$, $Q^{*0} = 0$, $\lambda_0 = 0.56$, $k = 1.4$, $d/D = 0$, $y/D = 0$ and $H_0^*/H_b^* = 2.43$)

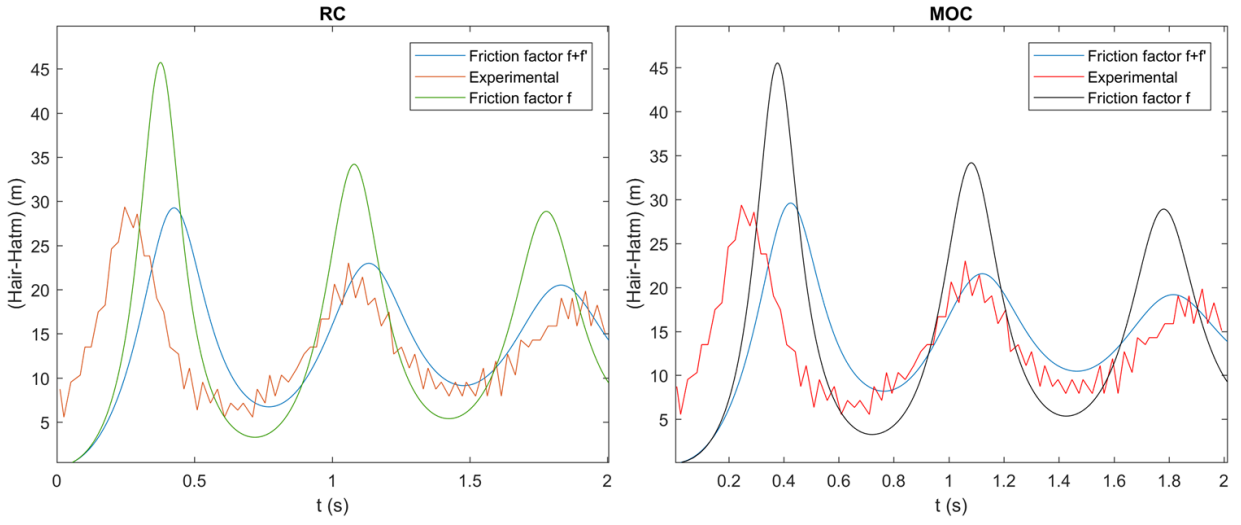

Figure 4.15 The pressure of the air pocket against time for (a) RC, and (b) MOC with Zhou (2000) ($V_a^{*0} = 22.1$, $Q^{*0} = 0$, $\lambda_0 = 0.89$, $k = 1.4$, $d/D = 0$, $y/D = 0$ and $H_0^*/H_b^* = 2.43$)

4.3.3 Hatcher et al. (2015) experimental data

Some of experiments of Hatcher et al. (2015), for which the reservoir volume size is $0.66\,m^3$ with a plan area of $0.50\,m^2$, are also analysed in this paper. The test case chosen for comparison was carried out with a clear PVC pipeline of length $L_{pipe} = 10.7\,m$, diameter $D = 0.053\,m$ and slope $S_0 = 0.02$. The other characteristics of this experiment are local head loss coefficient $K_{loss} = 2.9$, initial air pocket volume $V_a^{*0} = 1.29$, and initial flow discharge $Q^{*0} = 0.21$.

Since the steady-state friction factor (f), the water level in the reservoir (H_{res}) and the acoustic wave speed were not found in the article of Hatcher et al. (2015), it was assumed that f is equal to 0.025, the water level in the reservoir was determined by the energy equation as $H_{res} = 0.204\,m$, and the acoustic wave speed was approximated by Equation (4-22).

Hatcher et al. (2015) assumes a polytropic coefficient with $k = 1.2$ and used the dimensionless time $t^* = t/V_a^{1/3}/\sqrt{gD}$. Thus, the same parameters will be used for numerical comparison with Hatcher et al. (2015) test case. As can be seen in Figure 4.16, similar to other test cases, the additional friction factor is also effective on this test case as well.

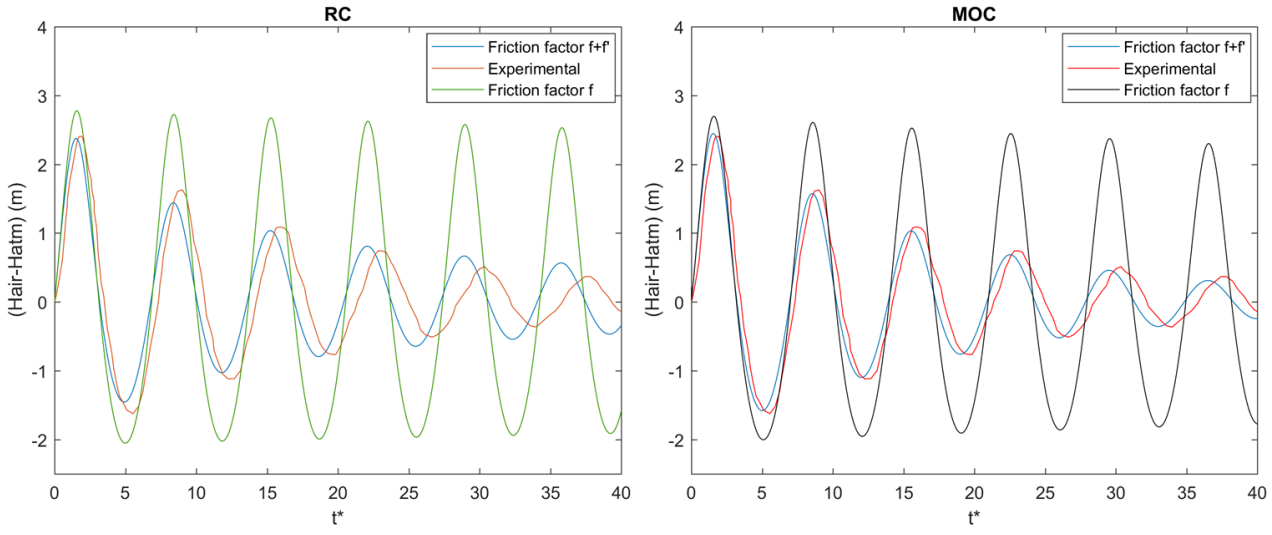

Figure 4.16 The pressure of the air pocket against time for (a) RC, and (b) MOC with Hatcher et al. (2015) ($V_a^{*0} = 1.29$, $Q^{*0} = 0.21$ and $k = 1.2$)

4.4 Conclusion

In this paper, the transient partially pressurized flow following the air entrapment caused by valve obstruction in a closed conduit has been studied and the effects of friction loss have been analyzed. Since the flow is unsteady, using the steady-state Darcy-Weisbach friction factor to calculate the friction losses is too simplified approximation. Thus, a formula has been proposed, in which the additional friction factor is a function of influential variables including the density and the length of air and water phases, and the reservoir pressure. This formula, based on the Darcy-Weisbach formula, has been optimized for two different air pocket sizes to show the effect of air pocket size on the friction loss.

The ability of the proposed additional friction factor has been examined by solving different examples with different air and water lengths, different pipe diameters, different acoustic wave speeds, and different reservoir pressures. Two well-known mathematical models have been used for numerical calculation, which the results have been compared to the corresponding experimental data. These models include the rigid column model solved by the classical 4^{th} order Runge-Kutta scheme, called RC, and a modified version of the Saint-Venant equations solved by method of characteristics, called MOC.

It was found that both models by using the steady-state friction factor overestimate the pressure peak values and they predict insufficient pressure attenuation. However, by using the additional friction factor, both models calculate the peak values more accurately and predict the attenuation behaviors of the pressure distribution more properly. Although the additional friction factor was optimized for two specific examples, it was proved that it can help in similar problems and different mathematical models to improve the quality of the numerical solutions. Also, it was found that the magnitude of the additional friction factor has an inverse relation with the size of the air pocket. It was shown that the additional friction factor only has effects on damping the extra energy so that it offers the aforementioned improvements. Therefore, the phase shift that is observed between the experimental and numerical results is not due to this parameter. This phase shift was only observed for test cases with large air pocket sizes. Thus, it could be caused by the simplified thermodynamic model applied to the air pocket. This fact has been proved using a different polytropic coefficient, by which the phase shift between experimental data and numerical result can be removed.

CHAPTER 5 OTHER APPLICATION CASES OF THE ADDITIONAL FRICTION FACTOR

5.1 Introduction

The problem studied in this chapter is similar to Chapter 4. Compared to the experiments carried out in Chapter 4 in the hydraulics laboratory of "École Polytechnique de Montreal", Hatcher et al. (2015) considered different pipe diameters $D = 53\,mm$ and $102\,mm$ and total lengths $L_{pipe} = 10.7$ and $12\,m$ and adverse slopes $S = 2$ and 1.3 %, respectively. In Chapter 4, only pressure graphs were plotted whereas Hatcher et al. (2015) also plotted flow rate hydrographs. Thus, it is useful to compare numerical models with experimental data of Hatcher et al. (2015).

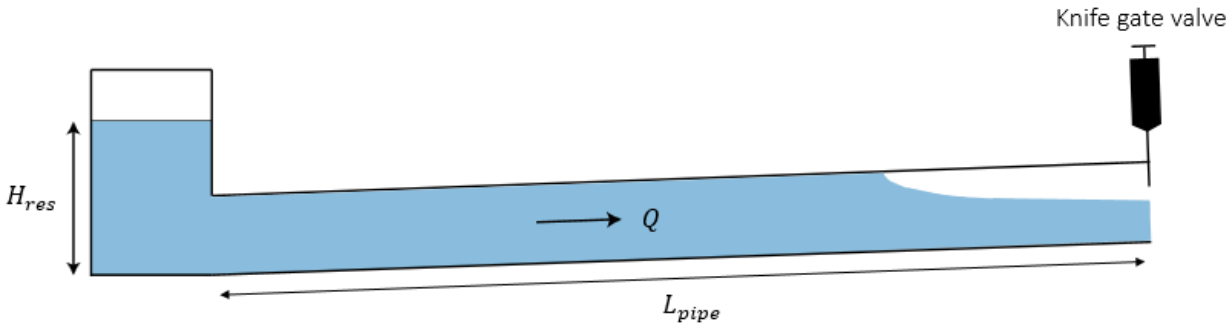

Figure 5.1 Illustration of the entrapped air pocket experiments of Hatcher et al. (2015)

By assuming a vertical interface between air and water phases, the problem shown with a closed valve in Figure 5.1 is equivalent to the one shown in Figure 5.2. An equivalent pressurized zone is represented by the length of the rigid column L.

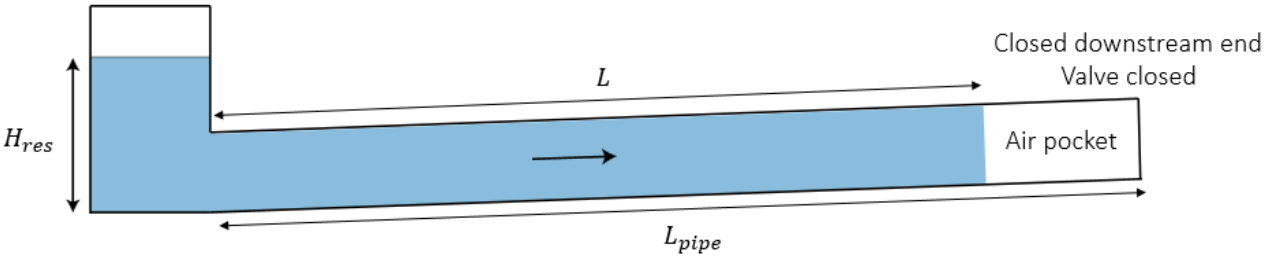

Figure 5.2 Illustration of the equivalent problem of Figure 5.1 represented by the length of the rigid column L

5.2 Methodology

Note that the same models, the rigid column model and the method of characteristics model, as Chapter 4 will be used in this chapter. Each models will be explained with more details in this section than in Chapter 4. The water level in the reservoir is not given in Hatcher et al. (2015). Therefore, it is approximated with the Bernoulli equation applied between a point in the reservoir and the last point of the pressurized zone:

$$H_{res} = -LS_0 + \left(\frac{fL}{D} + K_{loss}\right) \times \frac{Q^2}{2gA^2}. \quad (5\text{-}1)$$

A little error in the approximation of H_{res} does not affect the following results found in this chapter, it just slightly modifies the value of the calibration factor C. The value of H_{res} is between 0.2 and $0.3\ m$ using equation (5-1).

Hatcher et al. (2015) used dimensionless parameters (t^*, Q^* and V_a^*) to plot the graphs of pressure against time and discharge against time. The parameters are:

Dimensionless time parameter : $t^* = t/V_a^{1/3}/\sqrt{gD}$ (5-2)

Dimensionless flow rate : $Q^* = Q/\sqrt{gD^5}$ (5-3)

Dimensionless volume of air : $V_a^* = V_a/D^3$ (5-4)

The same dimensionless parameters will be used in this chapter.

From Vasconcelos and Leite (2012) and Hatcher et al. (2015), the steady friction factor (Darcy-Weisbach) $f = 0.025$, the polytropic coefficient $k = 1.2$, and the summation of local losses $K_{loss} = 2.9$ will be used in this chapter.

5.2.1 Rigid column model

The concept of the rigid column model is based on neglecting the water compressibility so that the velocity and pressure are space-invariant variables throughout the pressurized flow, which is assumed as a rigid water column.

Following other references, exemplified by Hatcher et al. (2015), Vasconcelos and Leite (2012), Vasconcelos et al. (2011b), and Zhou et al. (2002), by using the rigid column model, the air-water interface is assumed to be vertical so that the free-surface flow zone is neglected. Thus, the governing equations include the momentum equation of the water column, equation (5-5), and the continuity equation, equation (5-6), and the time derivative of the polytropic process relationship of the ideal gas law, equation (5-7), applied to the air pocket.

$$\frac{dQ}{dt} = \frac{gA}{L}\left[H_{res} - (H_{air} - H_{atm}) - \left(\left(f\frac{L}{D} + K_{loss}\right)\frac{Q|Q|}{2gA^2}\right)\right], \tag{5-5}$$

$$\frac{dV_a}{dt} = -Q, \tag{5-6}$$

$$\frac{dH_{air}}{dt} = -k\frac{H_{air}}{V_a} \times \frac{dV_a}{dt}, \tag{5-7}$$

where t is the time variable, Q is the discharge, V_a is the air pocket volume, H_{air} is the air phase absolute pressure head, H_{atm} is the atmospheric absolute pressure head, which is set to 10.33 m, L is the equivalent water column length, which is explained later. In addition, D is the pipe diameter, A is the cross-sectional area of the pipe, f is the Darcy-Weisbach steady-state friction factor, K_{loss} is the summation of local losses, and k is the polytropic coefficient.

Note that the equivalent water column length is calculated as:

$$L = \frac{L_{pipe}A - V_a}{A}, \tag{5-8}$$

to compensate for the water volume of the free-surface flow, which is neglected in applying the rigid column model.

The set of equations (5-5), (5-6), and (5-7) of the rigid column model is solved by using the classical 4th order Runge-Kutta method as described in other references (e.g. Rokhzadi and Fuamba 2020a; Press et al. 2007). Considering a general ordinary differential equation (ODE) problem as:

$$\frac{d\psi}{dt} = F(\psi), \tag{5-9}$$

where ψ is any time dependent variable and F is any continuous function of ψ. The classical 4th order Runge-Kutta scheme uses four internal stages in which the solution of equation (5-9), shown as ψ^i $(\mathrm{i} = 1, \cdots, 4)$, are calculated. Then, this scheme steps forward to calculate the solution at the final stage which is the time step $\mathrm{n} + 1$. These calculations can be presented as follows:

$$\psi^1 = \psi^n,$$

$$\psi^2 = \psi^n + \frac{1}{2}\Delta t F(\psi^1),$$

$$\psi^3 = \psi^n + \frac{1}{2}\Delta t F(\psi^2), \tag{5-10}$$

$$\psi^4 = \psi^n + \Delta t F(\psi^3),$$

$$\psi^{n+1} = \psi^n + \Delta t \left[\frac{1}{6}F(\psi^1) + \frac{1}{3}F(\psi^2) + \frac{1}{3}F(\psi^3) + \frac{1}{6}F(\psi^4)\right],$$

where Δt is the time step size and the superscript n represents the current time step. Note that the initial conditions will be explained later.

In addition, for further clarification, the calculation procedure of the rigid column model is shown in Figure 5.3.

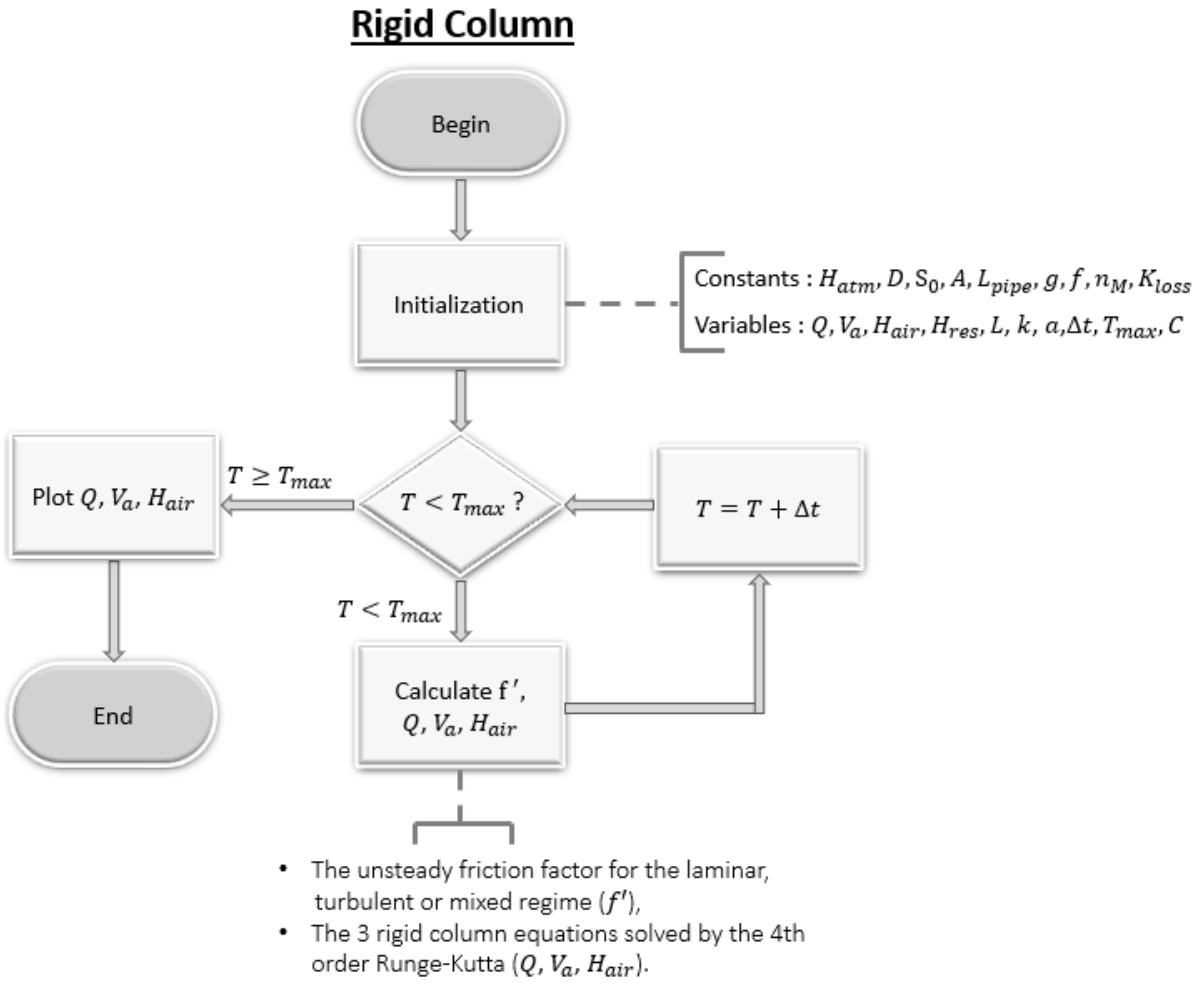

Figure 5.3 The calculations procedure for the rigid column model

5.2.2 Method of characteristics model

The governing equations for one-dimensional flow in closed conduits constitute a pair of partial differential equations (PDEs), which are the continuity and momentum equations, respectively, (Wylie and Streeter, 1993; Chaudhry. 2014):

$$\begin{cases} \dfrac{\partial V}{\partial t} + g\dfrac{\partial H}{\partial x} + \dfrac{f|V|V}{2D} = 0 \\ \dfrac{\partial H}{\partial t} + \dfrac{a^2}{g}\dfrac{\partial V}{\partial x} = 0 \end{cases}, \tag{5-11}$$

where V is the water velocity, H is the piezometric head, a is the acoustic wave speed, and x is the spatial variable along the pipe axis with the positive direction from the upstream to the downstream.

The method of characteristics is a numerical method with first order of accuracy, which has been commonly used to solve the water hammer equations. The method of characteristics allows to transform the pair of PDEs, equation (5-10), into two ODEs along two positive and negative characteristics as presented below. Note that further details of this method can be found in other references (e.g. Wylie and Streeter 1993).

Positive characteristic $C^+ : \frac{g}{a}\frac{dH}{dt} + \frac{dV}{dt} + \frac{fV|V|}{2D} = 0.$ (5-12)

Negative characteristic $C^- : -\frac{g}{a}\frac{dH}{dt} + \frac{dV}{dt} + \frac{fV|V|}{2D} = 0.$ (5-13)

Note that the positive and negative characteristic lines, corresponding to (5-12) and (5-13) can be determined, respectively, by equations (5-14) and (5-15).

$\frac{dx}{dt} = +a.$ (5-14)

$\frac{dx}{dt} = -a.$ (5-15)

Equations. (5-12) and (5-13) are called the compatibility equations. As shown in Figure 5.4, the unknown variables at the time step $(n + 1)$ for a grid point (P) can be calculated using the solutions at R and S, corresponding to the current time step (n). Therefore, the compatibility equations, equations (5-12) and (5-13), are integrated along the characteristic lines C^+, and C^-, respectively, as presented in equations (5-16) and (5-17).

$C^+: \ H_P = H_R - \frac{a}{gA} \times (Q_P - Q_R) - \frac{f\Delta x}{2gDA^2} Q_R|Q_R|.$ (5-16)

$C^-: \ H_P = H_S + \frac{a}{gA} \times (Q_P - Q_S) + \frac{f\Delta x}{2gDA^2} Q_S|Q_S|.$ (5-17)

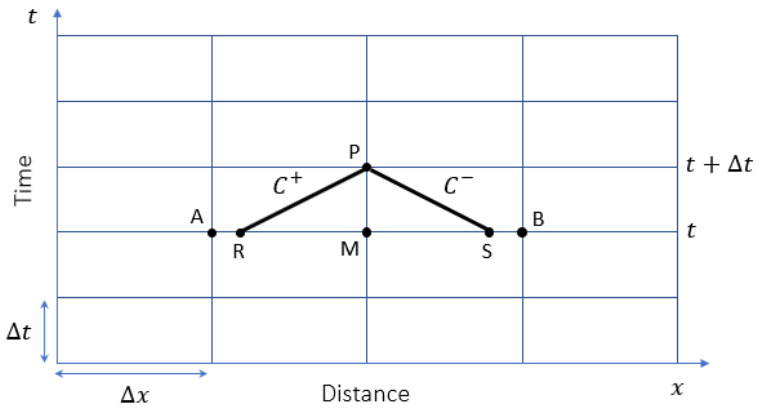

Figure 5.4 The characteristic lines in the space-time plane

It is possible that the characteristic lines C^+ and C^- do not intersect the time line exactly at grid points. Therefore, the intersection points R, and S can be different from the grid points A, and B. Since the pressure head and discharge values (H, Q) at grid points A and B are known, the pressure head and discharge at R (H_R, Q_R) and at S (H_S, Q_S) can be obtained by linear interpolations, as presented in equations (5-18) and (5-19).

$$\begin{cases} H_R = H_M + CFL(H_A - H_M) \\ Q_R = Q_M + CFL(Q_A - Q_M) \end{cases}. \tag{5-18}$$

$$\begin{cases} H_S = H_P + CFL(H_B - H_P) \\ Q_S = Q_P + CFL(Q_B - Q_P) \end{cases}. \tag{5-19}$$

It is known that the time step (Δt) is calculated with the Courant-Friedrichs-Lewy (CFL) condition:

$$\Delta t = CFL \frac{\Delta x}{|a| + max\,(|V|)}, \tag{5-20}$$

where Δx is the size of the grid network and $max(|V|)$ represents the maximum of the absolute values of the velocity in the pressurized zone. Note that in the present paper, CFL is set to 0.9. It is worth mentioning that the number of nodes used to discretize the pressurized flow zone is 20. However, finer grid network sizes were also examined to confirm that the numerical solutions do not depend on the number of discretization nodes.

Note that equation (5-6) is used to calculate the air pocket volumetric change. Thus, the air pocket volume at the new time step is calculated as:

$$V_a^{n+1} = V_a^n - \Delta t Q_N^n, \tag{5-21}$$

by which the air pocket pressure head at the new time step is calculated using the polytropic process equation as:

$$H_{air}^{n+1} = H_{air}^n \left(\frac{V_a^{n+1}}{V_a^n} \right)^k. \tag{5-22}$$

Boundary conditions:

For the first node of the pressurized flow zone at the upstream (the one near the reservoir), only the negative characteristic C^-, which originates somewhere between the first and second nodes, can be used for the calculation. Thus, for the first node, the energy equation between the reservoir and the first node of the pressurized zone is used instead of the equation along the positive characteristic:

$$H_1^{n+1} = (H_{res} + H_{atm}) - (1 + K_{loss}) \times \frac{Q_1^n |Q_1^n|}{2gA^2}, \tag{5-23}$$

where the subscript (1) denotes the first node of the pressurized flow zone.

For the last node of the pressurized flow zone (the one near the air pocket), only the equation along the positive characteristic C^+ can be used. Therefore, instead of the negative characteristic line, the energy equation between the last node of the pressurized zone and the air pocket is used:

$$H_N^{n+1} = H_{air}^{n+1} - \frac{Q_N^{n+1} |Q_N^{n+1}|}{2gA^2}, \tag{5-24}$$

where N represents the last node of the pressurized flow zone.

In addition, for further clarification, the calculation procedure of the method of characteristics model is shown in Figure 5.5.

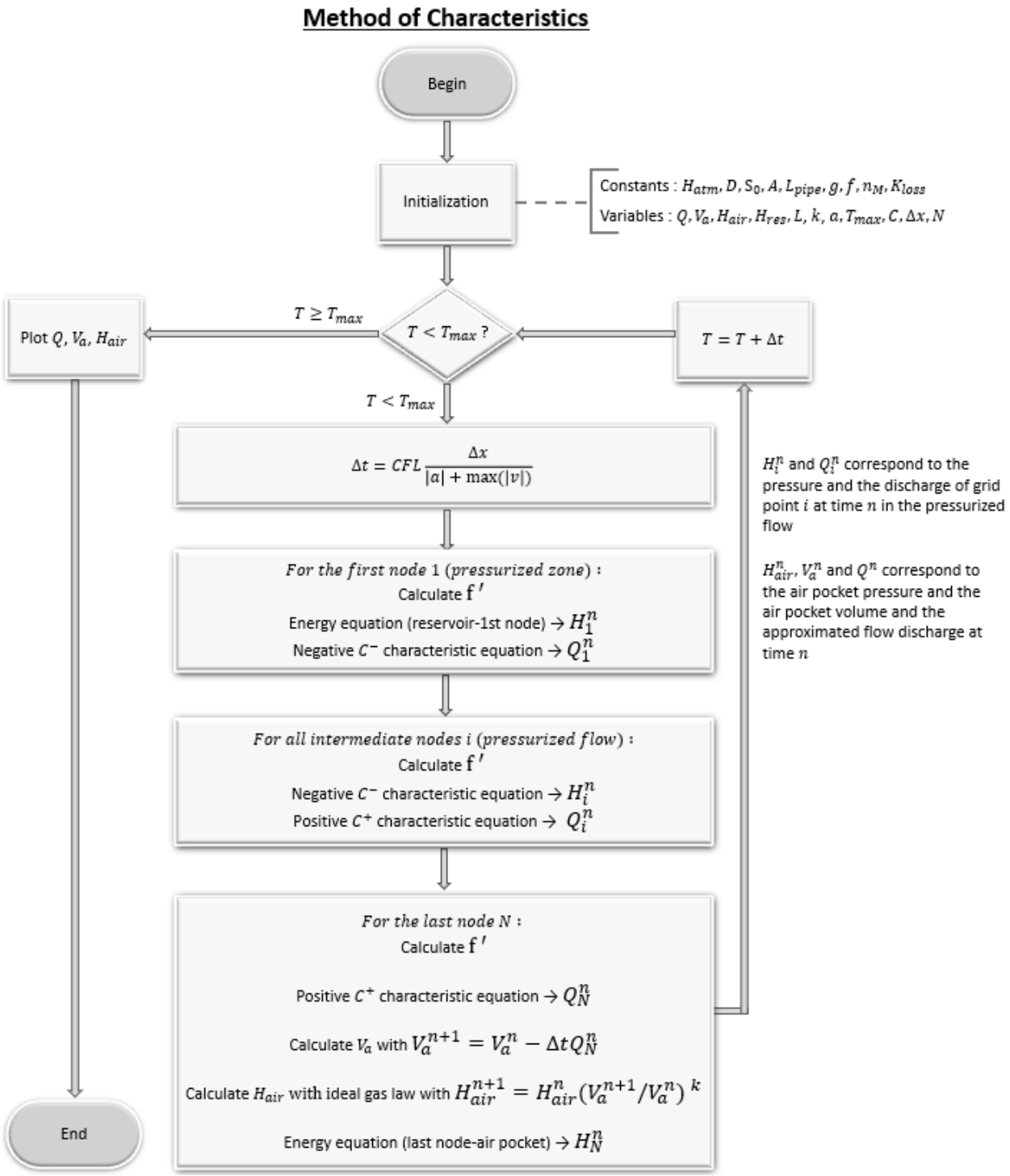

Figure 5.5 The calculations procedure for the method of characteristics model

5.3 Results

The code written in MATLAB for the rigid column model with an additional friction factor and a calibration factor C can be found in Appendix A and the one for the method of characteristics can be found in Appendix B.

5.3.1 Steady friction factor and polytropic coefficient k=1.2

Hatcher et al. (2015) already showed the pressure hydrographs and flow rate hydrographs (Figures 5 and 6 of their article) obtained with the rigid column and the method of characteristics models with a steady friction factor and a polytropic coefficient $k = 1.2$ for several sizes of air pocket. The pressure and flow rate hydrographs of test cases of Hatcher et al. (2015) were produced again in

Figure 5.6, Figure 5.7, Figure 5.8, Figure 5.9, Figure 5.10, and Figure 5.11 with the numerical codes used in this project because the results with a steady friction factor and with an additional friction factor will be compared. Since some information were not given by Hatcher et al. (2015) such as the water level in the reservoir (H_{res}) or the speed of the pressure wave (a), the pressure peaks and discharge can be slightly different but the general behavior is preserved.

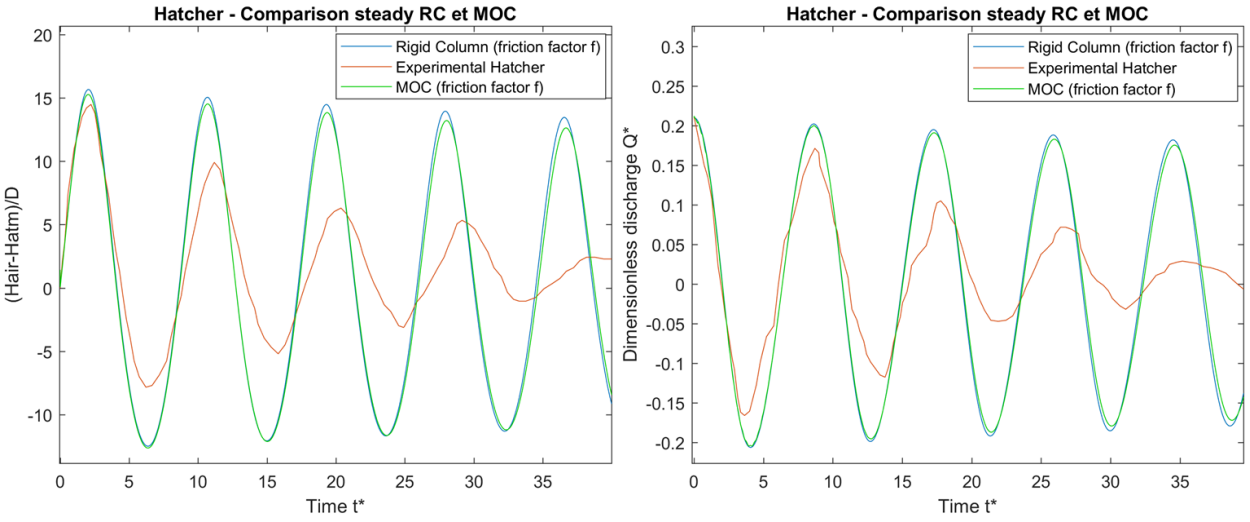

Figure 5.6 The dimensionless air pocket (left) and dimensionless discharge (right) against time with steady friction factor for $V_a^{*0} = 3.70$, $Q^{*0} = 0.21$, $D = 0.102\ m$, $L = 12m$, $S_0 = 1.3\%$, $k = 1.2$, and the experimental data of Hatcher et al. (2015)

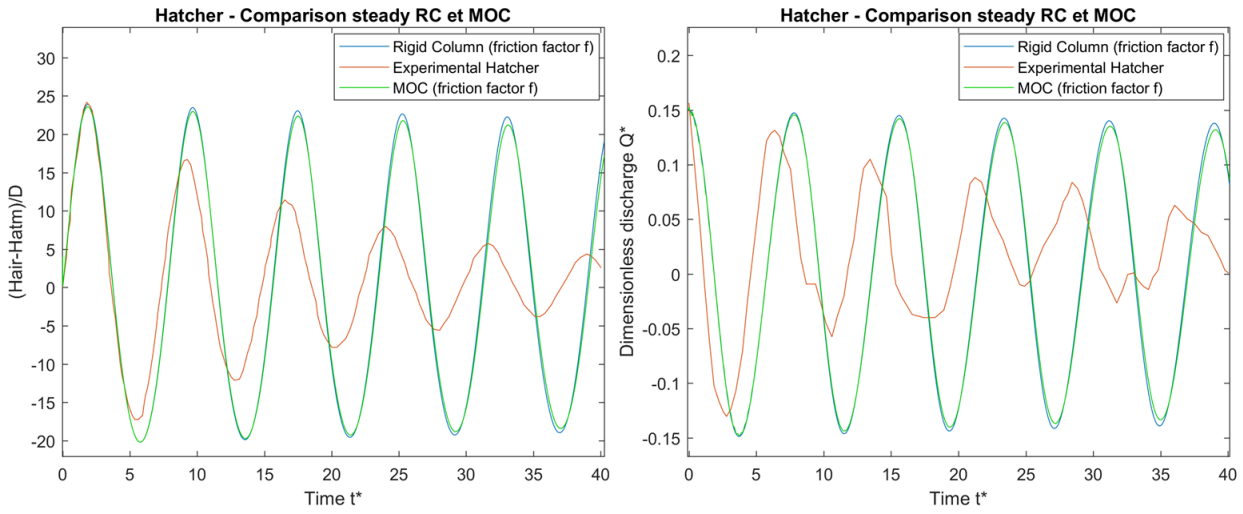

Figure 5.7 The dimensionless air pocket (left) and dimensionless discharge (right) against time with steady friction factor for $V_a^{*0} = 2.63$, $Q^{*0} = 0.15$, $D = 0.053\ m$, $L = 10.7\ m$, $S_0 = 2\%$, $k = 1.2$, and the experimental data of Hatcher et al. (2015)

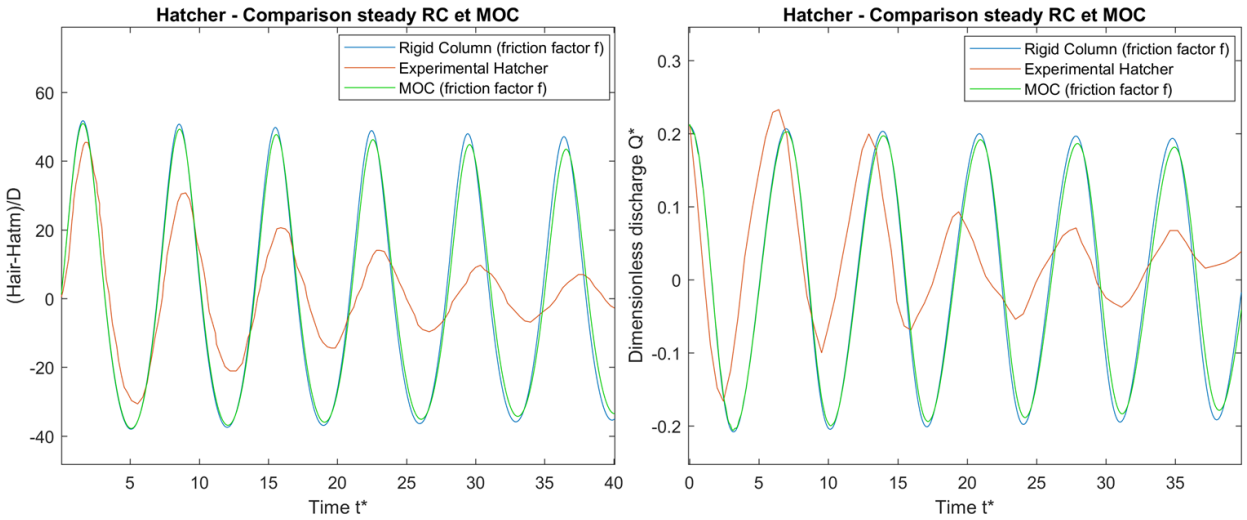

Figure 5.8 The dimensionless air pocket (left) and dimensionless discharge (right) against time with steady friction factor for $V_a^{*0} = 1.29$, $Q^{*0} = 0.21$, $D = 0.053\ m$, $L = 10.7\ m$, $S_0 = 2\%$, $k = 1.2$, and the experimental data of Hatcher et al. (2015)

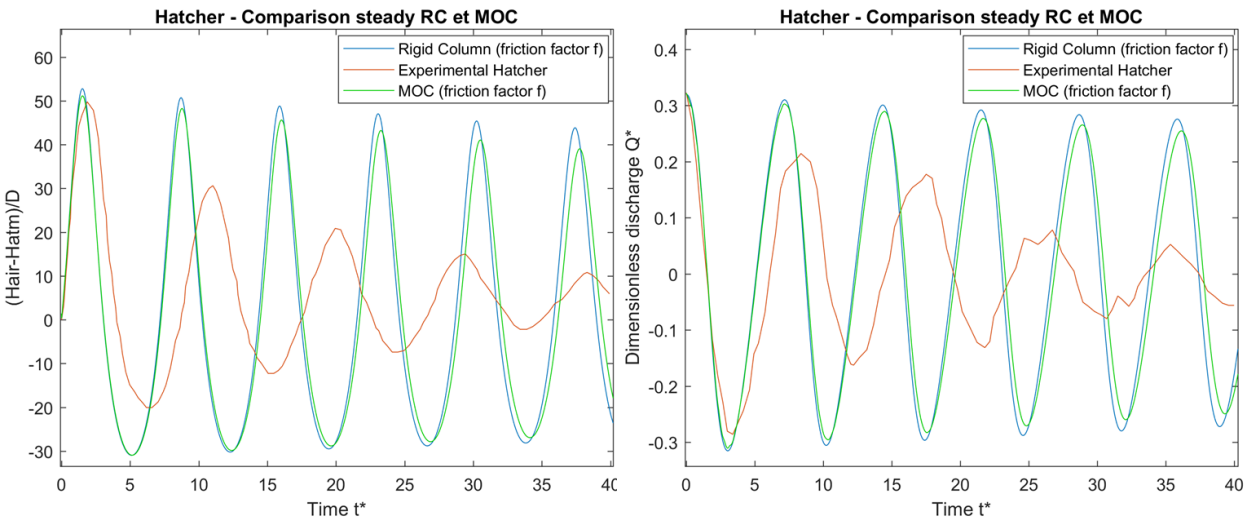

Figure 5.9 The dimensionless air pocket (left) and dimensionless discharge (right) against time with steady friction factor for $V_a^{*0} = 1.10$, $Q^{*0} = 0.32$, $D = 0.102\ m$, $L = 12\ m$, $S_0 = 1.3\%$, $k = 1.2$, and the experimental data of Hatcher et al. (2015)

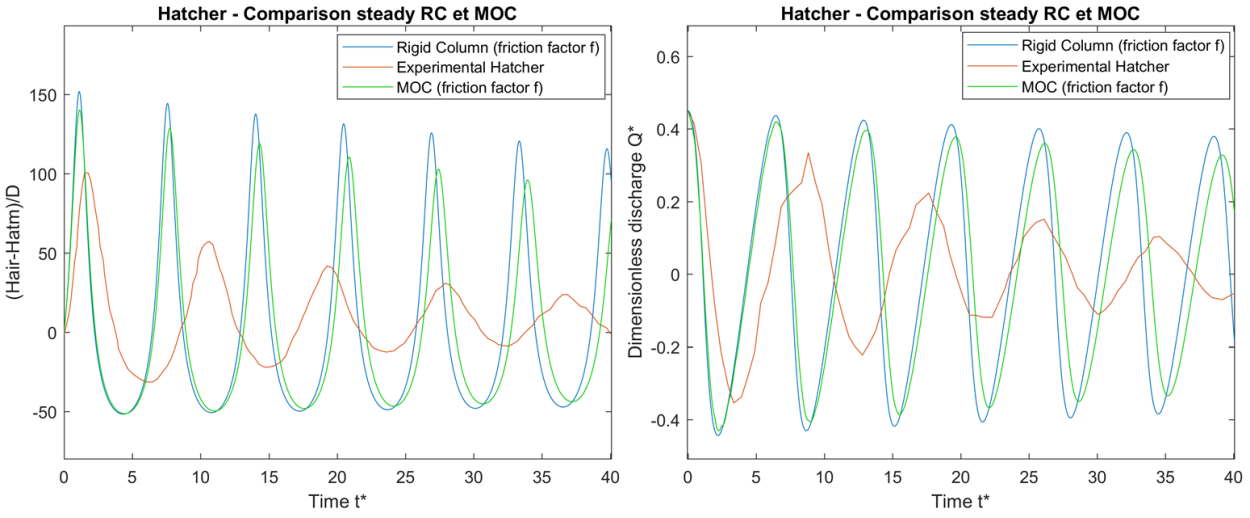

Figure 5.10 The dimensionless air pocket (left) and dimensionless discharge (right) against time with steady friction factor for $V_a^{*0} = 0.51$, $Q^{*0} = 0.45$, $D = 0.102\ m$, $L = 12\ m$, $S_0 = 1.3\%$, $k = 1.2$, and the experimental data of Hatcher et al. (2015)

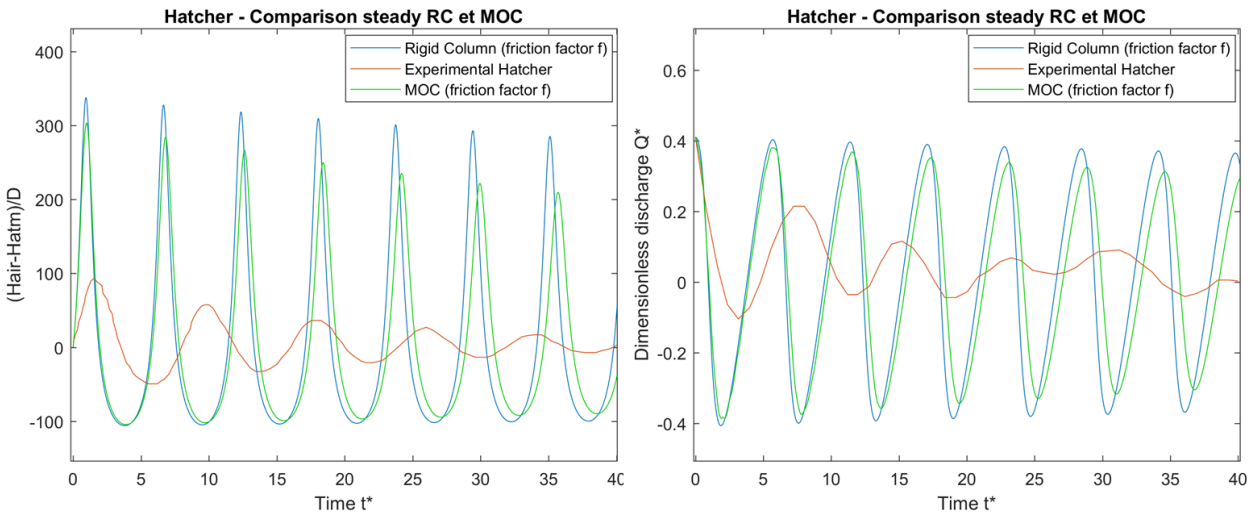

Figure 5.11 The dimensionless air pocket (left) and dimensionless discharge (right) against time with steady friction factor for $V_a^{*0} = 0.32$, $Q^{*0} = 0.41$, $D = 0.053\ m$, $L = 10.7\ m$, $S_0 = 2\%$, $k = 1.2$, and the experimental data of Hatcher et al. (2015)

The numerical pressure and discharge peaks are clearly overestimated with the steady-state friction factor. This overestimation is even greater for small air pockets. Phase shift can also be observed for certain air pocket sizes which can be especially seen in Figure 5.9, Figure 5.10, and Figure 5.11. Note that the phase shift can also be reported by Hatcher et al. (2015).

5.3.2 Additional friction factor and polytropic coefficient k=1.2

The results of the rigid column model, and the method of characteristics model with the additional friction factor and a constant polytropic coefficient $k = 1.2$ are given in Figure 5.12, Figure 5.13, Figure 5.14, Figure 5.15, Figure 5.16 and Figure 5.17. The optimal factor C is calculated for each size of air pocket.

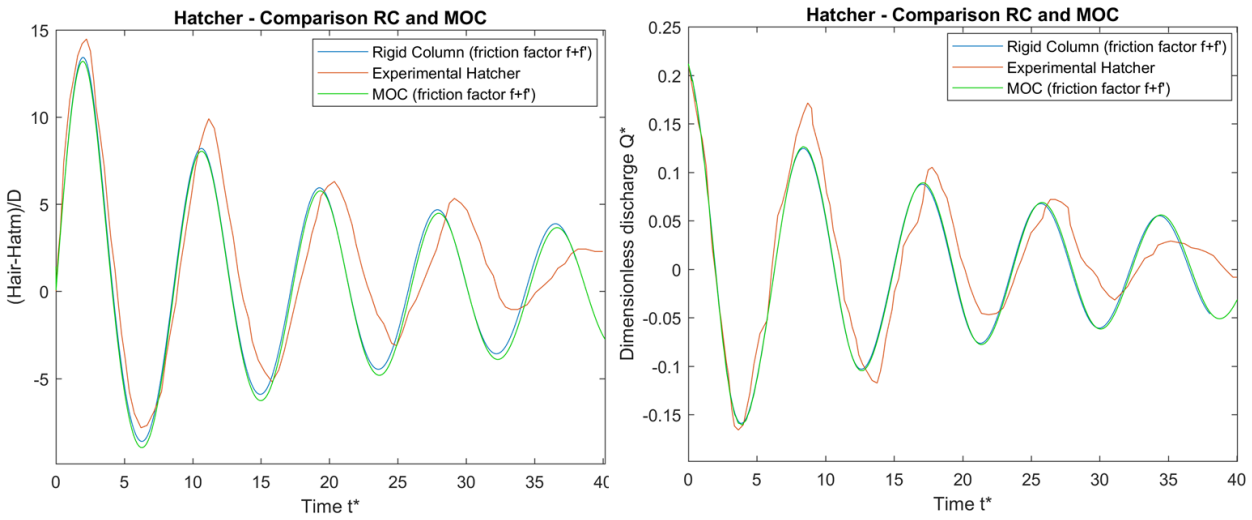

Figure 5.12 The dimensionless air pocket (left) and dimensionless discharge (right) against time with additional friction factor for $V_a^{*0} = 3.70$, $Q^{*0} = 0.21$, $D = 0.102\ m$, $L = 12\ m$, $S_0 = 1.3\%$, $k = 1.2$, and the experimental data of Hatcher et al. (2015)

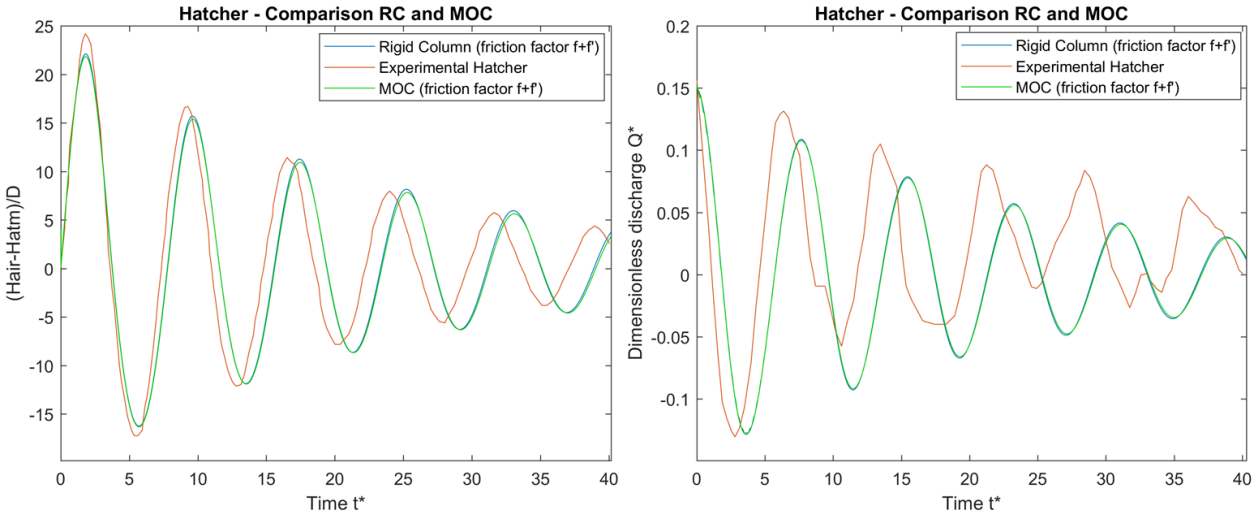

Figure 5.13 The dimensionless air pocket (left) and dimensionless discharge (right) against time with additional friction factor for $V_a^{*0} = 2.63$, $Q^{*0} = 0.15$, $D = 0.053\ m$, $L = 10.7\ m$, $S_0 = 2\%$, $k = 1.2$, and the experimental data of Hatcher et al. (2015)

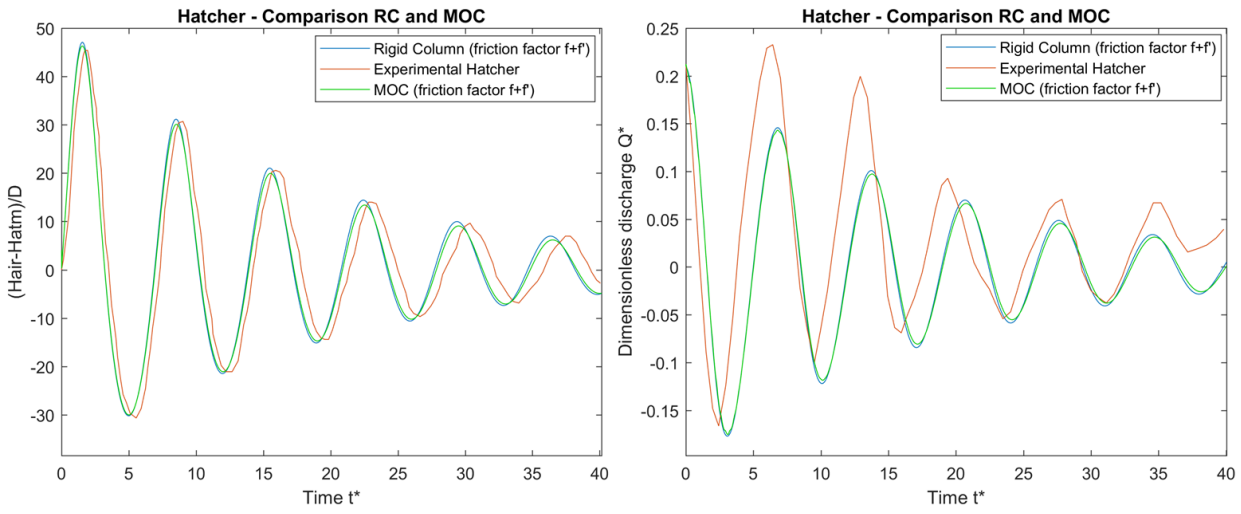

Figure 5.14 The dimensionless air pocket (left) and dimensionless discharge (right) against time with additional friction factor for $V_a^{*0} = 1.29$, $Q^{*0} = 0.21$, $D = 0.053\ m$, $L = 10.7\ m$, $S_0 = 2\%$, $k = 1.2$, and the experimental data of Hatcher et al. (2015)

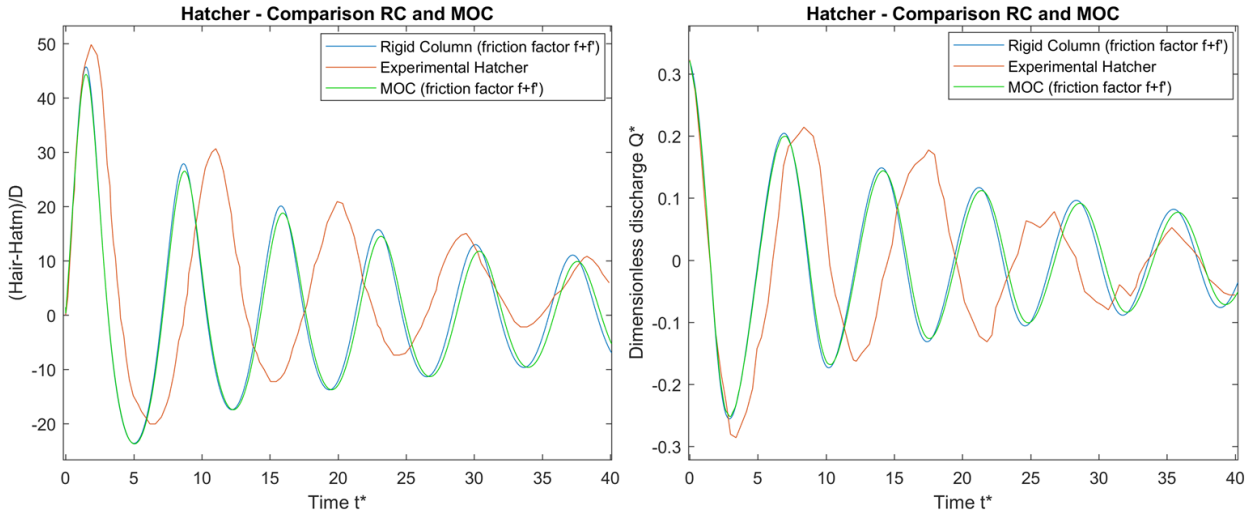

Figure 5.15 The dimensionless air pocket (left) and dimensionless discharge (right) against time with additional friction factor for $V_a^{*0} = 1.10$, $Q^{*0} = 0.32$, $D = 0.102\ m$, $L = 12\ m$, $S_0 = 1.3\%$, $k = 1.2$, and the experimental data of Hatcher et al. (2015)

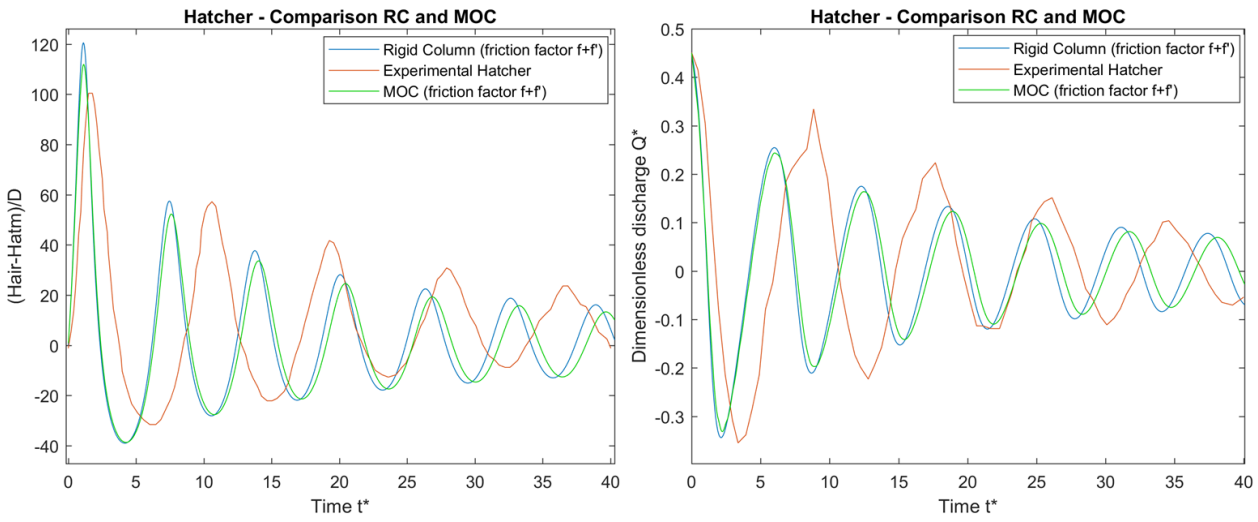

Figure 5.16 The dimensionless air pocket (left) and dimensionless discharge (right) against time with additional friction factor for $V_a^{*0} = 0.51$, $Q^{*0} = 0.45$, $D = 0.102\ m$, $L = 12\ m$, $S_0 = 1.3\%$, $k = 1.2$, and the experimental data of Hatcher et al. (2015)

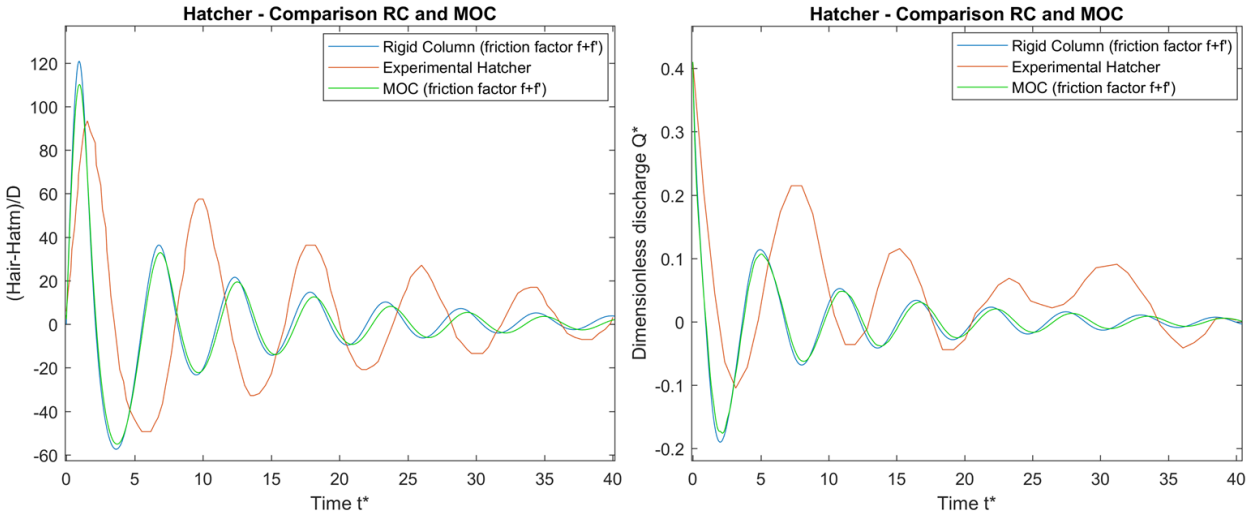

Figure 5.17 The dimensionless air pocket (left) and dimensionless discharge (right) against time with additional friction factor for $V_a^{*0} = 0.32$, $Q^{*0} = 0.41$, $D = 0.053\ m$, $L = 10.7\ m$, $S_0 = 2\%$, $k = 1.2$, and the experimental data of Hatcher et al. (2015)

Adding the additional friction factor allows to increase the attenuation of the pressure and discharge compared to the steady-state friction factor. The additional friction factor helps to improve the accuracy of the pressure graphs for large air pockets ($V_a^{*0} \geq 1.29$) as shown in Figure 5.12, Figure 5.13, Figure 5.14 and the phase shift is little. However, for small air pockets ($V_a^{*0} \leq 1.10$), the phase shift becomes very noticeable as shown in Figure 5.15, Figure 5.16 and Figure 5.17 and the numerical pressure peaks can also be very different from the experimental ones, particularly in the case of $V_a^{*0} = 0.32$ shown in Figure 5.17. The reason for the poor behavior in cases with small air pocket volumes for the rigid column and the method of characteristics is supposed to be due to the phase shift which is influenced by the value of k. Using a polytropic coefficient $k = 1.2$ for small air pockets for both models leads to a phase shift between experimental and numerical results regardless if the friction factor used is the steady-state friction factor (Figure 5.9, Figure 5.10, and Figure 5.11 or Hatcher et al. (2015)) or the additional friction factor (Figure 5.15, Figure 5.16 and Figure 5.17).

It can be observed that with the additional friction factor, the numerical results (pressure and discharge) obtained with the rigid column model are very close to the ones obtained with the method of characteristics for every initial air pocket volume $V_a^{*0} \in \{0.94; 1.05; 1.11; 1.68; 1.83\}$. This is not the case with only the steady-state friction factor because the pressure and the discharge peaks simulated by the rigid column approach are greater in absolute value than the corresponding peaks of the method of characteristics, as shown in Figure 5.10 and Figure 5.11.

5.3.3 Additional friction factor and polytropic coefficient k=1.2

As seen in Chapter 4, the polytropic coefficient k influences the phase of the numerical pressure graph. In order to obtain a similar phase between the numerical and experimental pressure peaks, the polytropic coefficient k was changed by trial and error. The results are given in Figure 5.18, Figure 5.19, Figure 5.20, Figure 5.21, Figure 5.22, and Figure 5.23.

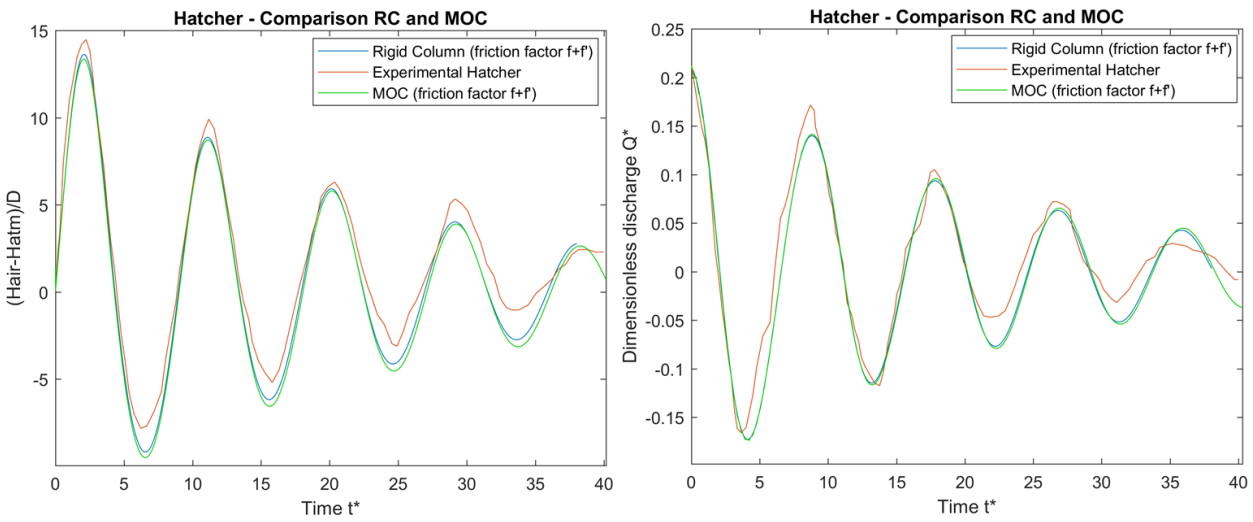

Figure 5.18 The dimensionless air pocket (left) and dimensionless discharge (right) against time with additional friction factor for $V_a^{*0} = 3.70$, $Q^{*0} = 0.21$, $D = 0.102\ m$, $L = 12\ m$, $S_0 = 1.3\%$, $k = 1.1$, and the experimental data of Hatcher et al. (2015)

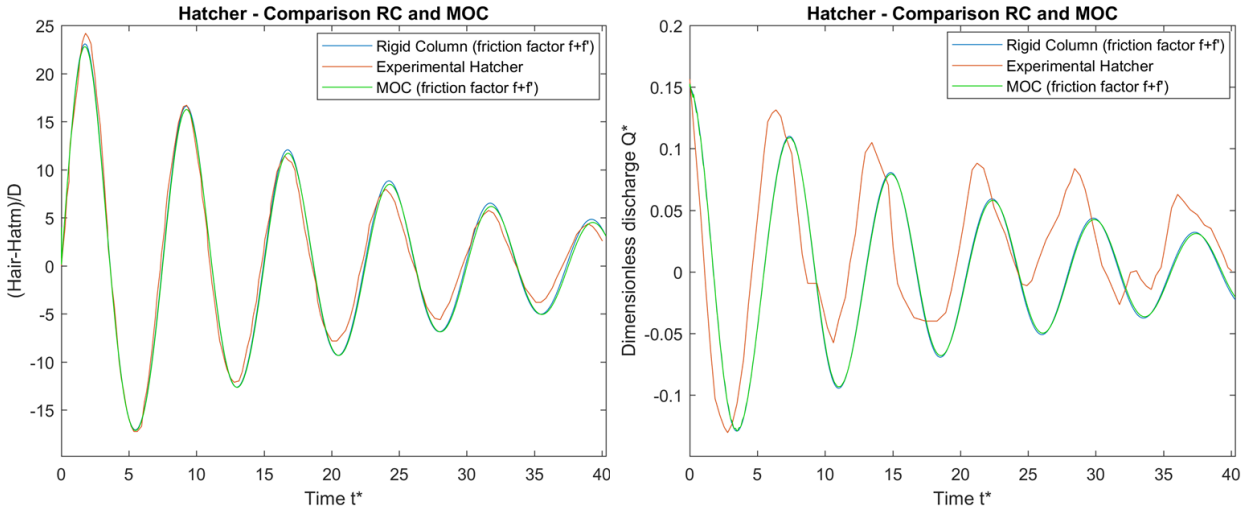

Figure 5.19 The dimensionless air pocket (left) and dimensionless discharge (right) against time with additional friction factor for $V_a^{*0} = 2.63$, $Q^{*0} = 0.15$, $D = 0.053\ m$, $L = 10.7\ m$, $S_0 = 2\%$, $k = 1.3$, and the experimental data of Hatcher et al. (2015)

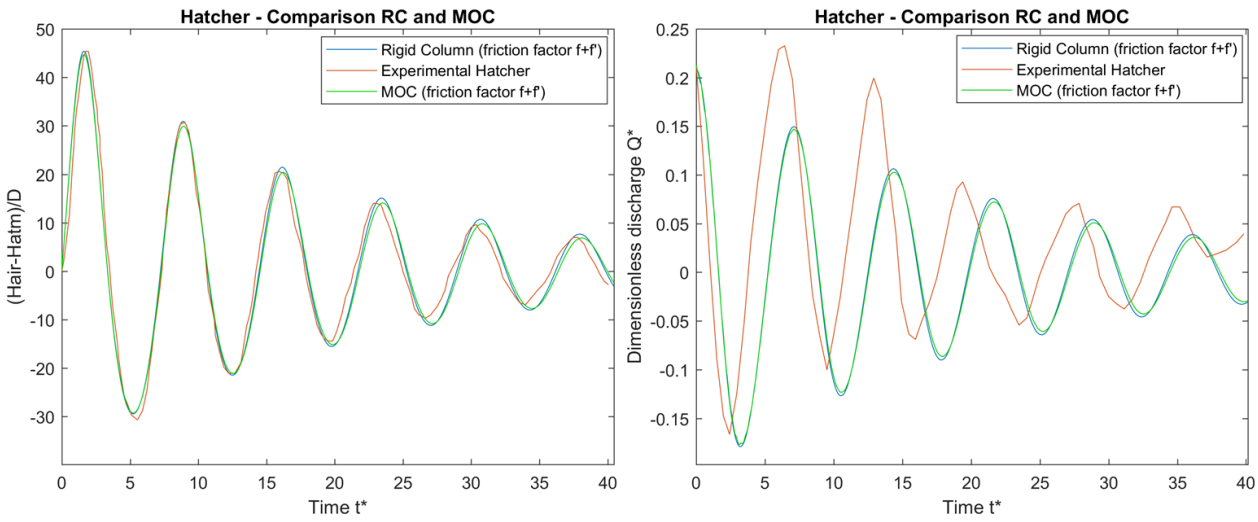

Figure 5.20 The dimensionless air pocket (left) and dimensionless discharge (right) against time with additional friction factor for $V_a^{*0} = 1.29$, $Q^{*0} = 0.21$, $D = 0.053\ m$, $L = 10.7\ m$, $S_0 = 2\%$, $k = 1.1$, and the experimental data of Hatcher et al. (2015)

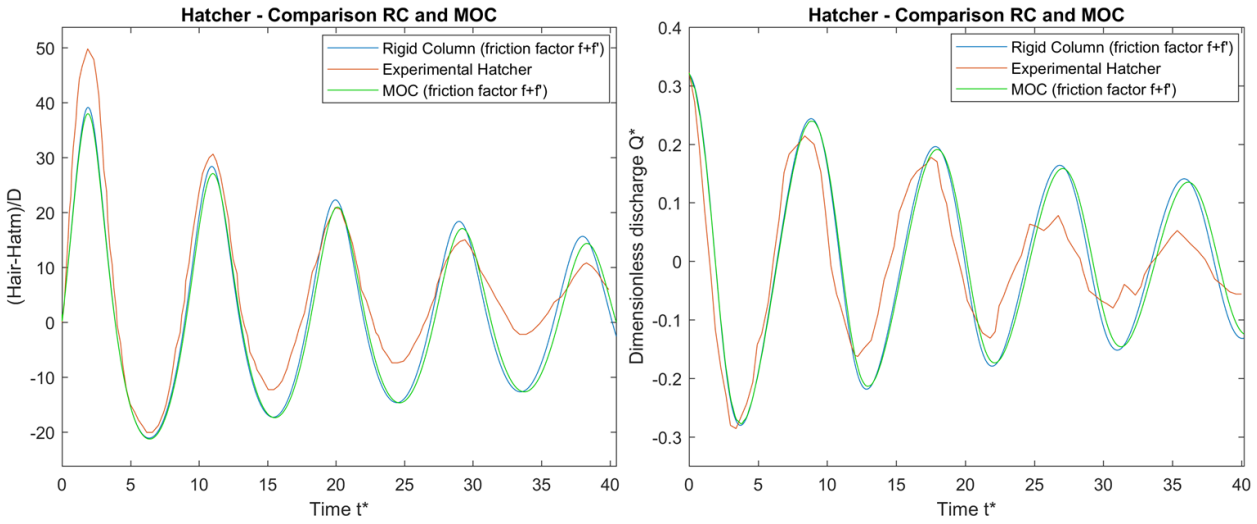

Figure 5.21 The dimensionless air pocket (left) and dimensionless discharge (right) against time with additional friction factor for $V_a^{*0} = 1.10$, $Q^{*0} = 0.32$, $D = 0.102\ m$, $L = 12\ m$, $S_0 = 1.3\%$, $k = 0.75$, and the experimental data of Hatcher et al. (2015)

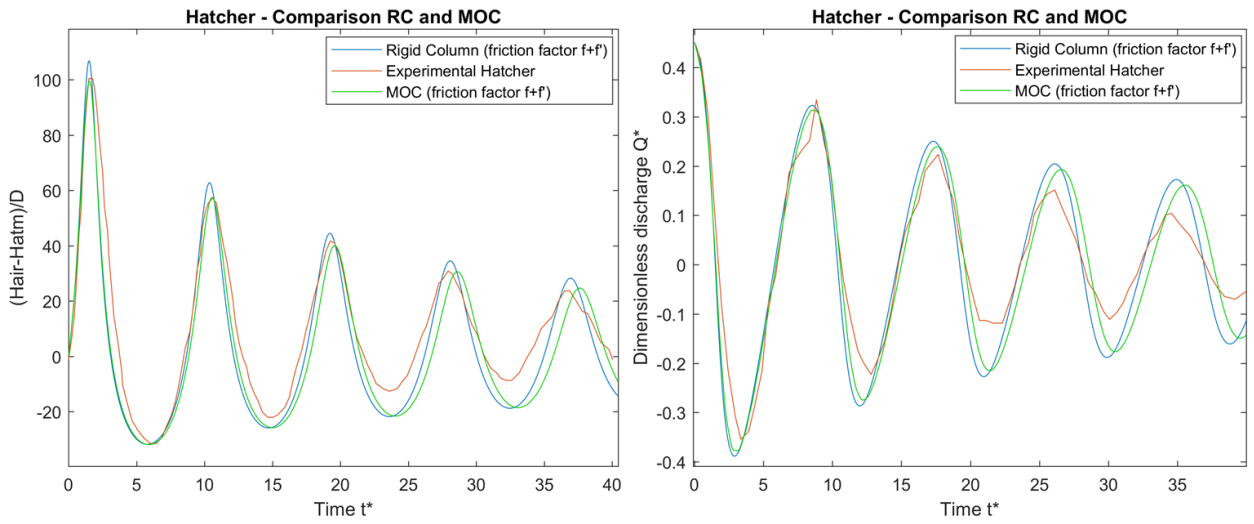

Figure 5.22 The dimensionless air pocket (left) and dimensionless discharge (right) against time with additional friction factor for $V_a^{*0} = 0.51$, $Q^{*0} = 0.45$, $D = 0.102\ m$, $L = 12\ m$, $S_0 = 1.3\%$, $k = 0.6$, and the experimental data of Hatcher et al. (2015)

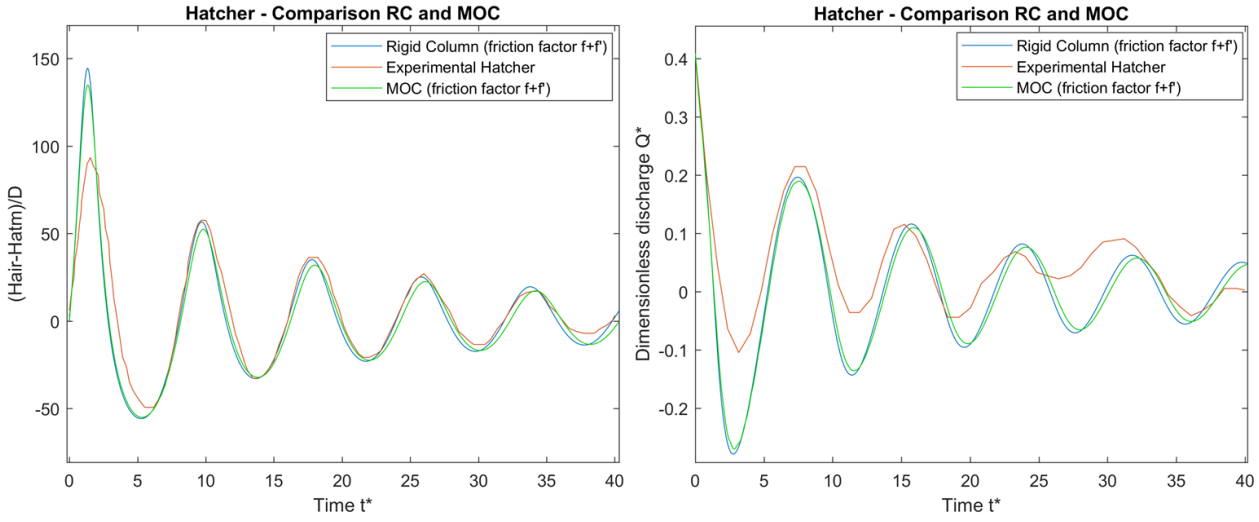

Figure 5.23 The dimensionless air pocket (left) and dimensionless discharge (right) against time with additional friction factor for $V_a^{*0} = 0.32$, $Q^{*0} = 0.41$, $D = 0.053\ m$, $L = 10.7\ m$, $S_0 = 2\%$, $k = 0.57$, and the experimental data of Hatcher et al. (2015)

The results given by adapting the value of k show that the pressure attenuation and the pressure phase are better captured. The discharge Q^* approximation is also improved by adapting the value of k. From the literature, the value of the polytropic coefficient k may influence the concordance between the numerical and experimental results (Bousso et al., 2013a and 2013b). The value of k is generally chosen by authors in order to have the best concordance between numerical and experimental results. For a given diameter D, when the initial discharge ${Q^*}^0$ increases, the initial volume of the air pocket ${V_a^*}^0$ decreases. Depending on the volume of the air pocket, the heat transfer may vary and therefore the polytropic coefficient k may vary too. Martin (1976), Lee and Martin (1999), Zhou et al. (2002), León et al. (2008) and Chaudhry and Reddy (2011) used numerical models with a polytropic coefficient ranging from 1 to 1.4.

However, Lee (2005) indicated that since the transient flow in SWSs is a fast process so that the adiabatic assumption ($k = 1.4$) is more relevant. In addition, Wan et al. (2010) studied transient flows in a rapidly filling horizontal pipe containing trapped air and simulated the problem with a numerical model based on the rigid column model. By comparing different values of k (1.0001; 1.2 and 1.4), they observed that the polytropic coefficient $k = 1.4$ gave the closest numerical results to the experimental values. This value of $k = 1.4$ was also the one chosen for the numerical simulation of Chapter 4 to compare with the results of the experiments carried out in the Hydraulics laboratory of "École Polytechnique de Montréal". It corresponds to an adiabatic process without heat transfer. However, Bousso and Fuamba (2013b) mentioned that ideal adiabatic ($k = 1.4$) or isothermal ($k = 1$) conditions are rarely verified in experiments. Assuming an identical k value for each size of air pocket may be questionable.

In addition, the phase shift does not seem to be exclusive to the rigid column and the method of characteristics. Vasconcelos et al. (2011) observed that for smaller air pockets the rigid column model and the Two-component approach (TPA) were less accurate and were unable to properly replicate the oscillation period. Thus, a phase shift was also observed for certain size of air pocket with TPA.

By quoting Bousso et al. (2013):

> "It seems obvious that further investigation is needed to enable a better choice of coefficient k that considers the air ratio, the air cavity size, the type of equations, and the test conditions".

This statement is reinforced by the results obtained in Chapters 4 and 5.

5.4 Conclusion

It was shown that using the calibrated additional friction factor in the rigid column model and the method of characteristics could lead to more accurate results with a better energy dissipation. It was also observed that for some test cases of Hatcher et al. (2015), there was a great discrepancy between numerical and experimental results. The phase shift was corrected by adapting the value of k by trial and error, but unfortunately this technique is not predictive.

CHAPTER 6 A SHOCK FITTING APPROACH APPLIED TO AIR POCKET ENTRAPMENT IN TRANSIENT FLOW

6.1 Introduction

In this chapter, similar to the previous chapters, a pipe segment is linked to a reservoir at upstream end and the air pocket is located at the downstream. The upstream flow is pressurized whereas the downstream flow is free-surface. The downstream end is suddenly closed with a valve and the air pocket is entrapped. However, in Chapters 4 and 5, the rigid column and the method of characteristics models were used by considering only the pressurized zone and the air pocket. The purpose of this chapter is to propose a model, which integrates this free-surface flow component in order to more accurately simulate the air pocket entrapment than the two previous models that neglect the free-surface flow. This new model proposed in this chapter considers the effect of the pressurized zone, the free-surface zone, and the air pocket. It uses the method of characteristics in a shock-fitting approach with a movable interface separating the pressurized flow and the free-surface flow.

Some shock-fitting approaches were already suggested to simulate the air pocket problem such as the ones of Rokhzadi and Fuamba (2019, 2020b). These shock-fitting approaches use the rigid column model for the pressurized zone and the method of characteristics to solve the set of Saint-Venant equations in the free-surface zone. In this present shock-fitting approach, the method of characteristics will be applied in both pressurized and free-surface regions. This new shock-fitting approach is part of the family of the interface tracking models (Bousso et al. 2013).

The code written in MATLAB for the shock-fitting approach developed in this chapter can be found in Appendix C.

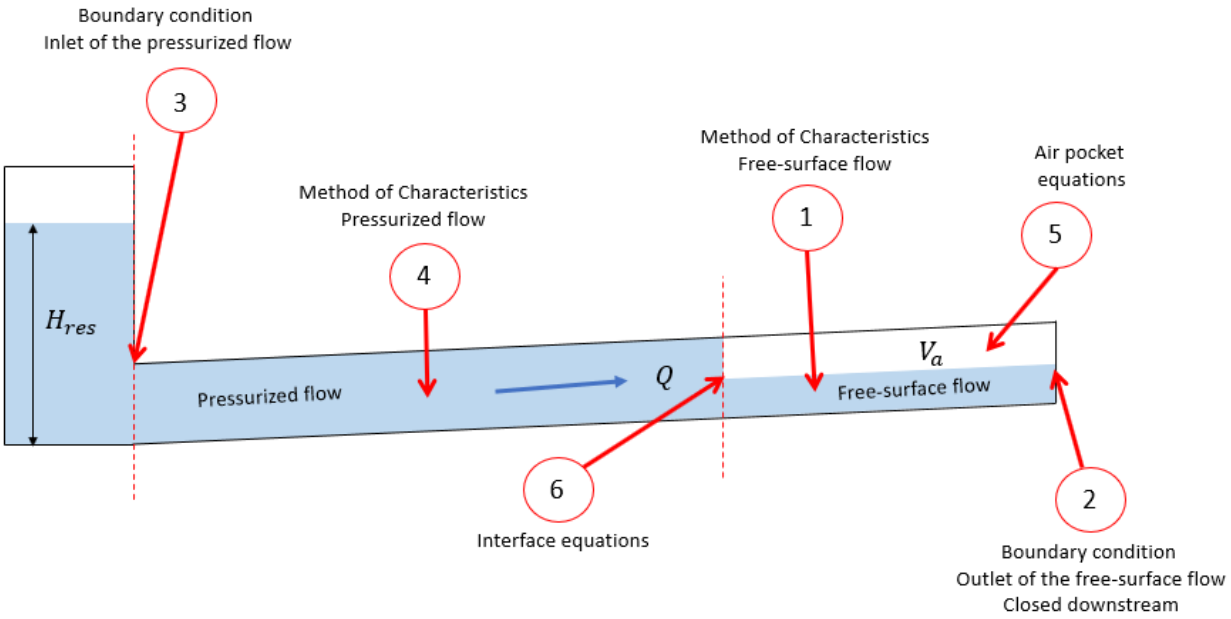

Figure 6.1 The steps in applying the shock-fitting approach

As shown in Figure 6.1, the shock-fitting approach is applied as $1 \rightarrow 2 \rightarrow 3 \rightarrow 4 \rightarrow 5 \rightarrow 6$ but can also be $3 \rightarrow 4 \rightarrow 1 \rightarrow 2 \rightarrow 5 \rightarrow 6$ without changing the results.

6.2 Shock-fitting approach

The time step $\Delta t'$ of the pressurized zone is calculated with the Courant-Friedrichs-Lewy (CFL) condition (Rokhzadi and Fuamba, 2020b):

$$\Delta t' = CFL \frac{\Delta x}{|a| + max\ (|V_u|)} \tag{6-1}$$

where $max\ (|V_u|)$ represents the maximum of the absolute values of the velocity in the pressurized zone. The Courant number is set equal to $CFL = 0.9$.

The time step $\Delta t''$ of the free-surface zone is calculated with:

$$\Delta t'' = CFL \frac{\Delta x}{|c| + max\ (|V|)} \tag{6-2}$$

where $max\ (|V|)$ represents the maximum of the absolute values of the velocity in the free-surface zone. The time step Δt is set to the minimum of $\Delta t'$ and $\Delta t''$:

$$\Delta t = \min(\Delta t', \Delta t''). \tag{6-3}$$

To initialise the pressure values of the free-surface flow for the shock-fitting model, the steady state solution for the free-surface flow need to be known. The water depth in the free-surface region was studied by several authors. Montes (1997) studied the transition to a free-surface flow at the end of a circular horizontal conduit. He determined the cavity profile at the end of the pipe with the x-ψ method. The cavity profile found numerically was similar to the one found experimentally. The water depth of the free-surface flow at the end of the pipe is between $0.5D$ and $0.6D$ with D the diameter of the pipe. According to Benjamin (1968) and Alves et al. (1993), by neglecting surface tension, the free-surface depth in steady conditions is equal to $0.563D$ for a horizontal pipe. For the experimental data of Hatcher et al. (2015), the slope is low so the free-surface depth in steady conditions is assumed to be around $0.563D$.

The initial length of the pressurized zone L_u^0 is calculated with equation (6-4):

$$L_u^0 = \frac{L_{pipe}(A - A_t) - V_a^0}{(A - A_t)}, \tag{6-4}$$

where A_t is the cross-sectional area of the channel, A is the cross-sectional area of the pipe, L_{pipe} is the length of the pipe and V_a^0 is the initial volume of air.

6.2.1 Method of Characteristics – Free-surface flow equations

The downstream free-surface flow is governed by the Saint-Venant equations, referred as the continuity equation (6-5) and the momentum equation (6-6) (Chaudhry, 2007; 2014) :

$$\frac{\partial y}{\partial t} + V\frac{\partial y}{\partial x} + \frac{A}{B}\frac{\partial V}{\partial x} = 0, \tag{6-5}$$

$$g\frac{\partial y}{\partial x} + \frac{\partial V}{\partial t} + V\frac{\partial V}{\partial x} = g\left(S_0 - S_f\right), \tag{6-6}$$

where V is the velocity, y is the flow depth, A is the flow area, B is the top water surface width, S_0 is the channel bottom slope, S_f is the slope of the energy grade line, x is the distance along the channel length, t is the time and g is the gravitational acceleration.

From (Chaudhry 2007), the positive and negative characteristic lines correspond to the equations (6-7) and (6-8):

$$\frac{dx}{dt} = V + c, \tag{6-7}$$

$$\frac{dx}{dt} = V - c. \tag{6-8}$$

By using the same notations as the Figure 5.4, the free-surface depth y and velocity v at the points R (y_R, v_R) and S (y_S, v_S) are obtained by linear interpolations:

$$\begin{cases} y_R = y_M + CFL(y_A - y_M) \\ v_R = v_M + CFL(v_A - v_M) \end{cases}, \tag{6-9}$$

$$\begin{cases} y_S = y_P + CFL(y_B - y_P) \\ v_S = v_P + CFL(v_B - v_P) \end{cases}. \tag{6-10}$$

The two compatibility equations are written as the equations (6-11) and (6-12) :

$$C^+: \; y_P = y_R - c_R \times \left(\frac{v_P - v_R}{g}\right) - c_R\left(S_f - S_0\right)_R \times \Delta t, \tag{6-11}$$

$$C^-: \; y_P = y_S + c_S \times \left(\frac{v_P - v_S}{g}\right) + c_S\left(S_f - S_0\right)_S \times \Delta t. \tag{6-12}$$

The system of equations constituted by the equations (6-11) and (6-12) yields to the following equations (6-13), (6-14), (6-15), and (6-16) which allow to calculate the pressure and the discharge at the point P (y_P, v_p):

$$D_q = v_R + \left(\frac{g}{c_R}\right) y_R + g\left(S_0 - S_f\right)_R \times \Delta t, \tag{6-13}$$

$$D_n = v_S - \left(\frac{g}{c_S}\right) y_S + g\left(S_0 - S_f\right)_S \times \Delta t, \tag{6-14}$$

$$y_P = (D_q - D_n)/(\frac{g}{c_R} + \frac{g}{c_S}), \tag{6-15}$$

$$v_P = D_n + \frac{g}{c_S} y_P. \tag{6-16}$$

The slope of the energy grade S_f is obtained by using the Manning equation (6-17):

$$S_f = \frac{n^2 \times v^2}{(R_h)^{4/3}}, \tag{6-17}$$

where n is the Manning coefficient assumed equal to $n = 0.009$ (Rokhzadi and Fuamba 2019), v the flow velocity in the free-surface zone and R_h the hydraulic radius.

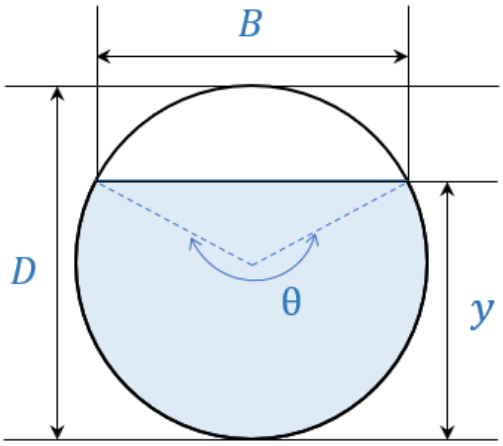

Figure 6.2 Definition of variables in the free-surface region

From Figure 6.2, the angle θ is equal to:

$$\theta = 2 \times \text{acos}\left(\frac{\frac{D}{2} - y}{\frac{D}{2}}\right). \tag{6-18}$$

The cross-sectional area A_t of the channel is equal to:

$$A_t = \left(\frac{D^2}{8}\right) \times (\theta - \sin(\theta)). \tag{6-19}$$

The celerity of the gravity wave c is obtained with the following equation (6-20) (León, 2007):

$$c = \sqrt{\frac{gA}{B}} = \sqrt{g\frac{D}{8}}\sqrt{\frac{\theta - \sin(\theta)}{\sin(\frac{\theta}{2})}}. \quad (6\text{-}20)$$

When calculating the gravity wave speed of R and S, the gravity wave speed c can either be calculated with the equation (6-20) applied to R and S, or be calculated with the interpolation equations (6-21) and (6-22) :

$$c_R = c_M + CFL(c_A - c_M), \quad (6\text{-}21)$$

$$c_S = c_P + CFL(c_B - c_P). \quad (6\text{-}22)$$

6.2.2 Boundary condition; Outlet of the free-surface flow (closed downstream)

The downstream end is closed so the velocity of the last node of the free-surface zone is $v_n = 0$.

The positive characteristic C^+ equation (6-11) is used to find the depth y_n of the last node of the free-surface zone:

$$y_n = y_R - c_R \times \left(\frac{v_n - v_R}{g}\right) - c_R\left(S_f - S_0\right)_R \times \Delta t. \quad (6\text{-}23)$$

6.2.3 Boundary condition; Inlet of the pressurized zone (near the reservoir)

The energy equation (6-24) is used between the reservoir and the first node of the pressurized zone to determine the pressure of the first node of the pressurized zone H_0:

$$H_0 = H_{res} - (1 + K_{loss}) \times \frac{v_0^2}{2g}. \quad (6\text{-}24)$$

The negative characteristic C^- equation (6-25) is used to find the velocity of the first node of the pressurized zone v_0:

$$v_0 = v_S - \left(\frac{g}{a}\right)H_S + g\left(S_0 - S_f\right)_S \times \Delta t + \frac{g}{a}H_0. \quad (6\text{-}25)$$

6.2.4 Method of characteristics; Pressurized flow

The upstream pressurized flow is governed by the water hammer equations, referred as the continuity equation (6-26) and the momentum equation (6-27) (Chaudhry, 2014; Wylie and Streeter, 1993):

$$\frac{\partial H}{\partial t} + V\frac{\partial H}{\partial x} + \frac{a^2}{g}\frac{\partial V}{\partial x} = 0, \tag{6-26}$$

$$g\frac{\partial H}{\partial x} + \frac{\partial V}{\partial t} + V\frac{\partial V}{\partial x} = g(S_0 - S_f), \tag{6-27}$$

where V is the velocity, H is the piezometric head, a is the water hammer wave velocity, S_0 is the channel bottom slope, S_f is the slope of the energy grade line, x is the distance along the channel length, t is the time and g is the gravitational acceleration.

From Wylie and Streeter (1993), the positive and negative characteristic lines correspond to the equations (6-28) and (6-29):

$$\frac{dx}{dt} = V + a, \tag{6-28}$$

$$\frac{dx}{dt} = V - a. \tag{6-29}$$

By using the same notations as Figure 5.4, the piezometric head H and velocity v at the points R (H_R, v_R) and S (H_S, v_S) are obtained by linear interpolations:

$$\begin{cases} H_R = H_M + CFL(H_A - H_M) \\ v_R = v_M + CFL(v_A - v_M) \end{cases}, \tag{6-30}$$

$$\begin{cases} H_S = H_P + CFL(H_B - H_P) \\ v_S = v_P + CFL(v_B - v_P) \end{cases}. \tag{6-31}$$

The two compatibility equations are written as the equations (6-32) and (6-33):

$$C^+: \; H_P = H_R - a \times \left(\frac{v_P - v_R}{g}\right) - a\left(S_f - S_0\right)_R \times \Delta t, \tag{6-32}$$

$$C^{-}:\ H_P = H_S + a \times \left(\frac{v_P - v_S}{g}\right) + a\left(S_f - S_0\right)_S \times \Delta t. \tag{6-33}$$

The system of equations constituted by the equations (6-32) and (6-33) yields to the following equations (6-13), (6-14), (6-15), and (6-16) which allow to calculate the pressure and the discharge at the point P (H_P, v_p):

$$D_q = v_R + \left(\frac{g}{a}\right) y_R + g\left(S_0 - S_f\right)_R \times \Delta t, \tag{6-34}$$

$$D_n = v_S - \left(\frac{g}{a}\right) y_S + g\left(S_0 - S_f\right)_S \times \Delta t, \tag{6-35}$$

$$H_P = \frac{D_q - D_n}{\frac{2g}{a}}, \tag{6-36}$$

$$v_P = D_n + \frac{g}{a} H_P. \tag{6-37}$$

6.2.5 Air pocket equations

The air pocket is modelled with the ideal gas law and the polytropic process represented by equation (6-38):

$$\frac{dH_{air}}{dT} = k \frac{H_{air}}{V_a} \frac{dV_a}{dT}. \tag{6-38}$$

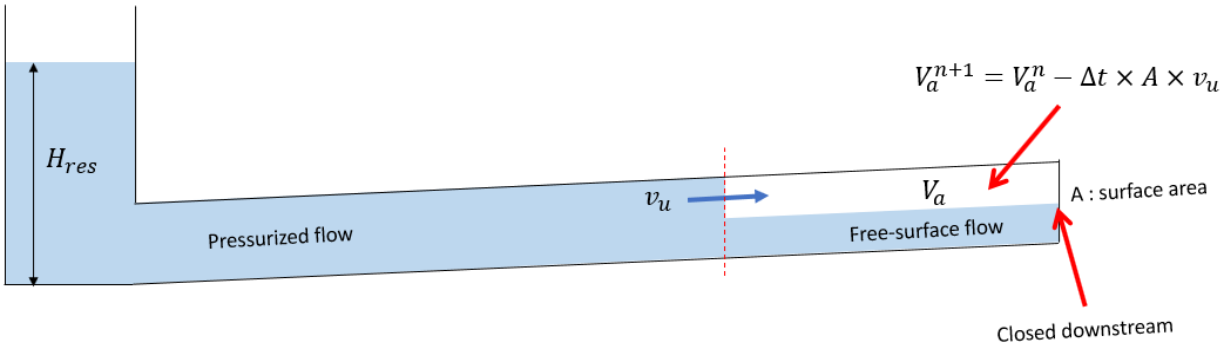

Figure 6.3 Calculation of the air pocket volume

As seen in Figure 6.3, the new air pocket volume V_a^{n+1} at time $n+1$ is calculated with the value V_a^n at the previous time step:

$$V_a^{n+1} = V_a^n - \Delta t \times A \times v_u, \tag{6-39}$$

where v_u represents the velocity of the last node of the pressurized zone.

Equation (6-38) can be expressed as equation (6-40) to calculate the air pressure H_{air}^{n+1} at time $n+1$ with the value H_{air}^n at the previous time step :

$$H_{air}^{n+1} = H_{air}^n \times (\frac{V_a^n}{V_a^{n+1}})^k. \tag{6-40}$$

6.2.6 Interface equations

The shock-fitting approach used in this chapter assumes a unique surge front. To introduce the interface equations, some notions need to be introduced. The theory is based on the concepts of positive and negative interfaces as shown in Figure 6.4 in stationary coordinate system. The positive interface, also called advancing interface, is defined as an interface moving in direction of the open-channel flow, causing the pipe to pressurize or fill up. The negative interface, also called retreating interface, is defined as an interface moving in direction of the region of the pressurized flow which means that the pipe depressurizes.

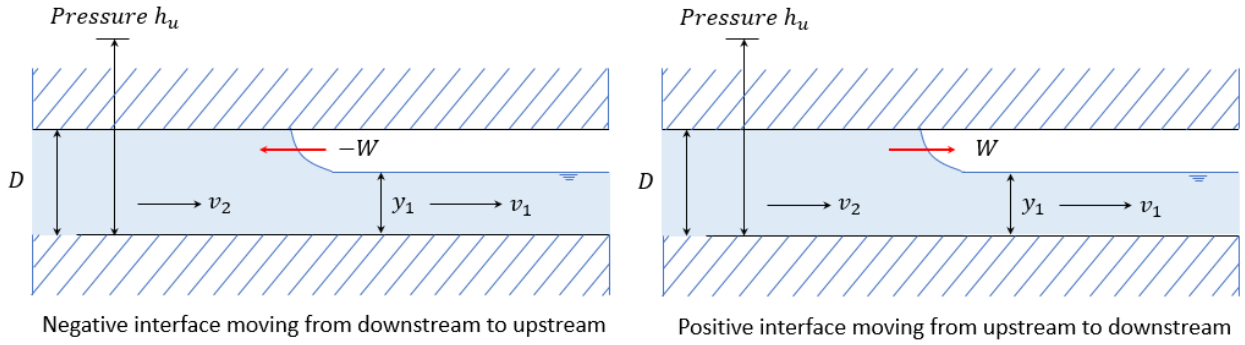

Figure 6.4 Negative interface moving from dowstream to upstream (left illustration) and positive interface moving from upstream to downstream (right illustration) in stationary coordinate system (inspired by Cardle, 1984; Song et al., 1983; Fuamba, 2002)

In order to express the equations of the positive and negative interfaces, the stationary coordinate system of Figure 6.4 need to be expressed in a moving coordinate as shown in Figure 6.5.

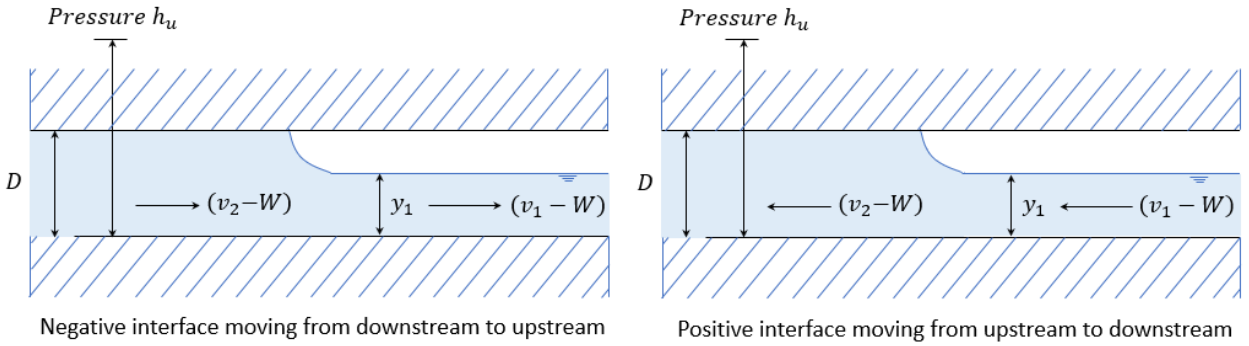

Figure 6.5 Negative interface moving from dowstream to upstream (left illustration) and positive interface moving from upstream to downstream (right illustration) in stationary coordinates in a moving coordinate system (inspired by Cardle, 1984; Song et al., 1983; Fuamba, 2002)

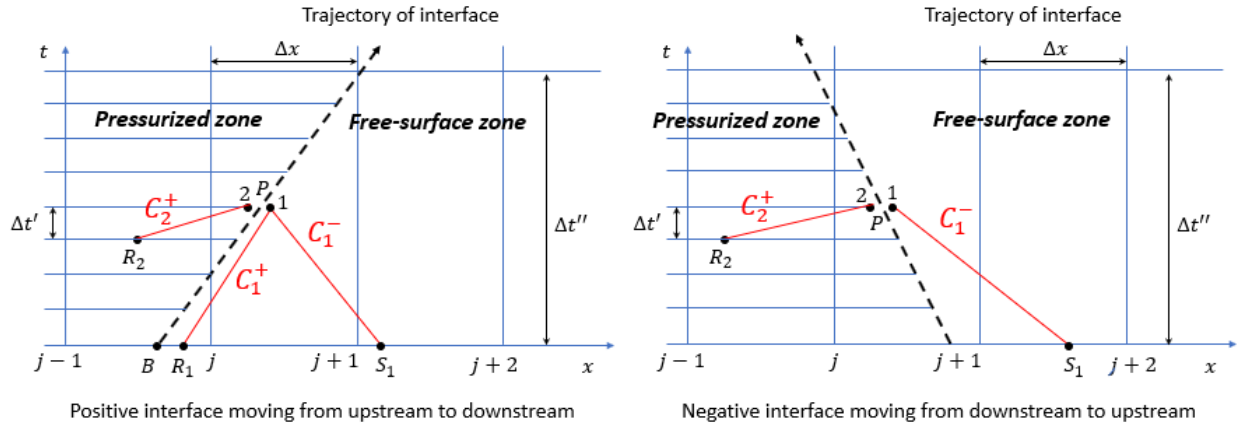

Figure 6.6 Typical x-t grid system near a negative interface (left illustration) and near a positive interface (right illustration)

For the positive interface moving from upstream to downstream, the fluid in moving coordinate system moves from right to left across, from the supercritical to the subcritical condition (Cardle, 1984). By denoting Fr_1 as the Froude number in the pressurized zone and Fr_2 as the Froude number in the free-surface zone, it yields to:

$$Fr_1 < 1 < Fr_2 \quad \Leftrightarrow \quad \frac{(Flow\ velocity)_1}{(Wave\ speed)_1} < 1 < \frac{(Flow\ velocity)_2}{(Wave\ speed)_2} \tag{6-41}$$

Therefore the following condition holds:

$$a + v_2 > W > c + v_1. \tag{6-42}$$

The position of the interface is determined by the relation $\frac{dL}{dt} = W$, in which W represents the slope of the interface trajectory of the interface in the x-t plane shown in Figure 6.6. Because the slope of the positive C_2^+ characteristic of the pressurized region is $\frac{dx}{dt} = (a + v_2)$ and that of the positive C_1^+ characteristic of the open-channel flow is $\frac{dx}{dt} = (c + v_1)$, the inequality (6-42) guarantees that the characteristic equations C_2^+, C_1^+, and C_1^- are applicable for the positive interface moving from upstream to downstream.

A similar reasoning is done for the negative interface moving from the downstream to upstream to obtain that the characteristic equations C_2^+ and C_1^- are applicable in the case of negative interface moving (Cardle 1984).

Positive interface moving downstream:

Inspired by Cardle (1984), the equations for the positive interface advancing downstream are the following equations (6-43), (6-44), (6-45), (6-46), and (6-47):

$$C_1^+ : y_{P1} - y_{R1} + \frac{c_{R1}(v_{P1} - v_{R1})}{g} + c_{R1}(S_f - S_0)\Delta t = 0, \tag{6-43}$$

$$C_1^- : y_{P1} - y_{S1} - \frac{c_{S1}(v_{P1} - v_{S1})}{g} + c_{S1}(S_f - S_0)\Delta t = 0, \tag{6-44}$$

$$C_2^+ : y_{P2} - y_{R2} - \frac{c_{S1}(v_{P1} - v_{S1})}{g} + a(S_f - S_0)\Delta t = 0, \tag{6-45}$$

$$Continuity : (v_{P1} - W)A_1 = (v_{P2} - W)A_2, \tag{6-46}$$

$$Momentum : \rho g(y_{P2} - 0.5D)A_2 - \bar{F} - \rho g A H_{air} = \rho A_2(v_{P1} - W)(v_{P1} - v_{P2}). \tag{6-47}$$

The average pressure of the water column over the cross-sectional area $\bar{p}$ and the corresponding force $\bar{F}$ are calculated with the following equation (6-48) (León, 2007):

$$\bar{F} = \bar{p}A_1 = \frac{\rho g}{12}\left[(3D^2 - 4Dy + 4y^2)\sqrt{y(D-y)} - 3D^2(D-2y)\arctan\left(\frac{\sqrt{y}}{\sqrt{d-y}}\right)\right]. \quad (6\text{-}48)$$

Note that $\bar{F}$ is equal to $\rho g\overline{y_1}A_1$, in which $\overline{y_1}$ is the distance from the water surface to the gravity center of cross-sectional area in the free-surface zone. The initial idea behind equation (6-48) instead of $\bar{F} = \rho g\overline{y_1}A_1$ is because assuming $\bar{F} = \rho g\overline{y_1}A_1$ means that the pressure is hydrostatic, which could be a questionable assumption since the flow is transient. However, it was observed that using $\bar{F} = \rho g\overline{y_1}A_1$ or formula (6-48) did not make much difference in the results. Thus, both formulas can be used.

Only three equations are required to solve the system of equations for the positive interface moving downstream (León et al., 2010). The only three equations to solve are the equations (6-45), (6-46), and (6-47). The equations (6-43) and (6-44) are not necessary.

Negative interface moving upstream:

Inspired by Cardle (1984), the equations for the negative interface moving upstream are the following equations (6-50), (6-51), (6-52), (6-53), (6-54), (6-55), and (6-56):

$$C_2^+ : y_{P2} - y_{R2} + \frac{a(v_{P2} - v_{S2})}{g} + a(S_f - S_0)\Delta t = 0, \quad (6\text{-}49)$$

$$C_1^- : y_{P1} - y_{S1} - \frac{c_{S1}(v_{P1} - v_{S1})}{g} - c_{S1}(S_f - S_0)\Delta t = 0, \quad (6\text{-}50)$$

$$Continuity : (v_{P1} - W)A_1 = (v_{P2} - W)A_2, \quad (6\text{-}51)$$

$$Momentum : \rho g(y_{P2} - 0.5D)A_2 - \bar{F} - \rho g A H_{air} = \rho A_2(v_{P2} - W)(v_{P1} - v_{P2}), \quad (6\text{-}52)$$

$$c_{S1} = \sqrt{g\frac{D}{8}}\sqrt{\frac{\theta - \sin(\theta)}{\sin(\frac{\theta}{2})}}, \quad (6\text{-}53)$$

$$y_{P1} = \left(\frac{D}{2}\right) \times \left(1 - \cos\left(\frac{\theta}{2}\right)\right), \quad (6\text{-}54)$$

$$\bar{F} = \frac{\rho g}{12}\left[(3D^2 - 4Dy + 4y^2)\sqrt{y(D-y)} - 3D^2(D-2y)\arctan\left(\frac{\sqrt{y}}{\sqrt{d-y}}\right)\right], \quad (6\text{-}55)$$

$$A_1 = \left(\frac{D^2}{8}\right) \times (\theta - \sin(\theta)). \quad (6\text{-}56)$$

6.3 Results

It is worth mentioning that if, for iterative approaches, the Newton-Raphson algorithm is used, the code can become unstable when there are large discontinuities because this algorithm can diverge. The instability is a common aspect with shock-fitting approaches using MOC where there is a major discontinuity (Bousso, 2010; Chaudhry, 2007). The Newton–Raphson method for nonlinear systems of equations can also diverge in other approaches for storm-water systems (León et al., 2010).

To solve this instability issue, the idea was to solve the system of non-linear equations by using a combination of the Newton-Raphson algorithm and the Levenberg-Marquardt algorithm. The latter takes longer to converge but is more stable than the Newton-Raphson algorithm. Thus, the decision was made to always use the Newton-Raphson algorithm for each time step except when it is about to diverge and in this case the Levenberg-Marquardt algorithm is used.

Another source of instability is the way the position of the interface is calculated. A common way to determine the interface is assuming that a grid point in the free-surface becomes pressurized if its depth y is superior to $0.95D$ and that a grid point in the pressurized zone becomes free-surface if its pressure head H is inferior to $0.84D$ and the air pocket relative pressure is positive. The reference value of $y_{ref,1} = 0.95D$ which represents the phase change from free-surface to pressurized flow comes from León et al. (2010). The threshold value of $y_{ref,2} = 0.84D$ that determines when the depressurization (pressurized to free-surface flow) occurs, comes from Yuan (1984), and León et al. (2010). However, with the shock-fitting approach of this chapter, the code becomes unstable as shown in Figure 6.7 for the test case $Va^* = 2.63$, $D = 0.053\,m$, $L = 10.7\,m$, $S_0 = 2\%$, and $k = 1.2$ of Hatcher et al. (2015).

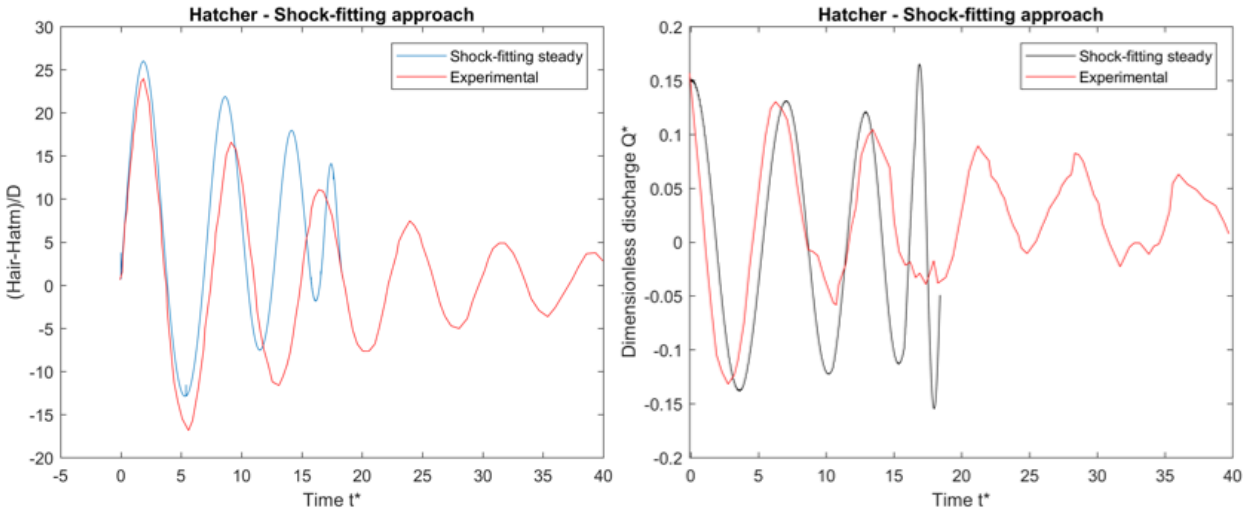

Figure 6.7: Unstable pressure of the air pocket against time (left graph) and dimensionless discharge against time (right) with the threshold values $y_{ref,1}$ and $y_{ref,2}$ for $V_a^{*0} = 2.63$, $Q^{*0} = 0.15$, $D = 0.053\,m$, $L = 10.7\,m$, $S_0 = 2\%$ and $k = 1.2$ (data experiments from Hatcher et al. (2015))

León et al. (2010) also encountered instability problems, when using a two-governing equation model that tries in particular to simulate pure free-surface flow that is about to pressurize. Threshold levels for piezometric head found by trial and error were used during pressurization to address the numerical instabilities of their finite volume model. To adress the instability of the shock-fitting approach shown in Figure 6.7, another method was considered in this study.

For the shock-fitting approach of this chapter, the second way to determine the interface will solve the remaining cause of instability. This second way considers that pressurization and depressurization are controlled by the equation (6-57):

$$L_u(t + dt) = L_u(t) + w \times \Delta t \qquad (6\text{-}57)$$

Every grid point which has an abscissa inferior to the position of the interface L_u, calculated by equation (6-57), is considered located in the pressurized flow and every grid point which has an abscissa superior to L_u, is considered located in the free-surface flow. By using equation (6-57), the code becomes stable and there is no program abortion.

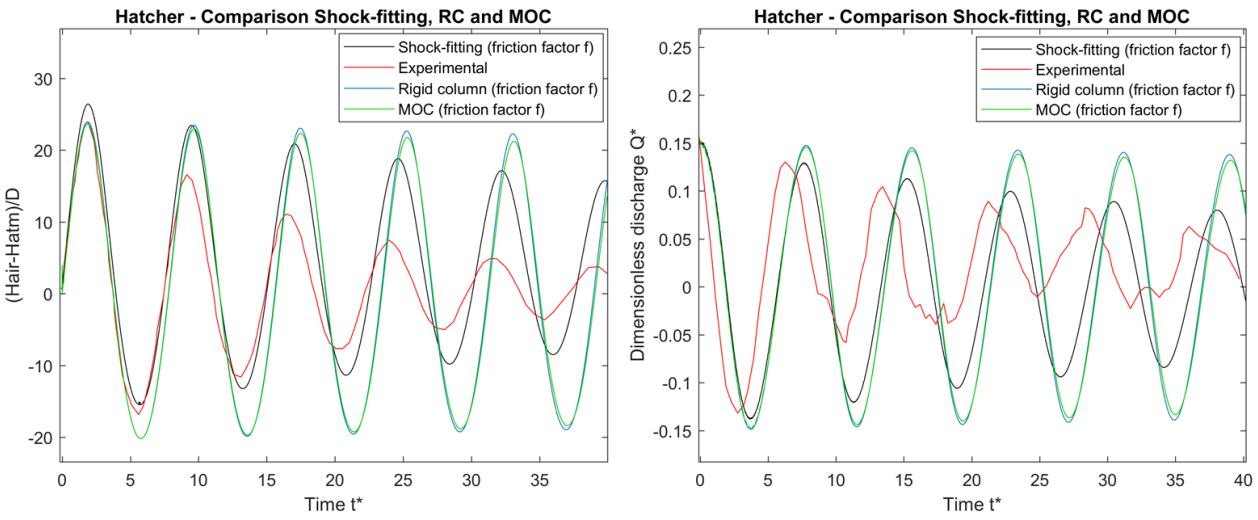

Figure 6.8 Stable pressure of the air pocket against time (left graph) and dimensionless discharge against time (right) with the calculation of the interface L_u for $V_a^{*0} = 2.63$, $Q^{*0} = 0.15$, $D = 0.053\ m$, $L = 10.7\ m$, $S_0 = 2\%$ and $k = 1.2$ (data experiments from Hatcher et al. (2015))

With a steady-state friction factor, the shock-fitting approach improves the pressure and discharge attenuation compared to the models, the rigid column model, and the method of characteristics model as seen in Figure 6.8, $V_a^{*0} = 2.63$, $Q^{*0} = 0.15$, $D = 0.102\ m$, $L = 10.7\ m$, $S_0 = 2\%$. The phase shift between the experimental and numerical values is also better in the case of the shock-fitting approach.

Unfortunately, the shock-fitting approach has a huge disadvantage. The duration of the simulation is very long which is quite common with this type of technique. In this case, the resolution of system of the non-linear equations of the model with algorithms like Newton-Raphson and Levenberg-Marquardt is one factor to explain this long time of simulation. Another reason is the very small time step used in the pressurized zone to fulfill the CFL condition, which is smaller than the time step required in the free-surface zone. This leads to more calculations and a longer simulation duration.

Moreover, the pressure and discharge are still overestimated by the shock-fitting method. The nature of the shock-fitting approach developed in this chapter can help explain the errors generated and the discrepancy between the numerical model and the experimental data.

There are different types of interpolations for the method of characteristics than the linear interpolation used in this chapter to obtain the velocity and pressure at R and S. There is the

Space-Line interpolation, the Reach Out in Space interpolation, the Time-Line interpolation, the Reach-back-in-Time interpolation described by Ghidaoui and Karney (1994). Quadratic, cubic and spline interpolations for the method of characteristics were also studied by Sibetheros et al. (1991) for the water hammer analysis.

The linear interpolations may lead to mass and momentum conservation problems according to Bousso and Fuamba (2014b), Politano et al. (2007) and León (2007). Moreover, the model of the negative interface used in this chapter may generate errors. By quoting León (2007): " When using the model of Song et al. (1984), open-channel surges cannot be modeled and negative interfaces are not adequately addressed." The model of the negative interface used in this chapter was inspired by Cardle (1984) which is similar to the one presented by Song et al. (1983). Furthermore, the hypothesis of only one surge front is questionable. Initiating multiple turbulent wave fronts may be necessary (Bousso et al. 2013).

The additional friction factor f' proposed in Chapter 4 can also be applied to the shock-fitting approach but the search for an optimal calibration factor C is unpractical. Knowing that only one simulation could take an hour with a common computer, making more than 30 simulations for each flow regime (Laminar, Turbulent and Mixed) with the shock-fitting approach to search for the optimal calibration factor C would not be worth it computationally wise. Indeed, the MOC and RC model combined with the additional friction factor f' already give good results with a rapid simulation duration (several seconds).

6.4 Conclusion

A shock-fitting approach was proposed in this chapter with the intention to improve the air pocket entrapment modelling compared to the models, the rigid column model, and the method of characteristics model. The shock-fitting approach consists in separately modelling the free-surface and the pressurized regions with the method of characteristics and in tracking the interface. If only the steady-state is applied, the results (air pocket pressure and discharge) given by the shock-fitting approach in this chapter are more accurate than the one given by the rigid colum and the method of characteristics models. Unfortunately, the simulation duration with the shock-fitting approach is too long and the slight improvement in accuracy is not worth it.

CHAPTER 7 IMPLEMENTATION OF THE RIGID COLUMN AND METHOD OF CHARACTERISTICS IN SWMM IN THE CASE OF THE AIR POCKET ENTRAPMENT IN STORMWATER SYSTEMS

7.1 Introduction

The Storm Water Management Model (SWMM) is an extended model used to simulate the flows from sewer systems, storm water runoff quantity and quality from primarily urban areas.

The current version of the software SWMM, developed by the U.S. Environmental Protection Agency (EPA), has many advantages. It has a large number of users and a community supporting it. The source codes of the computational engine and the GUI interface are also open source, which make them editable by the community. The free software SWMM also contains water quality and LID (Low Impact Development) options which are useful for further analysis. The idea behind this chapter is to present the results of the implementation of the rigid column and the method of characteristics models in SWMM in the case of the air pocket entrapment in a single reservoir-pipe system. The current version of SWMM has three existing routine models ("Steady Flow", "Kinematic Wave" and "Dynamic Wave") for the numerical simulation.

The calculation procedure of SWMM called "Dynamic Wave" has two algorithms of resolution, which are EXTRAN and SLOT. There are significant differences in solving between these two procedures but there is not much studies about the eventual differences yielded by these algorithms (Pachaly et al., 2020). The EXTRAN algorithm integrated in SWMM is explained in the official reports of the U.S. Environmental Protection Agency EPA (Rossman, 2006; 2010; 2016) whereas the SLOT algorithm in SWMM does not have any documentation as of yet (Pachaly et al., 2020). The dynamic wave analysis based on the EXTRAN algorithm solves the complete form of the Saint-Venant equations, namely the conservation of mass (7-1) and momentum (7-2) equations, for unsteady free-surface flow:

$$\frac{\partial A}{\partial t} + \frac{\partial Q}{\partial x} = 0, \tag{7-1}$$

$$\frac{\partial Q}{\partial t} + \frac{\partial (Q^2/A)}{\partial x} + gA\frac{\partial H}{\partial x} + gAS_f = 0, \tag{7-2}$$

where x is the distance, t is the time, A is the cross-sectional area, Q is the flow rate, H is the hydraulic head of water in conduit $(Z + Y)$, Z is the conduit invert elevation, Y is the conduit water depth, S_f is the friction slope and g is the acceleration of gravity.

By quoting Rossman (2017):

> The dynamic wave analysis "can account for channel storage, backwater effects, entrance/exit losses, flow reversal, and pressurized flow. Because it couples together the solution for both water levels at nodes and flow in conduits, it can be applied to any general network layout, even those containing multiple downstream diversions and loops".

Among the three routine models of SWMM, the dynamic wave model gives the most theoretically accurate results. The price of this method is that a small time step needs to be used to maintain numerical stability since the Saint-Venant equations are solved with an explicit method.

The "Kinematic Wave" model solves the continuity equation along with a simplified form of the momentum equation in each conduit (Rossman, 2006; 2010; 2016; 2017). This model is less accurate than the "Dynamic Wave" model but can maintain numerical stability with much larger time steps. Pressurized flow, flow reversal, entrance/exit losses, and backwater effect cannot be simulated by the "Kinematic Wave" model. Conduits with a slope $> 0.1\%$ with shallow flow and high velocity generally constitute the best domain of application of this model.

The least accurate routine model called "Steady Flow", which assumes that the flow is uniform and steady within each computational time step which means that inflow hydrographs at the upstream end of a conduit is translated to its downstream end with no delay or change in shape. The "Steady Flow" option is only appropriate for rough preliminary analysis of long-term continuous simulations according to Rossman (2017). According to Song et al. (1983), the "Steady Flow" and "Kinematic Wave" models are not suitable for a sewer network used a storage-conveyance system.

Details of the three routine models of SWMM can be found in the reports written by Rossman (2006; 2010; 2016; 2017). None of these models can simulate air pocket entrapment, hence, the role of this chapter is to implement air pocket entrapment models in SWMM to simulate the same problem that was studied all along this project without deleting the current available functionalities.

7.2 Methodology

The rigid column and the method of characteristics models that were studied in Chapters 4 and 5 will be added to the three existing routine models ("Steady Flow", "Kinematic Wave", and "Dynamic Wave"). The shock-fitting approach discussed in Chapter 6 has a too long simulation duration which makes it impractical, thus, it will not be implemented in the modified version of SWMM.

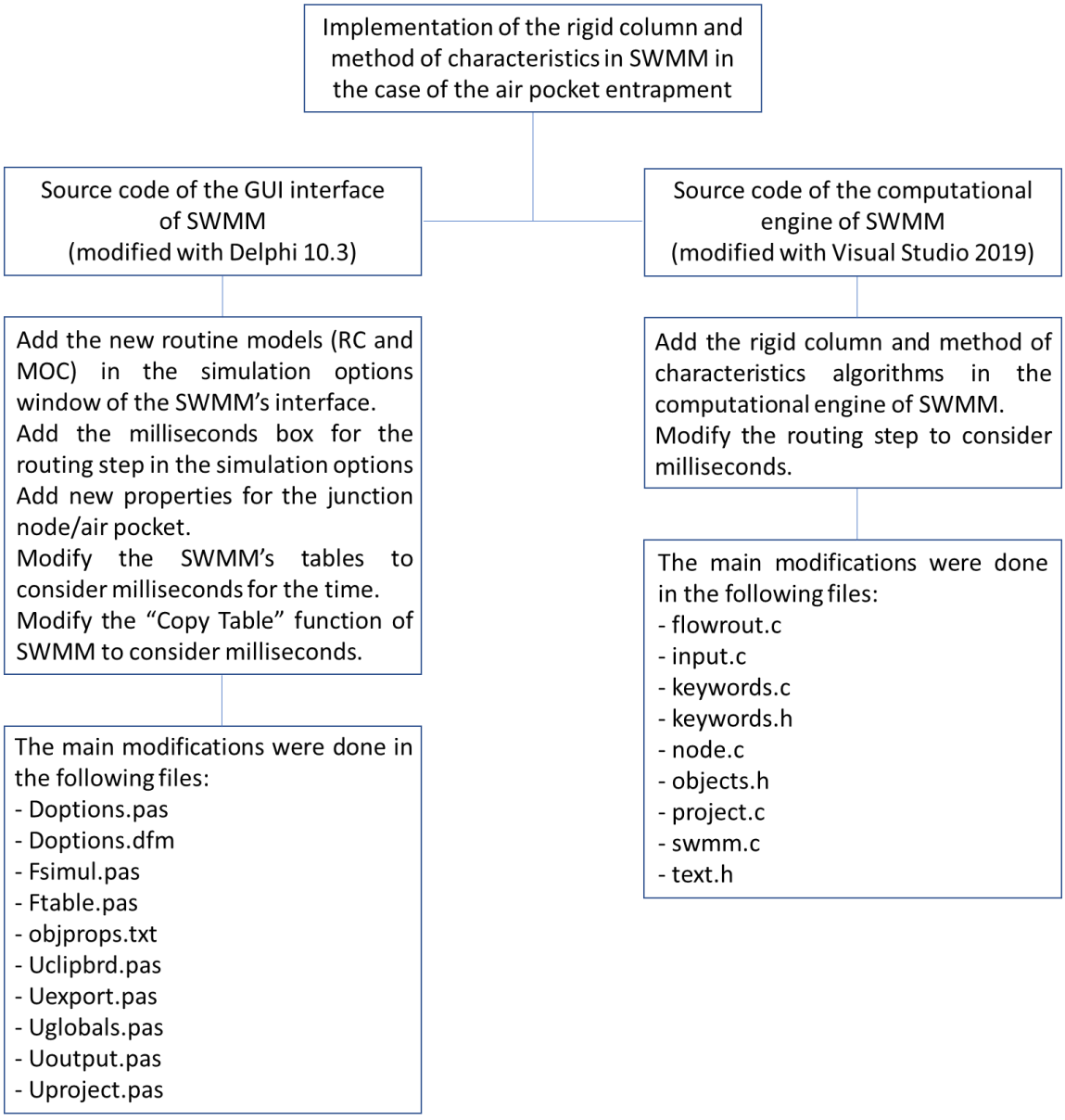

Figure 7.1 Implementation of the rigid column and method of characteristics in the case in SWMM in the case of air pocket entrapment

The source code of the computational engine of SWMM version 5.1.013 was modified in order to implement the rigid column and the method of characteristics models applied for the simple air pocket entrapment problem. The calculation procedure for each model was already explained in Chapters 4 and 5, the only difference is that there is no additional friction (only the steady-state friction factor f). The source code of the GUI interface of the software was also modified accordingly (see Figure 7.1).

7.3 Results

As shown in Figure 7.2, the reservoir is drawn on the left and the entrapped air pocket on the right. The two objects on SWMM are linked by the conduit.

Normally for the three original models of SWMM ("Steady Flow", "Kinematic Wave", and "Dynamic Wave"), the "junction node" represents a drainage system node, which can be a confluence of natural surface channels, manholes in a sewer system, or pipe connection fittings. However, with the rigid column and the method of characteristics models of this chapter, the "junction node" symbolizes the entrapped air pocket in Figure 7.2. This choice was made in order to keep a compatible version between the original version of SWMM and the modified one developed in this chapter.

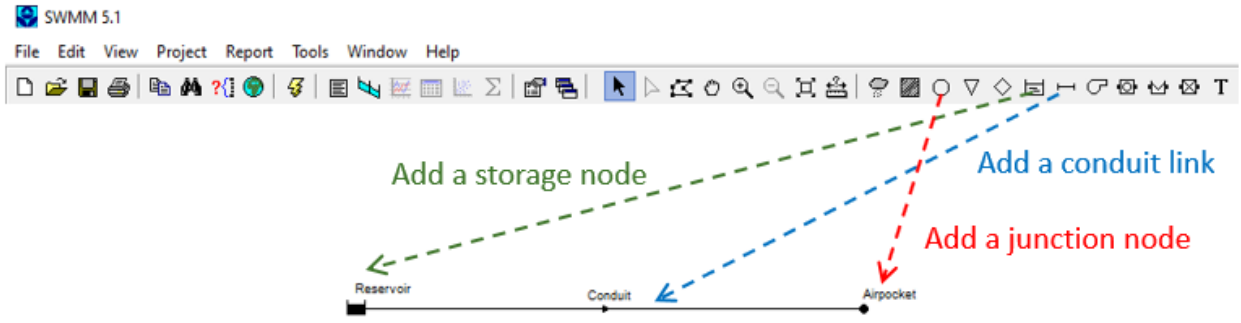

Figure 7.2 Illustration of the air pocket entrapment problem in SWMM

Figure 7.3, Figure 7.4, and Figure 7.5 show how to enter the proprieties of the problem in the modified version of SWMM. The air pocket $V_a^{*0} = 2.63$ from Hatcher et al. (2015) is used as an example and the data of the problem are the following:

$$H_{res} = 0.204\ m\ ($$

- Figure 7.3);
- $D = 0.053\ m$, $L = 10.7\ m$, $Q_0 = 0.0003\ m^3/s$, $K_{loss} = 2.9$ (Figure 7.4);
- $S_0 = 2\ \%$, $V_0 = 0.00039$, $f = 0.025$, $a = 1000\ m/s$, $k = 1.2$ (Figure 7.5).

Note that metric units were used (even for the initial discharge and volume of air pocket).

The speed of pressure wave a can be fixed in the modified version of SWMM. It was assumed as $1000\ m/s$ but it can also be approximated with Equation (4-22). Either way, the results do not vary much for the given example. The reasoning behind not enforcing the calculation of a with Equation (4-22). in the modified version of SWMM is to let the user change the value of a freely.

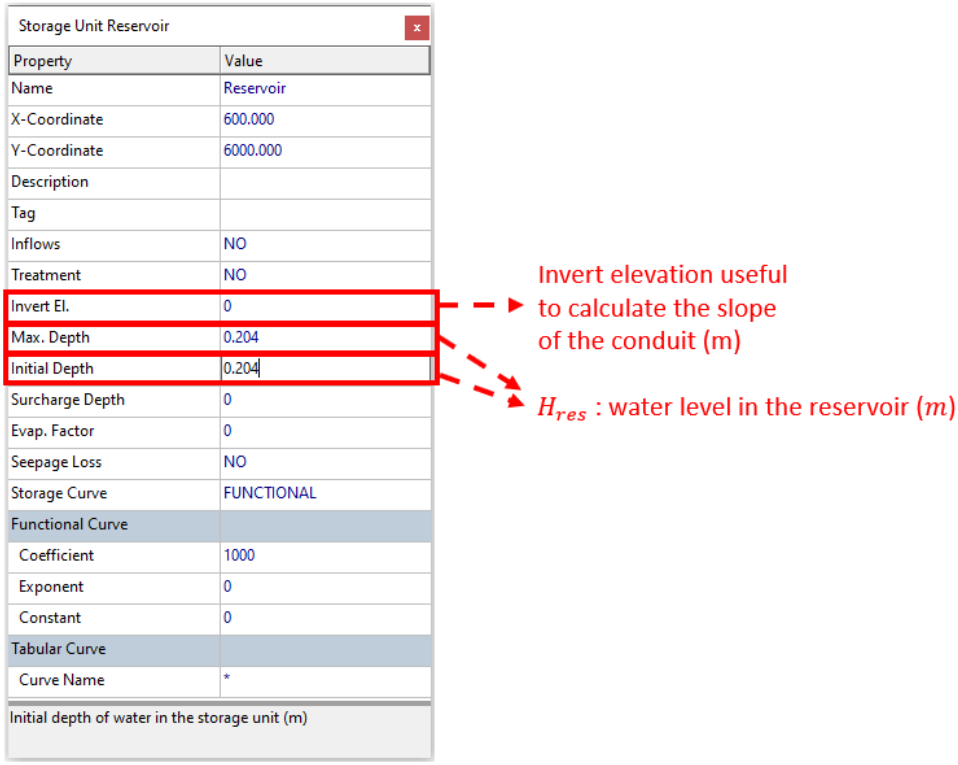

Figure 7.3 Reservoir properties in the modified version of SWMM

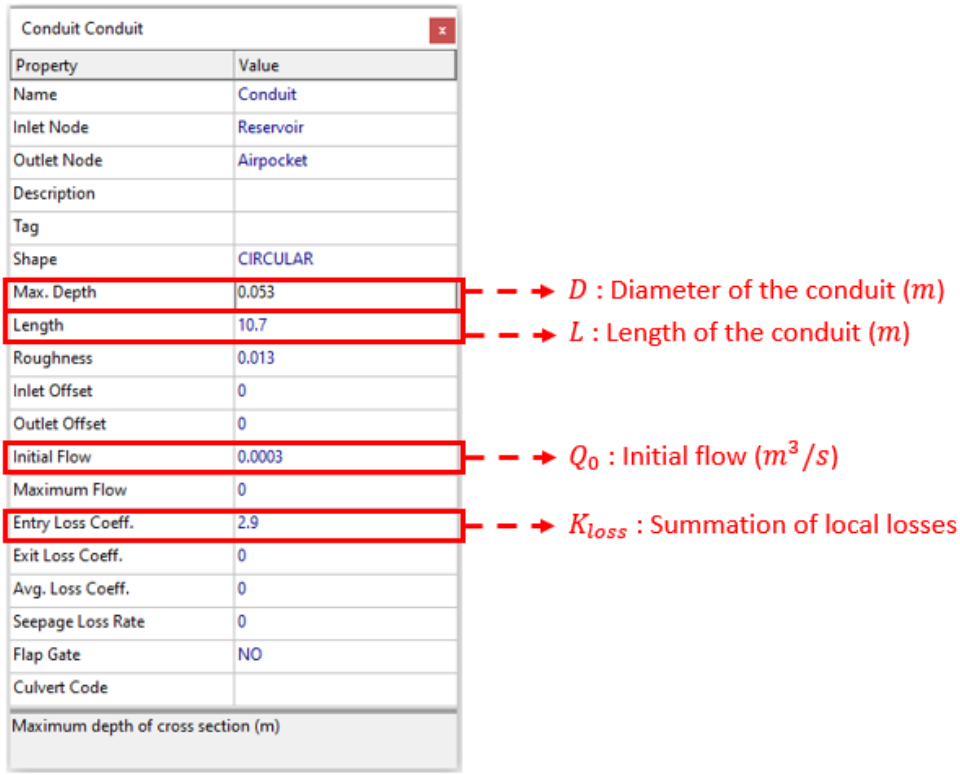

Figure 7.4 Conduit properties in the modified version of SWMM

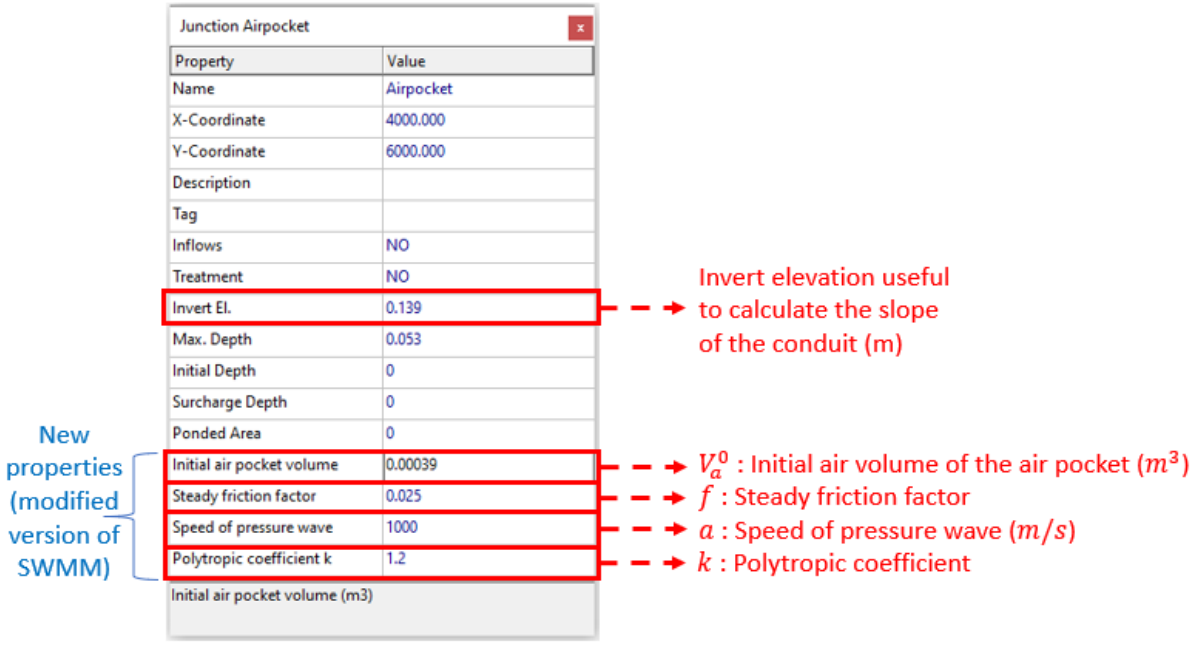

Figure 7.5 Junction/air pocket properties in the modified version of SWMM

As seen in Figure 7.5, in the “Junction node” window, four new properties have been added, which have been called “Initial air pocket volume”, “Steady friction factor”, “Speed of pressure wave” and “Polytropic coefficient”, respectively.

The models, the rigid column model, and the method of characteristics model were added in the routing model list as shown in Figure 7.6 with a red rectangle. Notice that there are three options for the rigid column model which represent the three different ways the rigid column equations (4-6), (4-7), and (4-8) are discretized and solved. The three options for the rigid column model are: The explicit Euler (also called forward Euler method), Implicit Euler (backward Euler method), and 4^{th} order Runge-Kutta.

In Chapters 4 and 5, the 4^{th} order Runge-Kutta was used to solve the rigid column equations because this numerical method gives good stability and accuracy. The explicit Euler method was added in the modified version of SWMM because it was easier to implement but to capture the variation in pressure accurately and to avoid instability, the 4^{th} order Runge-Kutta method is recommended. For this project, the implementation of the rigid column and the method of characteristics methods concerns only the single reservoir-pipe system.

In the future, it would be interesting to simulate air pocket entrapment in a large network. An idea to simulate unsteady flows in a large network would be to combine the rigid column or the method of characteristics models (for the parts of the networks with an entrapped air pocket) and the “Dynamic Wave” routine model of SWMM such as EXTRAN or SLOT (for the parts of the networks without any entrapped air pocket).

For the reporting step, a millisecond box was also added, as shown by another red rectangle. The reason for adding the millisecond box will be explained later.

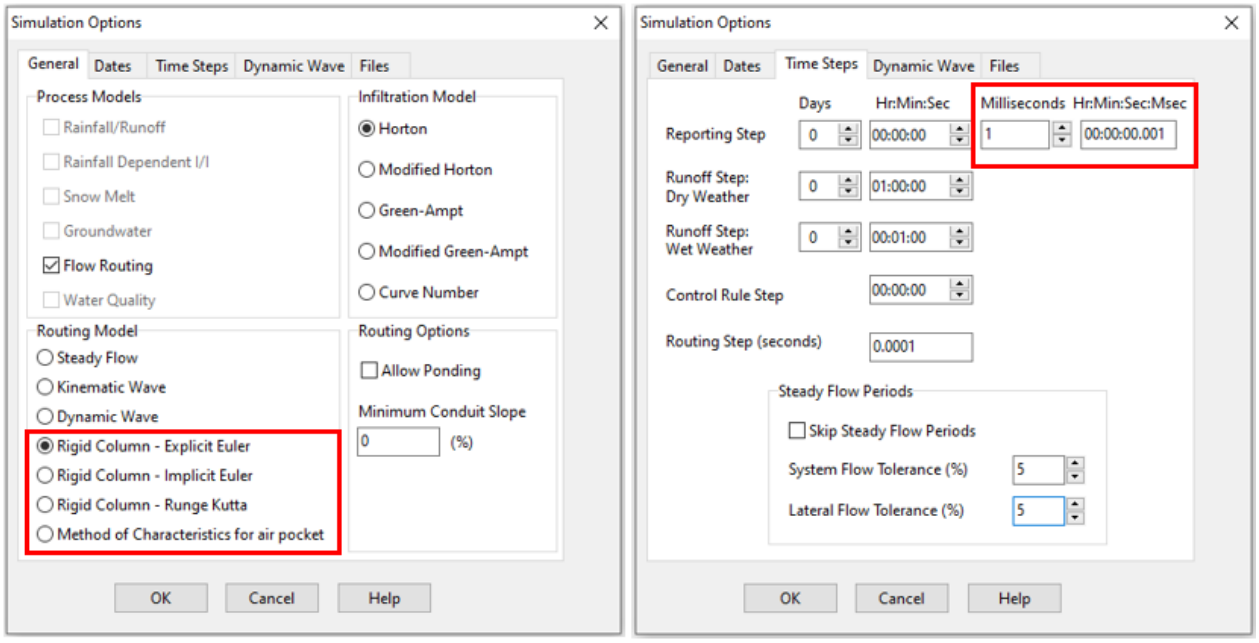

Figure 7.6 Simulation options in the modified version of SWMM

As shown in Figure 7.7, in order to plot the graph of the discharge against time, a “Time Series Plot” needs to be created with “Link” as the “Object Type”, “Conduit” as the “Object Name” and “Flow” as the “Variable”.

In order to plot the graph of the pressure of the air pocket against time, a “Time Series Plot” needs to be created with “Node” as the “Object Type”, “Airpocket” as the “Object Name” and “Depth” as the “Variable”.

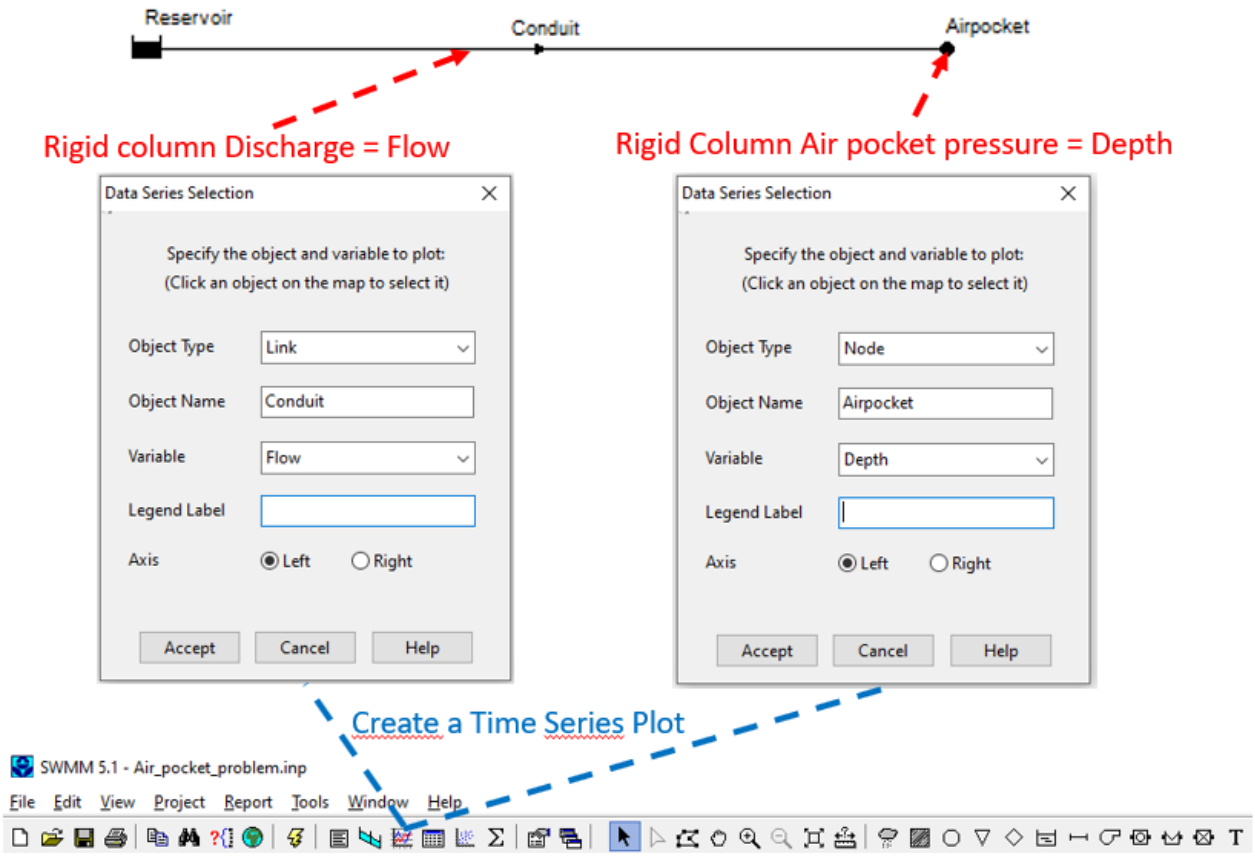

Figure 7.7 Windows of modified version of SWMM to plot the discharge against time (left) and the air pocket pressure against time (right)

The reason for adding the millisecond box in Figure 7.6 will now be explained. - As shown in Figure 7.8, the graphs of the discharge against time and the pressure of the air pocket against time simulated with the method of characteristics give distorted results with a reporting step of one second and a time step of 0.001 second. Adding the millisecond box in Figure 7.6 allows the user of the modified version of SWMM to set the reporting step equal to $0.001\ s$ which permits to find the desired behavior for the pressure and flow rate graphs (see Figure 7.9) like what was obtained in Chapters 4 and 5.

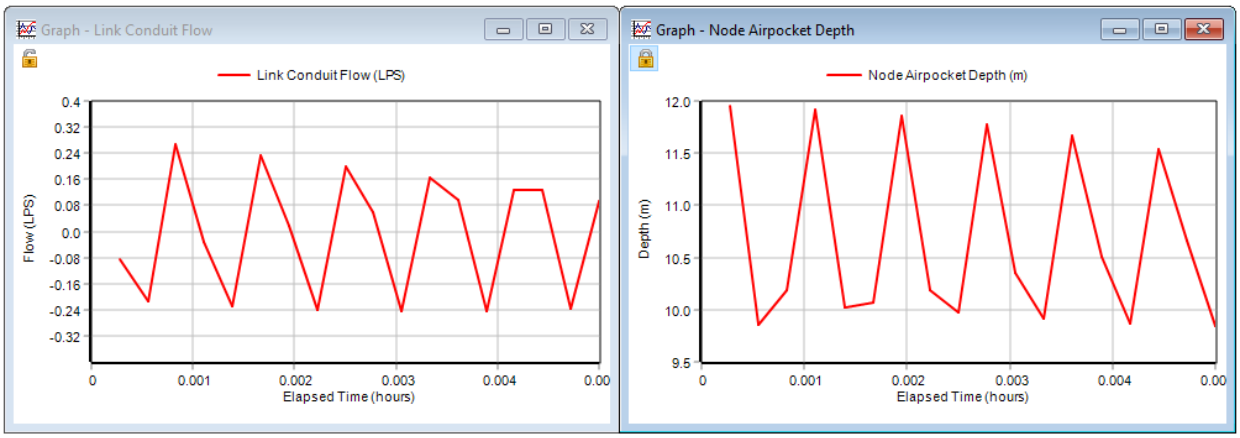

Figure 7.8 Discharge against time in liters per second (left graph) and pressure of the air pocket against time (right graph) simulated with the method of characteristics on SWMM for the Reporting_Step=1 s and Routing_Step=0.001 s

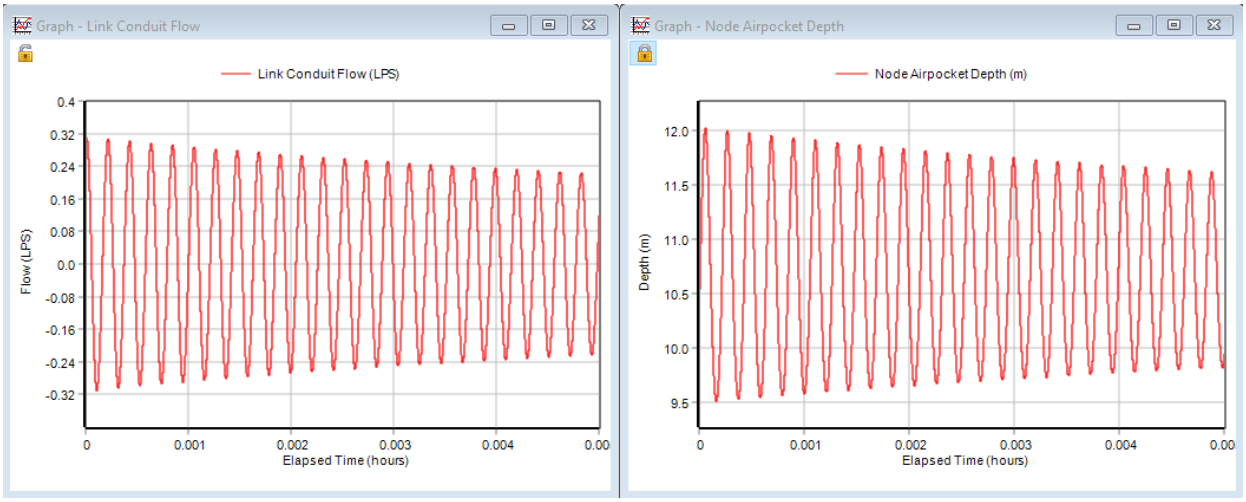

Figure 7.9 Discharge against time in liters per second (left graph) and pressure of the air pocket against time (right graph) simulated with the method of characteristics on SWMM for the Reporting_Step=1 ms and Routing_Step=0.001 s

Table 7.1 Discharge against time in liters per second (left table), pressure of the air pocket against time (right table) and Copy Table Window on SWMM

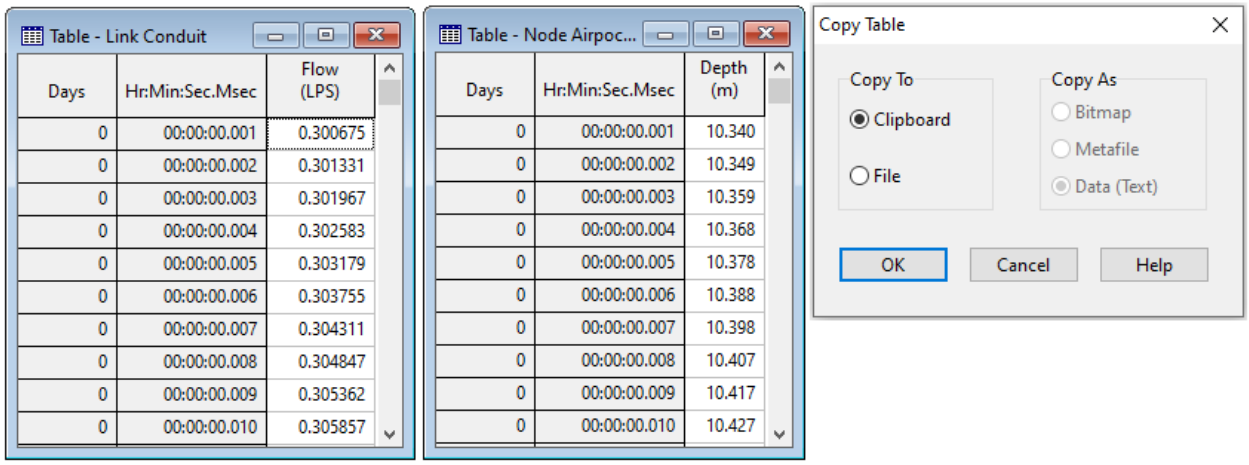

Table - Link Conduit

Days	Hr:Min:Sec.Msec	Flow (LPS)
0	00:00:00.001	0.300675
0	00:00:00.002	0.301331
0	00:00:00.003	0.301967
0	00:00:00.004	0.302583
0	00:00:00.005	0.303179
0	00:00:00.006	0.303755
0	00:00:00.007	0.304311
0	00:00:00.008	0.304847
0	00:00:00.009	0.305362
0	00:00:00.010	0.305857

Table - Node Airpoc...

Days	Hr:Min:Sec.Msec	Depth (m)
0	00:00:00.001	10.340
0	00:00:00.002	10.349
0	00:00:00.003	10.359
0	00:00:00.004	10.368
0	00:00:00.005	10.378
0	00:00:00.006	10.388
0	00:00:00.007	10.398
0	00:00:00.008	10.407
0	00:00:00.009	10.417
0	00:00:00.010	10.427

The pressure of the air pocket and the discharge against time can also be visualized in a table form in the modified version of SWMM (see Table 7.1). The time is represented by the column “Hr:Min:Sec.Msec” which decomposes in order of the hours, minutes, seconds, and milliseconds. The milliseconds in the columns were added because they were absent from the original version of SWMM with a minimum reporting step equal to one second.

The columns can also be copied and pasted in an Excel file (the same way as the original SWMM) in order to make calculations on the desired values, change legend, compare multiple graphs, etc. The Excel formula to separate the different fields (hours, minutes, seconds and milliseconds) of the values in the column “Hr:Min:Sec.Msec” can be “STXT()” in the French version of Excel or “MID()” in the English version of Excel. By treating the values of Table 7.1, it is possible to plot the graphs of the pressure of the air pocket and the discharge against time in Excel (see Figure 7.10). To sum up, the pressure and flow rate graphs can either be plotted directly in SWMM (Figure 7.9) or plotted in Excel after transferring the corresponding data from the modified version of SWMM to Excel (Figure 7.10).

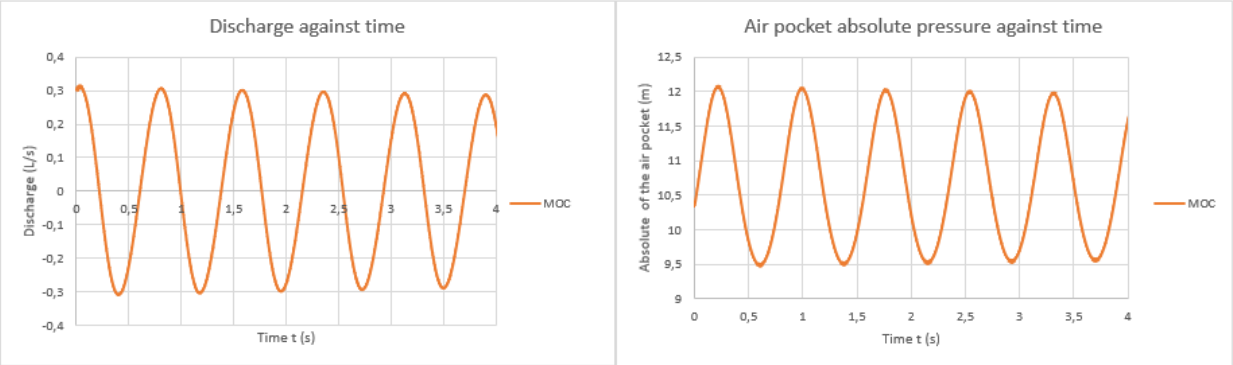

Figure 7.10 Discharge against time in liters per second (left graph) and pressure of the air pocket against time (right graph) simulated with the method of characteristics on Excel for the Reporting_Step=1 ms and Routing_Step=0.001 s

7.4 Conclusion

The models, the rigid column model, and the method of characteristics model used to simulate the transient flows causing air pocket entrapment in the single reservoir-pipe system problem studied in Chapters 4 and 5 have been implemented in the SWMM software. Only the steady-state friction factor was used. The work is incomplete because the models for air pocket entrapment in this modified version of SWMM do not work for another application. Further investigation is needed to extend the numerical simulation to a larger network composed with pipes with or without entrapped air pocket. A way to do that could be to combine the ”Dynamic Wave” model of SWMM with an air pocket entrapment model such as the one studied in this project (rigid column, method of characteristics, etc.).

CHAPTER 8 GENERAL DISCUSSION

The literature review of Chapters 2 and 4 show that there are numerous numerical models for transient flows in stormwater systems, but none of these models fully resolves the problem related to flow dynamics under the air pocket entrapment. The rigid column and the method of characteristics models are common models used in the literature to model the air pocket entrapment process in stormwater systems but these models overestimate the pressure peaks if only the Darcy-Weisbach steady-state friction factor is used. The purpose of the literature review of the unsteady friction factors in Chapter 2 was to find an additional friction factor that would lead to better simulated results.

The main contributions of this master thesis, besides carrying a literature review, writing appropriate computer codes to numerically solve the equations, and running experiments to extract relevant experimental data, are:

1. The results of the air pocket pressure and discharge simulated by the two well-known models, the rigid column model, and the method of characteristics model have been improved by introducing an additional friction factor calibrated as a function of the air pocket.

2. It was found that the shock-fitting approach takes very long time to solve the transient flow, which is due to Courant-Friedrichs-Lewy (CFL) condition restricted by the acoustic wave speed and due to the resolution of a non-linear system of equations. In addition, it was found that the common pressurization/depressurization criteria used in the Finite Volume method, which is based on the pressure, causes instability in the shock-fitting approach based on the finite difference methods. To improve the instability, another criterion was proposed to obtain more stability This criterion is based on the explicit calculation of the position of the interface that separates the open-channel flow and the pressurized flow.

3- The SWMM software was upgraded for the first time by implementing the rigid column model and the method of characteristics model in this software. Now, the SWMM software can solve the air pocket entrapment problem in transient flows occurring in a single reservoir-pipe system. In addition, the reporting step in the SWMM software is modified to milliseconds, which is needed to model transient flows following air pocket entrapment in stormwater systems.

CHAPTER 9 CONCLUSION AND RECOMMENDATIONS

The goal of this project was to improve the numerical models used to simulate air pocket entrapment problems followed by partially pressurized transient flows in storm water systems. In Chapters 4 and 5, two well-known models, the rigid column model, and a modified version of the Saint-Venant equations (solved with MOC) were used with and without an additional friction factor and it was found that adding an additional friction factor could yield better numerical results. Those numerical results were compared with experimental data from the Hydraulics Laboratory of "École Polytechnique de Montréal" and the article of Hatcher et al. (2015). In addition, it was observed that if the same polytropic coefficient k is used with both models experience a phase shift between the numerical solutions and experimental data depending on the size of the entrapped air pocket. It also was shown that the value of the polytropic coefficient k influenced the phase of the numerical reuslts. Thus, changing the value of k can decrease the phase shift and give more accurate results. However, how to select the right value of k? This question has not been answered clearly, as the heat transfer mechanism between the air, water, and pipe wall is so complicated. Also, the literature is not unanimous about the value of k to choose. In transient flow modelling (not necessarily air pocket entrapment), some authors select $k = 1.2$, others take $k = 1.4$ (adiabatic) or another value. However, due to rapid nature of the transient flow in SWSs, the adiabatic process, $k = 1.4$, has been more recommended. The value of k is often chosen to have the more accurate numerical results. It is also possible that the phase shift is due other factors that are not included in mathematical models for their complexities, which make these models impractical such as turbulent shear stresses, or the dynamic of the air pocket.

The additional friction factor in Chapter 4 was found for only some particular ranges of air pocket size. For further analysis, it would be interesting to continue the study of the additional friction factor on more examples and test cases as well as different air pocket sizes, pipe lengths, pipe diameter, pipe material, water levels in the upstream reservoir, etc. Another idea would be to avoid having to calibrate the coefficient C of the additional friction factor with experimental data. This could be done by finding an explicit formula for this coefficient C which would clearly be an improvement because in that case, no search for the optimal coefficient C would be needed. For further research, it could be interesting to study the finite-volume method in the case of air

pocket entrapment and to combine it with the proposed additional friction factor. Indeed, the finite-volume approach does not use mathematical artifices to solve the mass and continuity equations like the method of characteristics, for example.

In Chapter 6, the shock-fitting approach with the steady-state friction factor was developed and gave good numerical approximation of the pressure of the air pocket and the flow rate during the air pocket entrapment process, but the duration of the simulation is too long mainly due to the resolution of systems of non-linear equations. Unfortunately, the accuracy of the results obtained by the shock-fitting approach is not worth the computational burden. Thus, the rigid column model, and the method of characteristics model are recommended over this shock-fitting approach.

Finally, in Chapter 7, the rigid column model, and the method of characteristics model applied to the air pocket entrapment process with a steady-state friction factor were implemented in the software SWMM in a single reservoir-pipe system. However, this is just the first step of the implementation of an air pocket entrapment model in SWMM. Further research need to be done to model air pocket entrapment in more complex situations with larger networks containing, converging, diverging pipes, multiple reservoirs, pipes, pumps, etc. A more complete model that takes into account the size of air pockets could then be added to SWMM to share it to all the research community.

BIBLIOGRAPHY

Abuiziah, I., Ahmed, O., & Driss, O. (2013). Simulating Flow Transientsin Conveying Pipeline Systems by Rigid Column and Full Elastic Methods: Pump Combined with Air Chamber.

Adamkowski, A., & Lewandowski, M. (2004). Unsteady friction modelling in transient pipe flow simulation. *Transactions of the Institute of Fluid-Flow Machinery, 115*, 83-97.

Adamkowski, A., Lewandowski, M. (2006). Experimental examination of unsteady friction models for transient pipe flow simulation. *Journal of Fluids Engineering* 128(11), 1351–1363.

Altaie, H., & Dreyfuss, P. (2018). *Numerical Solutions for 2D Depth-Averaged Shallow Water Equations.* Paper presented at the International Mathematical Forum.

Alves, I. N., Shoham, O., & Taitel, Y. (1993). Drift velocity of elongated bubbles in inclined pipes. *Chemical engineering science, 48*(17), 3063-3070.

Anderson, J. D., & Wendt, J. (1995). *Computational fluid dynamics* (Vol. 206): Springer.

Bashiri, H., Shirai, H., Hosoda, T., & Karney, B. (2020). Experimental and numerical simulation of bidirectional propagation of an air cavity. *Journal of Hydraulic Research, 58*(4), 638-652.

Bazargan-Lari, M. R., Kerachian, R., Afshar, H., & Bashi-Azghadi, S. N. (2013). Developing an optimal valve closing rule curve for real-time pressure control in pipes. *Journal of Mechanical Science technology, 27*(1), 215-225.

Benjamin, T. B. (1968). Gravity currents and related phenomena. *Journal of Fluid Mechanics, 31*(2), 209-248.

Bergant, A., Ross Simpson, A., & Vìtkovsk, J. (2001). Developments in unsteady pipe flow friction modelling. *Journal of Hydraulic Research, 39*(3), 249-257.

Bergant, A., Simpson, A. R., & Scotland, M. (1994). *Estimating unsteady friction in transient cavitating pipe flow*. Paper presented at the 2nd International Conference on Water Pipeline Systems, Edinburgh, Scotland, May, p. 3 - 15.

Bergant, A., Tijsseling, A. S., Vítkovský, J. P., Covas, D. I., Simpson, A. R., & Lambert, M. F. (2008). *Parameters affecting water-hammer wave attenuation, shape and timing—Part 1: Mathematical tools*. Journal of Hydraulic Research, 46(3), 373-381.

Besharat, M., Coronado-Hernández, O. E., Fuertes-Miquel, V. S., Viseu, M. T., & Ramos, H. M. (2020). Computational fluid dynamics for sub-atmospheric pressure analysis in pipe drainage. *Journal of Hydraulic Research, 58*(4), 553-565.

Bousso, S. (2010). *Modélisation expérimentale des écoulements transitoires avec poches d'air emprisonnées dans les réseaux de drainage urbain* (Masters thesis, École Polytechnique de Montréal). Retrieved from: https://publications.polymtl.ca/367/1/2010_SambaBousso.pdf (accessed March 21, 2020).

Bousso, S., Daynou, M., & Fuamba, M. (2013a). Numerical modeling of mixed flows in storm water systems: Critical review of literature. *Journal of Hydraulic Engineering, 139*(4), 385-396. doi:10.1061/(asce)hy.1943-7900.0000680

Bousso, S., Daynou, M., & Fuamba, M. (2014a). Mixed flows with depressurizing wavefront in circular pipe. *Journal of Irrigation and Drainage Engineering, 140*(1). doi:10.1061/(asce)ir.1943-4774.0000665

Bousso, S., & Fuamba, M. (2013b). Numerical simulation of unsteady friction in transient two-phase flow with Godunov method. *Journal of Water Resources, 5*(11), 1048.

Bousso, S., & Fuamba, M. (2014b). Numerical and experimental analysis of the pressurized wave front in a circular pipe. *Journal of Hydraulic Engineering, 140*(3), 300-312.

Brunone, B., Golia, U., & Greco, M. (1991). Some remarks on the momentum equation for fast transients. *Paper presented at the Proceedings of the International Meeting on Hydraulic Transients with Column Separation*.

Brunone, B., Golia, U., & Greco, M. (1995). Effects of two-dimensionality on pipe transients modeling. *Journal of Hydraulic Engineering, 121*(12), 906-912.

Brunone, B., Karney, B. W., Mecarelli, M., Ferrante, M., & management. (2000). Velocity profiles and unsteady pipe friction in transient flow. *Journal of water resources planning, 126*(4), 236-244.

Cardie, J. A., Song, C. C., & Yuan, M. (1989). Measurements of mixed transient flows. *Journal of Hydraulic Engineering, 115*(2), 169-182.

Cardle, J. (1984). *An investigation of hydraulic transients in combination free surface and pressurized flows.* Ph.D. Thesis Minnesota Univ., Minneapolis.

Carravetta, A., Golia, U., & Greco, M. (1992). On the spontaneous damping of pressure oscillations in water hammer transients. *Proc., 23rd Convegno Nazionale di Idraulica e Construzioni Idrauliche, 4*, 67-79.

Cataño-Lopera, Y. A., Tokyay, T. E., Martin, J. E., Schmidt, A. R., Lanyon, R., Fitzpatrick, K., . . . García, M. H. (2014). Modeling of a transient event in the tunnel and reservoir plan system in Chicago, Illinois. *Journal of Hydraulic Engineering, 140*(9), 05014005.

Chaudhry, M. H. (2007). *Open-channel flow*: Springer Science & Business Media.

Chaudhry, M. H. (2014). *Applied hydraulic transients*: Springer.

Chegini, T., & Leon, A. S. (2020). Numerical investigation of field-scale geysers in a vertical shaft. *Journal of Hydraulic Research, 58*(3), 503-515.

Chen, W.-F., & Liew, J. R. (2002). *The civil engineering handbook*: Crc Press.

Cunge, J. (1980). Practical aspects of computational river hydraulics. *Pitman Publishing Ltd. London , 420*.

Cunge, J. A., & Wegner, M. (1964). Intégration numérique des équations d'écoulement de Barré de Saint-Venant par un schéma implicite de différences finies. *La Houille Blanche*(1), 33-39.

Daynou, M. (2012). Contributions à la modélisation hydrodynamique des écoulements transitoires dans les réseaux de drainage urbain : théories et études de cas (PhD thesis, École Polytechnique de Montréal). Retrieved from: https://publications.polymtl.ca/1037/1/2012_MathurinDaynou.pdf (accessed March 21, 2020).

Daynou, M., Fuamba, M., & Mahdi, T.-F. (2009). Manhole Storage Capacity Influence on Transient Flow Modeling during Storm Sewer Flooding Event. *Journal of Water Management Modeling*.

De Martino, G., Fontana, N., & Giugni, M. (2008). Transient flow caused by air expulsion through an orifice. *Journal of Hydraulic Engineering, 134*(9), 1395-1399.

Després, B., & Dubois, F. (2005). *Systèmes hyperboliques de lois de conservation: Application à la dynamique des gaz*. Editions Ecole Polytechnique.

Eckhardt, B. (2009). Introduction. Turbulence transition in pipe flow: 125th anniversary of the publication of Reynolds' paper. In: The Royal Society London.

El Abboudi, N. (2000). *Modélisation des écoulements en charge*. Université du Québec, Institut national de la recherche scientifique,

Elbashir, M., & Amoah, S. (2007). Hydraulic Transient in a Pipeline (Using Computer Model to Calculate and Simulate Transient).

EL-Turki, A. (2013). *Modeling of hydraulic transients in closed conduits.* (Degree of Master of Science, Colorado State University).

Freni, G., Ferreri, G., & Tomaselli, P. (2010). Ability of software SWMM to simulate transient sewer smooth pressurization. *NOVATECH*.

Fuamba, M. (1997). *Transient Flows Modelling in Drainage Systems Networks.* Ph. D. dissertation, Katholieke Universiteit Leuven, Belgium),

Fuamba, M. (2002). Contribution on transient flow modelling in storm sewers. *Journal of Hydraulic Research*, *40*(6), 685-693.

Fuamba, M., Daynou, M., Bousso, S., & Rokhzadi, A. (2018). *Modeling complex boundary conditions during transient two-phase mixed flow in storm water systems (SWS).* Paper presented at the 13th International Conference on Pressure Surges, Bordeaux, France.

Fuertes-Miquel, V. S., & Iglesias-Rey, P. L. J. J. o. H. E. (2015). Discussion of "Numerical Modeling of Mixed Flows in Storm Water Systems: Critical Review of Literature" by Samba Bousso, Mathurin Daynou, and Musandji Fuamba. *141*(2), 07014018.

Garg, R., & Kumar, A. (2018). Analysis of Hydraulic Transients in a Reservoir-Valve-Pipeline Arrangement by Using Method of Characteristics (MOC). Almora, Uttarakhand, India, April.

Garg, R., & Kumar, A. (2018). Analysis of Hydraulic Transients in a Reservoir-Valve-Pipeline Arrangement by Using Method of Characteristics (MOC). *Almora, Uttarakhand, India, Apr*.

Ghidaoui, M. S., & Karney, B. W. (1994). Equivalent differential equations in fixed-grid characteristics method. *Journal of Hydraulic Engineering, 120*(10), 1159-1175.

Ghidaoui, M. S., Zhao, M., McInnis, D. A., & Axworthy, D. H. (2005). A review of water hammer theory and practice. *Appl. Mech. Rev.*, *58*(1), 49-76.

Goldberg, D. E., & Benjamin Wylie, E. (1983). Characteristics method using time-line interpolations. *Journal of Hydraulic Engineering, 109*(5), 670-683.

Gong, J., Lambert, M. F., Simpson, A. R., & Zecchin, A. C. (2014). Detection of localized deterioration distributed along single pipelines by reconstructive MOC analysis. *Journal of Hydraulic Engineering, 140*(2), 190-198.

Graf, W. H., & Altinakar, M. S. (2000). *Hydraulique fluviale: écoulement et phénomènes de transport dans les canaux à géométrie simple* (Vol. 16): PPUR presses polytechniques.

Graze, H. (1968). *A rational thermodynamic equation for air chamber design.* Paper presented at the 3rd Australasian Conf. on Hydraulics and Fluid Mechanics.

Guo, Q., & Song, C. C. (1990). Surging in urban storm drainage systems. *Journal of Hydraulic Engineering, 116*(12), 1523-1537.

Guo, Q., & Song, C. C. (1991). Dropshaft hydrodynamics under transient conditions. *Journal of Hydraulic Engineering, 117*(8), 1042-1055.

Hager, W. (1999). Cavity outflow from a nearly horizontal pipe. *International journal of multiphase flow, 25*(2), 349-364.

Hanif Chaudhry, M., & Prashanth Reddy, H. (2011). Mathematical modeling of lake tap flows. *Journal of Hydraulic Engineering, 137*(5), 611-614.

Hatcher, T. M., Malekpour, A., Vasconcelos, J., & Karney, B. (2015). Comparing unsteady modeling approaches of surges caused by sudden air pocket compression. *Journal of Water Management Modeling*. 23: C392. https://doi.org/10.14796/JWMM.C392

Hatcher, T. M., & Vasconcelos, J. G. (2017). Peak Pressure Surges and Pressure Damping Following Sudden Air Pocket Compression. *Journal of Hydraulic Engineering, 143*(4), 04016094. doi:doi:10.1061/(ASCE)HY.1943-7900.0001251

Holly Jr, F. M., & Preissmann, A. (1977). Accurate calculation of transport in two dimensions. *Journal of the Hydraulics division, 103*(ASCE 13336 Proceeding).

Holmboe, E. L., & Rouleau, W. T. (1967). The effect of viscous shear on transients in liquid lines. *ASME. Journal of Basic Engineering*. 89(1): 174–180. Retrieved from: https://doi.org/10.1115/1.3609549 (accessed May 8, 2020).

Huber, W. C., Dickinson, R. E., & Barnwell, T. O. (1988). *Storm water management model, version 4: user's manual*: Environmental Research Laboratory, Office of Research and Development, US. Retrieved from: http://www.dynsystem.com/netstorm/docs/swmm4manuals.pdf (accessed August 20, 2020).

Hudson, J. (1999). Numerical techniques for the shallow water equations. *Numerical Analysis Report, 2*, 99. Retrieved from: https://www.reading.ac.uk/web/files/maths/02-99.pdf (accessed January 15, 2021).

Izquierdo, J., Iglesias, P. J. M., & Modelling, C. (2002). Mathematical modelling of hydraulic transients in simple systems. *Mathematical Computer Modelling, 35*(7-8), 801-812.

Jang, T. U., Wu, Y., Xu, Y., Newman, J., & Sun, Q. (2016). Efficient quasi-two-dimensional water hammer model on a characteristic grid. *Journal of Hydraulic Engineering*, 142(12), 06016019.

Jung, B. S., & Karney, B. (2017). A practical overview of unsteady pipe flow modeling: from physics to numerical solutions. *Urban Water Journal, 14*(5), 502-508.

Karney, B. W. (1984). *Analysis of fluid transients in large distribution networks* (T). University of British Columbia. Retrieved from: https://open.library.ubc.ca/collections/ubctheses/831/items/1.0062640 (accessed January 8, 2021).

Kjerrumgaard Jensen, R., Kær Larsen, J., Lindgren Lassen, K., Mandø, M., & Andreasen, A. (2018). Implementation and validation of a free open source 1d water hammer code. *Fluids, 3*(3), 64.

Kodura, A. (2016). An analysis of the impact of valve closure time on the course of water hammer. *Archives of Hydro-Engineering and Environmental Mechanics, 63*(1), 35-45.

Landry, C., Nicolet, C., Bergant, A., Müller, A., & Avellan, F. (2012). *Modeling of unsteady friction and viscoelastic damping in piping systems.* Paper presented at the IOP Conference Series: Earth and Environmental Science.

Leaf, G., & Chawla, T. (1977). *Survey of numerical methods for hydraulic transients*, report, Argonne National Laboratory, Argonne, Illinois,. Retrieved from: https://www.osti.gov/servlets/purl/5161666 (accessed January 15, 2021).

Lee, N., & Martin, C. (1999). *Experimental and analytical investigation of entrapped air in a horizontal pipe.* Paper presented at the Proc., 3rd ASME/JSME Joint Fluids Engineering Conf.

Lee, N. H. (2005). *Effect of pressurization and expulsion of entrapped air in pipelines* (Doctoral dissertation, Georgia Institute of Technology).

Leendertse, J. J. (1967). *Aspects of a computational model for long-period water-wave propagation*. Santa Monica, CA: RAND Corporation, 1967. Retrieved from: https://www.rand.org/pubs/research_memoranda/RM5294.html (accessed November 4, 2020).

León, A., & Oberg, N. (2015). *Illinois transient model two-equation model V. 1.5*. Retrieved from: https://www.researchgate.net/profile/Arturo-Leon-2/publication/239588823_ILLINOIS_TRANSIENT_MODEL_TWO-EQUATION_MODEL_V_12_User%27s_Manual_May_2010/links/597664fa0f7e9b4016bc478f/ILLINOIS-TRANSIENT-MODEL-TWO-EQUATION-MODEL-V-12-Users-Manual-May-2010.pdf (accessed January 15, 2021).

León, A. S. (2007). *Improved modeling of unsteady free surface, pressurized and mixed flows in storm-sewer systems*. Ph.D. thesis, Univ. of Illinois, Urbana-Champaign, IL.

León, A. S., Ghidaoui, M. S., Schmidt, A. R., & Garcia, M. H. (2008). Efficient second-order accurate shock-capturing scheme for modeling one-and two-phase water hammer flows. *Journal of Hydraulic Engineering*, *134*(7), 970-983.

León, A. S., Ghidaoui, M. S., Schmidt, A. R., & García, M. H. (2010). A robust two-equation model for transient-mixed flows. *Journal of Hydraulic Research*, *48*(1), 44-56.

León, A., Oberg, N., Schmidt, A. R., & Garcia, M. H. (2011). Illinois transient model: simulating the flow dynamics in combined storm sewer systems. *Journal of Water Management Modeling.* Retrieved from: https://www.chijournal.org/Content/Files/R241-02.pdf (accessed January 15, 2021).

Li, J., & McCorquodale, A. (1999). Modeling mixed flow in storm sewers. *Journal of Hydraulic Engineering*, *125*(11), 1170-1180.

Liang, D., Falconer, R. A., & Lin, B. (2006). Comparison Between TVD-MacCormack and ADI-Type Solvers of the Shallow Water Equations Simple. *Advances in water resources*, *29*(12), 1833-1845.

Liou, C. P., & Hunt, W. A. (1996). Filling of pipelines with undulating elevation profiles. *Journal of Hydraulic Engineering, 122*(10), 534-539.

Lohrasbi, A., & Attarnejad, R. (2008). Water hammer analysis by characteristic method. *American Journal of Engineering Applied Sciences, 1*(4): 287-294, 2008. ISSN 1941-7020. Retrieved from: https://thescipub.com/pdf/ajeassp.2008.287.294.pdf (accessed November 4, 2020).

Machalinska-Murawska, J., & Szydłowski, M. (2014). Lax-wendroff and mccormack schemes for numerical simulation of unsteady gradually and rapidly varied open channel flow. *Archives of Hydro-Engineering and Environmental Mechanics, 60*(1-4), 51-62.

Malekpour, A., & Karney, B. (2014). Discussion of "pressure surges following sudden air pocket entrapment in storm-water tunnels" by Jose G. Vasconcelos and Gabriel M. Leite. *Journal of Hydraulic Engineering, 140*(4), 1081-1089.

Martin, C. S. (1976). Entrapped air in pipelines. *Proc., 2nd Int. Conf. on Pressure Surges*, 15–27. London, UK: BHRA.

McCorquodale, J., & Hamam, M. (1983). *Modeling surcharged flow in sewers.* Paper presented at the Proc., Int'l Symposium on Urban Hydrology, Hydraulics and Sediment Control, University of Kentucky, Lexington, Kentucky.

MIT OpenCourseWare (2013). *Unsteady Bernoulli Equation*. Retrieved from: https://ocw.mit.edu/courses/mechanical-engineering/2-25-advanced-fluid-mechanics-fall-2013/inviscid-flow-and-bernoulli/MIT2_25F13_Unstea_Bernou.pdf (accessed February 6, 2021)

Montes, J. (1992). A potential flow solution for the free overfall. *Proceedings of the Institution of Civil Engineers-Water Maritime Energy, 96*(4), 259-266.

Montes, J. (1997). Transition to a free-surface flow at end of a horizontal conduit. *Journal of Hydraulic Research, 35*(2), 225-241.

Nicolet, C. (2007). *Hydroacoustic modelling and numerical simulation of unsteady operation of hydroelectric systems.* Thesis. Epfl. Retrieved from: https://www.powervision-eng.ch/Profile/Publications/pdf/EPFL_TH3751.pdf (accessed December 20, 2020).

Pachaly, R. L., Vasconcelos, J. G., Allasia, D. G., Tassi, R., & Bocchi, J. P. P. (2020). Comparing SWMM 5.1 Calculation Alternatives to Represent Unsteady Stormwater Sewer Flows. *Journal of Hydraulic Engineering, 146*(7), 04020046.

Pezzinga, G. (1999). Quasi-2D model for unsteady flow in pipe networks. *Journal of Hydraulic Engineering, 125*(7), 676-685.

Politano, M., Odgaard, A. J., & Klecan, W. (2007). Case study: Numerical evaluation of hydraulic transients in a combined sewer overflow tunnel system. *Journal of Hydraulic Engineering, 133*(10), 1103-1110.

Pozos, O., Gonzalez, C. A., Giesecke, J., Marx, W., & Rodal, E. A. (2010). Air entrapped in gravity pipeline systems. *Journal of Hydraulic Research, 48*(3), 338-347.

Prashanth Reddy, H., Silva-Araya, W. F., & Hanif Chaudhry, M. (2012). Estimation of decay coefficients for unsteady friction for instantaneous, acceleration-based models. *Journal of Hydraulic Engineering, 138*(3), 260-271.

Press, W. H., Teukolsky, S. A., Vetterling, W. T., & Flannery, B. P. (2007). *Numerical recipes 3rd edition: The art of scientific computing*: Cambridge university press.

Ridgway, K., & Kumpula, G. J. (2008). Surge modeling in sewers using alternative hydraulic software Programs. *Journal of Water Management Modeling*. Retrieved from: https://www.chijournal.org/Content/Files/R228-10.pdf (accessed September 12, 2020).

Rokhzadi, A., & Fuamba, M. (2019). A Shock Fitting Approach for Simulating the Surge Caused by Obstruction in a Storm-Water Tunnel. *E-proceedings of the 38th IAHR World Congress*.

Rokhzadi, A., & Fuamba, M. (2020a). The Impacts of Time Integration Schemes on the Pressure Surge Prediction in a Closed Conduit Transient Flow. In *World Environmental and Water Resources Congress 2020: Hydraulics, Waterways, and Water Distribution Systems Analysis* (pp. 225-236). Reston, VA: American Society of Civil Engineers.

Rokhzadi, A., & Fuamba, M. (2020b). Shock-Fitting Approach for Calculating Air Pocket Entrapment Caused by Full Obstruction in Closed Conduit Transient Flow. *Journal of Hydraulic Engineering, 146*(11), 04020078.

Rokhzadi, A., & Fuamba, M. (2021). Investigation of Air Pocket Behavior in Pipelines Using Rigid Column Model and Contributions of Time Integration Schemes. *Water*, 13(6), 785.

Rossman, L., Huber, W. J. V. I. H., Tech. Rep. EPA/600/R-17/111, US EPA Office of Research, & Development, W. S. D., avaialable at: https://nepis. epa. gov/Exe/ZyPDF. cgi. (2016). Storm water management model reference manual.

Rossman, L. A. (2010). *Storm water management model user's manual, version 5.0* (p. 276). Cincinnati: National Risk Management Research Laboratory, Office of Research and Development, US Environmental Protection Agency.

Rossman, L. A., & Huber, W. J. U. E. P. A., II. (2017). *Storm water management model reference manual volume II–hydraulics* (p.*190)*. Retrieved from: https://nepis.epa.gov/Exe/ZyPDF.cgi?Dockey=P100S9AS.pdf (accessed August 7, 2020).

Rossman, L. A., & Supply, W. (2006). *Storm water management model, quality assurance report: dynamic wave flow routing*: US Environmental Protection Agency, Office of Research and Development.

Sanders, B. F., & Bradford, S. F. (2011). Network implementation of the two-component pressure approach for transient flow in storm sewers. *Journal of hydraulic engineering*, 137(2), 158-172.

Schohl, G., & Holly Jr, F. (1991). Cubic-spline interpolation in Lagrangian advection computation. *Journal of Hydraulic Engineering, 117*(2), 248-253.

Seck, A., Fuamba, M., & Kahawita, R. (2017). Finite-volume solutions to the water-hammer equations in conservation form incorporating dynamic friction using the Godunov scheme. *Journal of Hydraulic Engineering, 143*(9), 04017029.

Sibetheros, I., Holley, E., & Branski, J. (1991). Spline interpolations for water hammer analysis. *Journal of Hydraulic Engineering, 117*(10), 1332-1351.

Soares, A. K., Covas, D. I., & Reis, L. F. (2008). Analysis of PVC pipe-wall viscoelasticity during water hammer. *Journal of Hydraulic Engineering, 134*(9), 1389-1394.

Song, C. C., Cardie, J. A., & Leung, K. S. (1983). Transient mixed-flow models for storm sewers. *Journal of hydraulic engineering, 109*(11), 1487-1504.

Trajkovic, B., Ivetic, M., Calomino, F., & D'Ippolito, A. (1999). Investigation of transition from free surface to pressurized flow in a circular pipe. *Water science technology*, *39*(9), 105-112.

Trikha, A. K. (1975). An Efficient Method for Simulating Frequency-Dependent Friction in Transient Liquid Flow. *Journal of Fluids Engineering*, ASME, 97(1): 97–105.

Tsai, T.-L., Yang, J.-C., & Huang, L.-H. (2004). Characteristics method using cubic–spline interpolation for advection–diffusion equation. *Journal of Hydraulic Engineering*, *130*(6), 580-585.

Twyman, J. (2018). Transient flow analysis using the method of characteristics MOC with five-point interpolation scheme. *Obras y Proyectos*, 24, 62-70.

Vardy, A., & Brown, J. (1996). On turbulent, unsteady, smooth-pipe friction. *Paper presented at the BHR group conference series publication.*

Vardy, A., Brown, J., & vibration. (2003). Transient turbulent friction in smooth pipe flows. *Journal of sound*, *259*(5), 1011-1036.

Vasconcelos, J., & Chosie, C. D. (2013). Kinematics of Entrapped Air Pockets Within Stormwater Storage Tunnels. *Journal of Water Management Modeling*. 10:157–175. https://doi.org/10.14796/JWMM.R246-10

Vasconcelos, J. G., & Leite, G. M. (2012). Pressure surges following sudden air pocket entrapment in storm-water tunnels. *Journal of Hydraulic Engineering*, *138*(12), 1081-1089. doi:10.1061/(asce)hy.1943-7900.0000616.

Vasconcelos, J. G., & Wright, S. J. (2003). *Laboratory investigation of surges formed during rapid filling of stormwater storage tunnels.* Paper presented at the Proc., 30th IAHR Congress.

Vasconcelos, J. G., & Wright, S. J. (2004). Numerical Modeling of the Transition between Free Surface and Pressurized Flow in Storm Sewers. *Journal of Water Management Modeling* R220-10. doi: 10.14796/JWMM.R220-10.

Vasconcelos, J. G., & Wright, S. J. (2005). Experimental investigation of surges in a stormwater storage tunnel. *Journal of Hydraulic Engineering*, *131*(10), 853-861. doi:10.1061/(asce)0733-9429(2005)131:10(853).

Vasconcelos, J. G., Wright, S. J., & Roe, P. L. (2006a). Improved simulation of flow regime transition in sewers: Two-component pressure approach. *Journal of Hydraulic Engineering, 132*(6), 553-562.

Vasconcelos, J. G., & Wright, S. J. (2006b). *Mechanisms for air pocket entrapment in stormwater storage tunnels.* Paper presented at the World Environmental and Water Resource Congress 2006: Examining the Confluence of Environmental and Water Concerns.

Vasconcelos, J., Wright, S. J., & Roe, P. L. (2006c). Current Issues on modeling extreme inflows in stormwater systems. *Journal of Water Management Modeling* R225-19. doi: 10.14796/JWMM.R225-19.

Vasconcelos, J., Wright, S., & Roe, P. (2006d). Two-Component Pressure Approach for the simulation of flow regime transition in sewers. *Journal of Hydraulic Engineering*, 553-562.

Vasconcelos, J. G., & Wright, S. J. (2007). Comparison between the two-component pressure approach and current transient flow solvers. *Journal of Hydraulic Research, 45*(2), 178-187.

Vasconcelos, J. G., & Wright, S. J. (2008). Rapid flow startup in filled horizontal pipelines. *Journal of Hydraulic Engineering, 134*(7), 984-992.

Vasconcelos, J. G., & Wright, S. J. (2009). Investigation of rapid filling of poorly ventilated stormwater storage tunnels. *Journal of Hydraulic Research, 47*(5), 547-558.

Vasconcelos, J. G., & Wright, S. J. (2010). Discussion of "Case Study: Numerical Evaluation of Hydraulic Transients in a Combined Sewer Overflow Tunnel System" by M. Politano, AJ Odgaard, and W. Klecan. *Journal of Hydraulic Engineering, 136*(6), 391-391.

Vasconcelos, J. G., & Wright, S. J. (2011a). Geysering generated by large air pockets released through water-filled ventilation shafts. *Journal of Hydraulic Engineering, 137*(5), 543-555.

Vasconcelos, J. G., Wright, S. J., & Lautenbach, D. J. (2011b). *Modeling approaches for the rapid filling of closed conduits with entrapped air.* Paper presented at the World Environmental and Water Resources Congress 2011: Bearing Knowledge for Sustainability.

Wan, W.-y., Zhu, S., Hu, Y.-j., & Mechanics. (2010). Attenuation analysis of hydraulic transients with laminar-turbulent flow alternations. *Applied Mathematics, 31*(10), 1209-1216.

Wang, J., & Vasconcelos, J. G. (2020). Investigation of Manhole Cover Displacement during Rapid Filling of Stormwater Systems. *Journal of Hydraulic Engineering*, *146*(4), 04020022.

Wiggert, D. C. (1972). Transient flow in free-surface, pressurized systems. *Journal of the Hydraulics division*, 98(1), 11-27.

Wright, S. J., Lewis, J. W., & Vasconcelos, J. G. (2009). *Physical processes resulting in geyser formation in rapidly filling stormwater tunnels.* Paper presented at the Proceedings of World Environmental and Water Resources Congress 2009 - World Environmental and Water Resources Congress 2009: Great Rivers, Kansas City, MO, United states.

Wright, S. J., Lewis, J. W., & Vasconcelos, J. G. (2011). Geysering in rapidly filling storm-water tunnels. *Journal of Hydraulic Engineering*, *137*(1), 112-115.

Wright, S. J., Vasconcelos, J. G., Creech, C. T., & Lewis, J. W. (2008). Flow regime transition mechanisms in rapidly filling stormwater storage tunnels. *Environmental fluid mechanics*, *8*(5-6), 605-616.

Wylie, E. B., & Streeter, V. L. (1993). *Fluid transients in systems* (Vol. 1): Prentice Hall Englewood Cliffs, NJ.

Yuan, M. (1984). *Pressurized surges*. MSc thesis. Department of Civil and Mineral Engineering, University of Minnesota, Twin Cities, MN.

Yuce, M. I., & Omer, A. F. (2019). Hydraulic transients in pipelines due to various valve closure schemes. *SN Applied Sciences*, *1*(9), 1110.

Zarzycki, Z. (1994). *Hydraulic Resistance in Unsteady Liquid Flow in Closed Conduits*. Research Reports of Tech. Univ. of Szczecin, No.516, Szczecin in Polish.

Zarzycki, Z. (2000). *On weighting function for wall shear stress during unsteady turbulent pipe flow*. Paper presented at the BHR Group Conference Series Publication.

Zhang, B., Wan, W., & Shi, M. (2018). Experimental and numerical simulation of water hammer in gravitational pipe flow with continuous air entrainment. *Water*, *10*(7), 928.

Zhou, F. (2000). *Effects of trapped air on flow transients in rapidly filling sewers*. PhD thesis. Department of Civil and Environmental Engineering, University of Alberta, Edmonton, CA.

Zhou, F., Hicks, F., & Steffler, P. (2002). Transient flow in a rapidly filling horizontal pipe containing trapped air. *Journal of Hydraulic Engineering*, *128*(6), 625-634.

Zhao, M., & Ghidaoui, M. S. (2004). Godunov-type solutions for water hammer flows. *Journal of Hydraulic Engineering*, 130(4), 341-348.

Zhou, L., Cao, Y., Karney, B., Bergant, A., Tijsseling, A. S., Liu, D., & Wang, P. (2020). Expulsion of Entrapped Air in a Rapidly Filling Horizontal Pipe. *Journal of Hydraulic Engineering*, *146*(7), 04020047.

Zhou, L., Liu, D., Karney, B., & Zhang, Q. (2011). Influence of entrapped air pockets on hydraulic transients in water pipelines. *Journal of Hydraulic Engineering*, *137*(12), 1686-1692.

Zielke, W.: Frequency-dependent friction in transient pipe flow, *Journal of Basics Engineering*, ASME, Vol. 90 (1968), No. 1, 109-115.

Zukoski, E. (1966). Influence of viscosity, surface tension, and inclination angle on motion of long bubbles in closed tubes. *Journal of Fluid Mechanics*, *25*(4), 821-837.

APPENDIX A RIGID COLUMN CODE

1. Main code called : 'RigidColumn_unsteady' :

```
clear all ; clc ; close all;

%%%%%%%%%%%%%%%%%%%% Rigid Column - Unsteady/Additional friction factor
%%%%%%%%%%%%%%%%%%%%

delta_t=0.0001;    % Time step
N=60000;           % Number of terms to calculate

% Initial condition
H_atm=10.33;         % Atmospheric pressure (m)
D=0.10;              % Pipe diameter (m)
Cd=0.4;              % Discharge coefficient
A_orif=0;            % Area of the orifice (m^2)
k=1.4;               % Polytropic coefficient
S_0=0;               % Slope (m/m)
A=pi*(D/2)^2;        % Cross-sectional area (m^2)
L_pipe=4.73;         % Length of the pipe (m)
g=9.81;              % Gravitational acceleration (m/(s^2))
f=0.0269;            % Darcy-Weisbach steady friction factor
K_loss=0;            % Summation of local losses

Q=zeros(N,1);       % Sequence Q_n
Va=zeros(N,1);      % Sequence Va_n
H_air=zeros(N,1);   % Sequence H_n
L_tab=zeros(N,1);   % Sequence H_n

Q_0=0.422*sqrt(g*D^5);      % Initial discharge (m^3/s)
Va_0=1.11*D^3;              % Initial volume (m^3)
%%% The previous formulas come from Hatcher et al. article
% % % % Hatcher, T. M., Malekpour, A., Vasconcelos, J., & Karney, B. (2015).
Comparing unsteady modeling approaches of surges caused by sudden air pocket
compression. Journal of Water Management Modeling.

H_res=0.30;                 % Water level in the reservoir (m)
Q(1)=Q_0;
Va(1)=Va_0;
H_air(1)=H_atm;
L=(L_pipe*A-Va(1))/A;       % Length of the rigid column (m)
L_tab(1)=L;
La=L_pipe-L;               % Length of the air pocket (m)

v_0=Q_0/A;                                  % Initial velocity (m/s)
rho=998;                                    % Water density (kg/(m^3))
dyn_viscosity=10^(-3);                      % Dynamic viscosity (N.s/(m^2))
kin_viscosity=dyn_viscosity/rho;            % Kinematic viscosity (m^2/s)
Re=v_0*D/kin_viscosity;                     % Reynolds number
```

```
Re_c=2320;                                  % Critical Reynolds number
C=13;                                       % Calibration factor
n=0.013;                                    % Manning coefficient
rho_air=1.2;                                % Air density (kg/(m^3))

E=2.5;e=0.007;Ta=273;Kw=2.5;R=8.314459848;rhoa=1.225;Ma=rhoa*Va_0;
a=sqrt(abs(Kw*10^9/rho/(1+(Kw*D/E/e)+(Ma*R*Ta/g/rho/H_atm)*(Kw*10^9/g/rho/H_at
m)-1))); % Speed of pressure wave (m/s)

Air_volume=Va_0/(D^3);
Water_volume=A*L;
Air_mass=Air_volume*rho_air;
Water_mass=Water_volume*rho;

m1=Air_volume/Water_volume;    m2=Air_mass/Water_mass;
time(1)=0;

for i=1:N-1

    time(i+1)=time(i)+delta_t;
    v_i=Q(i)/A;
    Re=v_i*D/kin_viscosity;

%%%%%%%%%%%%%%%%%%%% Variable %%%%%%%%%%%%%%%%%%%%
    Air_volume=Va(i)/(D^3);
    Water_volume=A*L_tab(i);
    Water_mass=Water_volume*rho;
    m1=Air_volume/Water_volume;
    m2=Air_mass/Water_mass;
%%%%%%%%%%%%%%%%%%%% Variable %%%%%%%%%%%%%%%%%%%%

   % % % % unsteadyA : Mixed (Turbulent + Laminar)
   % % % % unsteadyB : Turbulent
   % % % % unsteadyC : Laminar


unsteady_term=unsteadyA(Q(i),C,kin_viscosity,D,a,g,L,n,Re_c,Re,m1,m2,H_res,H_a
tm,rho,rhoa,La);


    K1=g*A/L*(H_res-(H_air(i)-H_atm)+L*S_0-
((f*L/D+K_loss)*Q(i)*abs(Q(i))/(2*g*(A^2))))-unsteady_term;
    K1_p=-Q(i)+Cd*A_orif*sqrt(2*g*(H_air(i)-H_atm));
    H1=H_air(i,1)*(Va(i,1)^k)/((Va(i,1)+K1_p*delta_t)^k);
    L1=Q(i)/A;

unsteady_term=unsteadyA(Q(i)+K1*delta_t/2,C,kin_viscosity,D,a,g,L,n,Re_c,Re,m1
,m2,H_res,H_atm,rho,rhoa,La);


    K2=g*A/L*(H_res-(H1-H_atm)+L*S_0-
((f*L/D+K_loss)*(Q(i)+K1*delta_t/2)*abs(Q(i)+K1*delta_t/2)/(2*g*(A^2))))-
unsteady_term;
    K2_p=-(Q(i)+K1*delta_t/2)+Cd*A_orif*sqrt(2*g*(H1-H_atm));
```

```
    H2=H_air(i,1)*(Va(i,1)^k)/((Va(i,1)+K2_p*delta_t/2)^k);
    L2=(Q(i)+L1*delta_t/2)/A;

unsteady_term=unsteadyA(Q(i)+K2*delta_t/2,C,kin_viscosity,D,a,g,L,n,Re_c,Re,m1
,m2,H_res,H_atm,rho,rhoa,La);


    K3=g*A/L*(H_res-(H2-H_atm)+L*S_0-
((f*L/D+K_loss)*(Q(i)+K2*delta_t/2)*abs(Q(i)+K2*delta_t/2)/(2*g*(A^2))))-
unsteady_term;
    K3_p=-(Q(i)+K2*delta_t/2)+Cd*A_orif*sqrt(2*g*(H_air(i)-H_atm));
    H3=H_air(i,1)*(Va(i,1)^k)/((Va(i,1)+K3_p*delta_t/2)^k);
    L3=(Q(i)+L2*delta_t/2)/A;

unsteady_term=unsteadyA(Q(i)+K3*delta_t,C,kin_viscosity,D,a,g,L,n,Re_c,Re,m1,m
2,H_res,H_atm,rho,rhoa,La);


    K4=g*A/L*(H_res-(H3-H_atm)+L*S_0-
((f*L/D+K_loss)*(Q(i)+K3*delta_t)*abs(Q(i)+K3*delta_t)/(2*g*(A^2))))-
unsteady_term;
    K4_p=-(Q(i)+K3*delta_t)+Cd*A_orif*sqrt(2*g*(H_air(i)-H_atm));
    L4=(Q(i)+L3*delta_t)/A;

    Q(i+1,1)=Q(i,1)+(delta_t/6)*(K1+2*K2+2*K3+K4);
    Va(i+1,1)=Va(i,1)+(delta_t/6)*(K1_p+2*K2_p+2*K3_p+K4_p);
    H_air(i+1,1)=H_air(i,1)*(Va(i,1)^k)/(Va(i+1,1)^k);
    L_tab(i+1,1)=L+(delta_t/6)*(L1+2*L2+2*L3+L4);

end

t=(i-1)*delta_t;
T=[0:delta_t:t+delta_t];
figure(2)
plot(T,Q);

xlabel('Time t (s)');
ylabel('Discharge Q (m^3/s)') ;
title('Rigid Column - Runge-Kutta 4th order');
[Hp,Hv,index1]=Square_residuals((H_air-H_atm),N,H_res);

figure(3)
plot(T,(H_air-H_atm));
xlabel('Time t (s)')
ylabel('Relative air pressure Hair (m)')
title('Rigid Column - Runge-Kutta 4th order');

figure(4)
plot(T,Va);
xlabel('Time t (s)')
ylabel('Va (m^3)')
title('Rigid Column - Runge-Kutta 4th order');
```

2. Function called : 'unsteadyA' (Mixed) :

```
function
unsteady_term=unsteadyA(Q,C,kin_viscosity,D,a,g,L,n,Re_c,Re,m1,m2,H_res,H_atm,
rho,rhoa,La)
%%%%%%%%%%%% Mixed flow (Laminar+Turbulent) %%%%%%%%%%%%%%
v = abs(Q/(pi*(D^2)/4));
Rp=D/4;
A=pi*(D^2)/4;
if v~=0
       if Re>Re_c
unsteady_term=abs(8*g*(n^2)/((Rp)^(1/3)))*(C*10^3)*((H_res+H_atm)/H_atm)*(rhoa
/rho)*(La/L)*(a/sqrt(g*D))*L/D*(g*A/L)*Q*abs(Q)/(2*g*(A^2));
       else
unsteady_term=abs(64*(kin_viscosity)/(v*D))*(C*10^3)*((H_res+H_atm)/H_atm)*(rh
oa/rho)*(La/L)*(a/sqrt(g*D))*L/D*(g*A/L)*Q*abs(Q)/(2*g*(A^2));
       end

else
    unsteady_term=0;
end
end
```

3. Function called : 'unsteadyB' (Turbulent) :

```
function
unsteady_term=unsteadyB(Q,C,kin_viscosity,D,a,g,L,n,Re_c,Re,m1,m2,H_res,H_atm,
rho,rhoa,La)
%%%%%%%%%%%% Turbulent %%%%%%%%%%%%%%
v = abs(Q/(pi*(D^2)/4));
Rp=D/4;
A=pi*(D^2)/4;
if v~=0
unsteady_term=abs(8*g*(n^2)/((Rp)^(1/3)))*(C*10^3)*((H_res+H_atm)/H_atm)*(rhoa
/rho)*(La/L)*(a/sqrt(g*D))*L/D*(g*A/L)*Q*abs(Q)/(2*g*(A^2));
else
    unsteady_term=0;
end
end
```

4. Function called : 'unsteadyC' (Laminar) :

```
function
unsteady_term=unsteadyC(Q,C,kin_viscosity,D,a,g,L,n,Re_c,Re,m1,m2,H_res,H_atm,
rho,rhoa,La)
%%%%%%%%%%%% Laminar %%%%%%%%%%%%%%
v = abs(Q/(pi*(D^2)/4));
Rp=D/4;
A=pi*(D^2)/4;
```

```
if v~=0
unsteady_term=abs(64*(kin_viscosity)/(v*D))*(C*10^3)*((H_res+H_atm)/H_atm)*(rh
oa/rho)*(La/L)*(a/sqrt(g*D))*L/D*(g*A/L)*Q*abs(Q)/(2*g*(A^2));
else
    unsteady_term=0;
end
end
```

APPENDIX B METHOD OF CHARACTERISTICS CODE (MATLAB)

1. Main code called : 'MOC_unsteady' :

```
clear all; clc; close all;

imax=20;                    % Number of grid points
nnmax=16000;                % Number of terms to calculate
t(1)=0;
CFL=0.4;                    % Courant number
k=1.4;                      % Polytropic coefficient
g=9.81;                     % Gravitational acceleration (m/s)
nu=1e-6;                    % Kinematic viscosity (m^2/s)
D=0.10;                     % Diameter of the pipe (m)
A=pi/4*D^2;                 % Cross-sectional area of the pipe (m^2)

Q_0=0.423*sqrt(g*D^5);      % Initial discharge (m^3/s)
Va_0=1.05*D^3;              % Initial volume (m^3)

Van=Va_0;Va=Va_0;
Q=Q_0;
Hatm=10.33;                 % Atmospheric pressure (m)
ha=Hatm;han=ha;
Kloss=0;                    % Summation of local losses
f=0.0269;                   % Darcy-Weisbach steady friction factor
S0=0;                       % Slope of the pipe (m/m)
Lt=4.73;                    % Length of the pipe (m)
Lu=(A*Lt-Va)/A;Lun=Lu;      % Length of the rigid column (m)
La=Lt-Lu;                   % Length of the air pocket (m)
xmax=Lu;xmin=0;
dx=(xmax-xmin)/(imax-1);
Hres=0.30;                  % Water level in the reservoir (m)

%%%%% Initial conditons %%%%%
for i=1:imax
v(i)=Q/A;
h(i)=Hres+Hatm;
end
hn=h;vn=v;


H=zeros(imax,nnmax);   V=zeros(imax,nnmax);   Q=zeros(imax,nnmax);
H(:,1)=h;   V(:,1)=v;   Q(:,1)=V(:,1)*A;

v_0=Q_0/A;                                    % Initial velocity (m/s)
rhow=998;                                     % Water density (kg/(m^3))
dyn_viscosity=10^(-3);                        % Dynamic viscosity (N.s/(m^2))
kin_viscosity=dyn_viscosity/rhow;             % Kinematic viscosity (m^2/s)
Re=v_0*D/kin_viscosity;                       % Reynolds number
Re_c=2320;                                    % Critical Reynolds number
C=13;                                         % Calibration factor
n=0.013;                                      % Manning coefficient
rho_air=1.2;                                  % Air density (kg/(m^3))
```

```
E=2.5;e=0.007;Ta=273;Kw=2.5;R=8.314459848;rhoa=1.225;Ma=rhoa*Va;
a=sqrt(abs(Kw*10^9/rhow/(1+(Kw*D/E/e)+(Ma*R*Ta/g/rhow/ha)*(Kw*10^9/g/rhow/ha)-
1)));

Air_volume=Va_0/(D^3);
Water_volume=A*Lt;
Air_mass=Air_volume*rhoa;
Water_mass=Water_volume*rhow;

m1=Air_volume/Water_volume;   m2=Air_mass/Water_mass;

for nn=2:nnmax

   % % % % unsteadyA : Mixed (Turbulent + Laminar)
   % % % % unsteadyB : Turbulent
   % % % % unsteadyC : Laminar

dt=CFL*dx/(abs(a)+max(abs(vn)));

t(nn)=t(nn-1)+dt;

hn(1)=(Hres+Hatm)-(1+Kloss)*vn(1)*abs(vn(1))/2/g;

vs=v(1)+CFL*(v(2)-v(1));
hs=h(1)+CFL*(h(2)-h(1));

v_i=vs;
Re=v_i*D/kin_viscosity;

f_prime=unsteadyA(v_i,C,kin_viscosity,D,a,g,Lt,n,Re_c,Re,m1,m2,Hres,Hatm,rhow,
rhoa,La);

Sfs=(f+f_prime)/(2*D*g)*vs*abs(vs);
Dn=vs-g/a*hs+g*(S0-Sfs)*dt;
vn(1)=g*hn(1)/a+Dn;

H(1,nn)=hn(1);
V(1,nn)=vn(1);
Q(1,nn)=V(1,nn)*A;

for i=2:imax-1

vs=v(i)+CFL*(v(i+1)-v(i));
hs=h(i)+CFL*(h(i+1)-h(i));

v_i=vs;
Re=v_i*D/kin_viscosity;

f_prime=unsteadyA(v_i,C,kin_viscosity,D,a,g,Lt,n,Re_c,Re,m1,m2)
,Hres,Hatm,rhow,rhoa,La);

Sfs=(f+f_prime)/(2*D*g)*vs*abs(vs);
```

```
Dn=vs-g/a*hs+g*(S0-Sfs)*dt;

vr=v(i)+CFL*(v(i-1)-v(i));
hr=h(i)+CFL*(h(i-1)-h(i));

v_i=vr;
Re=v_i*D/kin_viscosity;

f_prime=unsteadyA(v_i,C,kin_viscosity,D,a,g,Lt,n,Re_c,Re,m1,m2,Hres,Hatm,rhow,
rhoa,La);

Sfr=(f+f_prime)/(2*D*g)*vr*abs(vr);
Dq=vr+g/a*hr+g*(S0-Sfr)*dt;

hn(i)=(Dq-Dn)/(2*g/a);
vn(i)=Dn+g/a*hn(i);
H(i,nn)=hn(i);    V(i,nn)=vn(i);    Q(i,nn)=V(i,nn)*A;

end

vr=v(imax)+CFL*(v(imax-1)-v(imax));
hr=h(imax)+CFL*(h(imax-1)-h(imax));

v_i=vr;
Re=v_i*D/kin_viscosity;

f_prime=unsteadyA(v_i,C,kin_viscosity,D,a,g,Lt,n,Re_c,Re,m1,m2,Hres,Hatm,rhow,
rhoa,La);

Sfr=(f+f_prime)/(2*D*g)*vr*abs(vr);
Dq=vr+g/a*hr+g*(S0-Sfr)*dt;

vn(imax)=Dq-g/a*hn(imax);
Van=Va+dt*(-A*v(imax));
han=ha*(abs(Va))^k*(abs(Van))^-k;
hn(imax)=han-vn(imax)*abs(vn(imax))/2/g;
Lun=Lu+dt*(vn(imax));

H(imax,nn)=han;      V(imax,nn)=vn(imax);     Q(imax,nn)=V(imax,nn)*A;
ha=han; Va=Van; h=hn; v=vn; Lu=Lun;

end

for j=1:nnmax
    H_relative(:,j)=H(:,j)-Hatm;
end

figure(5)
plot(t,Q(imax,:));
xlabel('Time t (s)')
ylabel('Discharge Q (m3/s)')
title('Water hammer equations MOC')

figure(6)
```

```
plot(t, H_relative(imax,:));
xlabel('Time t (s)')
ylabel('Relative air pressure (Hair-Hatm) (m)')
title('Water hammer equations MOC')
```

2. Function called : 'unsteadyA' (Mixed) :

```
function
f_prime=unsteadyA(v,C,kin_viscosity,D,a,g,L,n,Re_c,Re,m1,m2,Hres,Hatm,rhow,rho
a,La)

%%%%%%%%% Mixed flow (Turbulent+Laminar)%%%%%%%%%
Rp=D/4;
A=pi*(D^2)/4;
if v~=0
       if Re>Re_c
          lambda=abs(8*g*(n^2)/((Rp)^(1/3)));
       else
          lambda=abs(64*(kin_viscosity)/(v*D));
       end
 f_prime=(C*10^3)*((Hres+Hatm)/Hatm)*(rhoa/rhow)*(La/L)*(a/sqrt(g*D))*lambda;

else
    f_prime=0;
end
end
```

3. Function called : 'unsteadyB' (Turbulent) :

```
Function
f_prime=unsteadyB(v,C,kin_viscosity,D,a,g,L,n,Re_c,Re,m1,m2,Hres,Hatm,rhow,rho
a,La)

%%%%%%%%% Turbulent %%%%%%%%%
Rp=D/4;
A=pi*(D^2)/4;
if v~=0
      lambda=abs(8*g*(n^2)/((Rp)^(1/3)));
 f_prime=(C*10^3)*((Hres+Hatm)/Hatm)*(rhoa/rhow)*(La/L)*(a/sqrt(g*D))*lambda;

else
    f_prime=0;
end
end
```

4. **Function called : 'unsteadyC' (Laminar) :**

```
function
f_prime=unsteadyC(v,C,kin_viscosity,D,a,g,L,n,Re_c,Re,m1,m2,Hres,Hatm,rhow,rho
a,La)

%%%%%%%%% Laminar %%%%%%%%%
Rp=D/4;
A=pi*(D^2)/4;
if v~=0
      lambda=abs(64*(kin_viscosity)/(v*D));
f_prime=(C*10^3)*((Hres+Hatm)/Hatm)*(rhoa/rhow)*(La/L)*(a/sqrt(g*D))*lambda;

else
    f_prime=0;
end
end
```

APPENDIX C SHOCK-FITTING CODE (MATLAB)

1. Main code called : 'Main' :

```
clear all; clc; close all;

global D g A S0 f n

Hatm=10.33;                     % Atmospheric pressure
Hres=0.204;                     % Relative pressure at the upstream reservoir
D=0.053;                        % Diameter
k=1.2;                          % Polytropic coefficient
S0=-0.02;                       % Slope
A=pi*(D/2)^2;                   % Pipe area
Lt=10.7;                        % Length of the pipe
g=9.81;                         % Gravitational acceleration
f=0.025;                        % Darcy-Weisbach friction factor
n=0.009;                        % Manning coefficient
Kloss=2.9;                      % Coefficient of singular head loss
a=1200;                         % Elastic wave speed
rho=998;                        % Density

delta=1e-16;

% Initial conditions
Q_0=0.15*sqrt(g*D^5);          % Initial discharge from Hatcher article
Va_0=2.63*D^3;                 % Initial air pocket volume from Hatcher article

v_0=Q_0/A;                     % Initial velocity
ha=0;                          % Initial air pocket pressure

y_0=0.5628*D;                  % Initial height of the free surface region
teta=2.0*acos((D/2-y_0)/(D/2));
At=((D^2)/8)*(abs(teta)-sin(abs(teta)));
Lu=(Lt*(A-At)-Va_0)/(A-At);          % Length of the pressurized zone


% Free surface flow (at the right of the interface)
imax=20;    xmin=Lu;    xmax=Lt;    dx=(xmax-xmin)/(imax-1);
x(1)=xmin+(1/2)*dx;    x(imax)=xmax;

for i=2:imax-1
x(i)=x(i-1)+dx;
end

for i=1:imax
y(i)=0.5628*D;
teta=2*acos((D/2-y(i))/(D/2));
AF(i)=((D^2)/8)*(abs(teta)-sin(abs(teta)));
c(i)=sqrt(g*D/8)*sqrt((abs(teta)-sin(abs(teta)))/sin(abs(teta)/2));
v(i)=Q_0/AF(i);
```

```
end

% Pressurized flow (at the left of the interface)
xxmin=0;    xxmax=Lu;    dxx=dx;    iimax=1+round((xxmax-xxmin)/dxx);
xx(1)=xxmin;    xx(iimax)=xxmax-(1/2)*dxx;

for i=2:iimax-1
xx(i)=xx(i-1)+dxx;
end

for i=1:iimax
hu(i)=Hres-(1+Kloss)*v_0*abs(v_0)/2/g;
vu(i)=Q_0/A;
end

Q33(1)=vu(iimax)*A;
vp1=v(1);    yp1=y(1);    cp1=c(1);    vp2=vu(iimax);    hp2=hu(iimax);    wu=0;

hu0=Hres-(1+Kloss)*v_0*abs(v_0)/2/g;
Va=Va_0;    hap(1)=ha;    Vap(1)=Va_0;    wup(1)=0;    hup(1)=hu(iimax);

nnmax=300000;   CFL=0.9;    t(1)=0;

for nn=2:nnmax

    nn
    dt1=CFL*dxx/(max(abs(vu))+a);
    dt2=CFL*dx/(max(abs(v))+max(c));

    dt1=min(dt1,dt2);
    dt0=dx/abs(wu);

    dtP=min(dt0,dt1);
    dtF=dtP;

    t(nn)=t(nn-1)+dtP;

    vr=v(1)+CFL*(vp1-v(1));
    yr=y(1)+CFL*(yp1-y(1));
    cr=c(1)+CFL*(cp1-c(1));

    teta=2*acos((D/2-yr)/(D/2));
    At=((D^2)/8)*abs((abs(teta)-sin(abs(teta))));
    Pt=abs(teta)*(D/2);


    Rr=abs(At/(abs(Pt)+delta));
    Sfr=abs(((n^2)*(vr^2))/(Rr^(4/3)));
    Dq=vr+(g/cr)*yr+g*(S0-Sfr)*dtF;

    vs=v(1)+CFL*(v(2)-v(1));
    ys=y(1)+CFL*(y(2)-y(1));
    cs=c(1)+CFL*(c(2)-c(1));
```

```
teta=2*acos((D/2-ys)/(D/2));
At=((D^2)/8)*(abs(teta)-sin(abs(teta)));
Pt=abs(teta)*(D/2);

Rs=abs(At/(abs(Pt)+delta));
Sfs=abs(((n^2)*(vs^2))/(Rs^(4/3)));
Dn=vs-(g/cs)*ys+g*(S0-Sfs)*dtF;

yn(1)=(Dq-Dn)/(g/cr+g/cs);
vn(1)=Dn+g/cs*yn(1);


for i=2:imax-1
    vr=v(i)+CFL*(v(i-1)-v(i));
    yr=y(i)+CFL*(y(i-1)-y(i));
    cr=c(i)+CFL*(c(i-1)-c(i));

    teta=2*acos((D/2-yr)/(D/2));
    At=((D^2)/8)*(abs(teta)-sin(abs(teta)));
    Pt=abs(teta)*(D/2);

    Rr=abs(At/(abs(Pt)+delta));
    Sfr=abs(((n^2)*(vr^2))/(Rr^(4/3)));
    Dq=vr+(g/cr)*yr+g*(S0-Sfr)*dtF;

    vs=v(i)+CFL*(v(i+1)-v(i));
    ys=y(i)+CFL*(y(i+1)-y(i));
    cs=c(i)+CFL*(c(i+1)-c(i));

    teta=2*acos((D/2-ys)/(D/2));
    At=((D^2)/8)*(abs(teta)-sin(abs(teta)));
    Pt=abs(teta)*(D/2);

    Rs=abs(At/(abs(Pt)+delta));
    Sfs=abs(((n^2)*(vs^2))/(Rs^(4/3)));
    Dn=vs-(g/cs)*ys+g*(S0-Sfs)*dtF;

    yn(i)=(Dq-Dn)/(g/cr+g/cs);
    vn(i)=Dn+g/cs*yn(i);
end

vr=v(imax)+CFL*(v(imax-1)-v(imax));
yr=y(imax)+CFL*(y(imax-1)-y(imax));
cr=c(imax)+CFL*(c(imax-1)-c(imax));

teta=2*acos((D/2-yr)/(D/2));
At=((D^2)/8)*(abs(teta)-sin(abs(teta)));
Pt=abs(teta)*(D/2);

Rr=abs(At/(abs(Pt)+delta));
Sfr=abs(((n^2)*(vr^2))/(Rr^(4/3)));
Dq=vr+(g/cr)*yr+g*(S0-Sfr)*dtF;
```

```
vn(imax)=0;
yn(imax)=(Dq-vn(imax))/(g/cr);

% Pressurized region
vs=vu(1)+CFL*(vu(2)-vu(1));
hs=hu(1)+CFL*(hu(2)-hu(1));

Sfs=f/(2*D)*vs*abs(vs);
Dn=vs-(g/a)*ys+g*(S0-Sfs)*dtP;
hun(1)=hu0-vu(1)^2/2/g-Kloss*abs(vu(1))*vu(1)/2/g;
vun(1)=(g/a)*hun(1)+Dn;

for i=2:iimax-1
    vr=vu(i)+CFL*(vu(i-1)-vu(i));
    hr=hu(i)+CFL*(hu(i-1)-hu(i));
    Sfr=f/2/D*vr*abs(vr);
    Dq=vr+(g/a)*hr+g*(S0-Sfr)*dtP;

    vs=vu(i)+CFL*(vu(i+1)-vu(i));
    hs=hu(i)+CFL*(hu(i+1)-hu(i));
    Sfs=f/2/D*vs*abs(vs);
    Dn=vs-g/a*hs+g*(S0-Sfs)*dtP;

    hun(i)=(Dq-Dn)/(2*g/a);
    vun(i)=Dn+g/a*hun(i);
end

vr=vu(iimax)+CFL*(vu(iimax-1)-vu(iimax));
hr=hu(iimax)+CFL*(hu(iimax-1)-hu(iimax));
Sfr=f/(2*D)*vr*abs(vr);
Dq=vr+(g/a)*hr+g*(S0-Sfr)*dtP;

vs=vu(iimax)+CFL*(vp2-vu(iimax));
hs=hu(iimax)+CFL*(hp2-hu(iimax));
Sfs=f/(2*D)*vs*abs(vs);
Dn=vs-g/a*hs+g*(S0-Sfs)*dtP;

hun(iimax)=(Dq-Dn)/(2*g/a);
vun(iimax)=Dn+g/a*hun(iimax);


%%%%%%%%%%%%%%%End pressurized flows%%%%%%%%%%%%%%%%%%%%%%%%%%%%%%%%%%%%
% %%%%%%%%%%%%%%%Air Volume & Pressure%%%%%%%%%%%%%%%%%%%%%%%%%%%%%%%%%%%
Van=Va-dtP*A*vun(iimax);
han=-Hatm+(ha+Hatm)*((abs(Va))^k)*((abs(Van))^(-k));
%%%%%%%%%%%%%%%End Air Volume and Pressure%%%%%%%%%%%%%%%%%%%%%%%%%%%%%%%
Va=Van;
ha=han;
vu=vun;
hu=hun;
v=vn;
y=yn;

for i=1:imax
teta=2.0*acos((D/2-y(i))/(D/2));
```

```
    AF(i)=((D^2)/8)*(abs(teta)-sin(abs(teta)));
    c(i)=sqrt(g*D/8)*sqrt(abs((abs(teta)-sin(abs(teta))))/sin(abs(teta)/2));
    Ap(i)=(rho*g/12)*((3*D^2-4*D*y(i)+4*y(i)^2)*sqrt(abs(y(i)*(D-y(i))))-
3*(D^2)*(D-2*y(i))*atan(sqrt(abs(y(i)/(D-y(i))))));

    end

 [vp1,yp1,cp1,hp2,vp2,wun]=Tran(vu,hu,iimax,y,v,c,wu,ha,rho,a,dtF,dtP);
 Length(nn)=Length(nn-1)+wu*dtF;

if(Length(nn)>x(1))
    iimax=iimax+1;   imax=imax-1;

    hu1=hu;vu1=vu;x1=x;
    xx(iimax)=xx(iimax-1)+dx;
    for i=1:imax
       x(i)=x1(i)+dx;
    end
    for i=1:iimax-1
        hu(i+1)=hu1(i);
        vu(i+1)=vu1(i);
    end
    hu(1)=hu(2);
    vu(1)=vu(2);
end

if(Length(nn)<xx(iimax))
    iimax=iimax-1;
    imax=imax+1;
    hu1=hu;vu1=vu;x1=x;
    xx(iimax)=xx(iimax-1)-dx;

    x(imax)=x1(imax-1);
    for i=1:imax-1
       x(i)=x1(i)-dx;
    end

    for i=1:iimax
        hu(i)=hu1(i+1);
        vu(i)=vu1(i+1);
    end

    y(imax)=y(imax-1);   AF(imax)=AF(imax-1);   c(imax)=c(imax-1);
v(imax)=v(imax-1);   Ap(imax)=Ap(imax-1);

end

   wu=wun;
   wup(nn)=wu;
   hap(nn)=ha;hup(nn)=hu(iimax);
   Vap(nn)=Va;
   Q33(nn)=vu(iimax)*A;
```

```
 if (mod(nn,1000)==0 )
        nn

        figure(2)
        plot(t/(Va_0^(1/3)/sqrt(g*D)),hup/D);
        ylabel('(Hair-Hatm)/D');xlabel('Time t*')
        title('Hatcher et al. - Shock-fitting')

        figure(3)
        plot(t/((Van)^(1/3)/sqrt(g*D)),Q33/sqrt(g*D^5),'-k');
        ylabel('Dimensionless discharge Q*');xlabel('Time t*')
        title('Hatcher et al. - Shock-fitting')

        figure(5)
        plot(xx(1:iimax),hu(1:iimax),'-o');
        ylabel('Pressure of the pressurized zone hu')
        xlabel('x')

        figure(7)
        plot(x(1:imax),y(1:imax)/D,'-o');
        ylabel('Depth of the free surface zone y')
        xlabel('x')

        figure(8)
        plot(t/((Van)^(1/3)/sqrt(g*D)),wup,'-k');
        ylabel('wu');xlabel('T*')

        figure(9)
        plot(t,Length)
        ylabel('Lu');xlabel('T*')

        pause(0.05)
 end

end
```

2. Function called : 'Tran' :

```
function [vp1,yp1,cp1,hp2,vp2,wun]=Tran(vu,hu,iimax,y,v,c,wu,ha,rho,a,dtF,dtP)
D=0.053;
if(wu>0)
[vp2,hp2,wun]=flxT4(y,v,vu,hu,ha,iimax,wu,rho,a,c,dtF,dtP);
vp1=v(1);    yp1=y(1);    cp1=c(1);
end

if(wu<=0)
[vp1,yp1,vp2,hp2,cp1,wun]=flxT1(ha,iimax,vu,hu,y,v,rho,a,c,dtF,dtP);
end

end
```

3. Function called : 'flxT1' :

```
function [vp1,yp1,vp2,hp2,cp1,wun]=flxT1(ha,iimax,vu,hu,y,v,rho,a,c,dtF,dtP)
global D g A S0 f n

tol=1e-16;delta=1e-16;

teta=2*acos((D/2-y(1))/(D/2));
AF(1)=((D^2)/8)*(abs(teta)-sin(abs(teta)));
Ap(1)=(rho*g/12)*((3*D^2-4*D*y(1)+4*y(1)^2)*sqrt(abs(y(1)*(D-y(1))))-
3*(D^2)*(D-2*y(1))*atan(sqrt(abs(y(1)/(D-y(1))))));

resv1=10.0;resy1=10.0;resv2=10.0;resh2=10.0;resc1=10.0;rest=10.0;resAp=10.0;
resA=10.0;

vp1=v(1)+tol;yp1=y(1)+tol;cp1=c(1)+tol;App1=Ap(1)+tol;Ap1=AF(1)+tol;
vp2=vu(iimax)+tol;hp2=hu(iimax)+tol;teta=3.0;

wun=(A*vu(iimax)-AF(1)*v(1))/(A-AF(1));

kk=1;

while((resv1>tol || resy1>tol || resv2>tol || resh2>tol || resc1>tol ||
rest>tol || resAp>tol || resA>tol) && (kk<3000))

kk=kk+1;

G1=0.5*sqrt(g*D/8)/sqrt((abs(teta)-sin(abs(teta)))/sin(abs(teta)/2))*((1-
cos(abs(teta)))*sin(abs(teta)/2)-0.5*cos(abs(teta)/2)*(abs(teta)-
sin(abs(teta))))/(sin(abs(teta)/2))^2;
G2=(rho*g/12)*((-4*D+8*yp1)*sqrt(abs(yp1*(D-yp1)))+(3*D^2-
4*D*yp1+4*(yp1^2))*(abs(D-2*yp1))/(2*sqrt(abs(yp1*(D-
yp1))))+6*(D^2)*atan(sqrt(abs(yp1/(D-yp1))))-3*(D^2)*(abs((D-
2*yp1))/D)*(sqrt(abs(D-yp1))/(2*sqrt(yp1))+sqrt(yp1)/(2*sqrt(abs(D-yp1)))));

Pt=abs(teta)*(D/2);
Rs=abs(Ap1/(abs(Pt)+delta));

Sf1=abs(((n^2)*(v(1)^2))/(Rs^(4/3)));
Sf2=f/(2*D)*vu(iimax)*abs(vu(iimax));

J=[1 g/a 0 0 0 0 0 0;
   0 0 1 -g/cp1 g*yp1/(cp1^2) 0 0 0;
   A 0 -Ap1 0 0 0 0 -vp1+wun
   -rho*A*(vp1-vp2)+rho*A*vp2-wun*rho*A rho*g*A -rho*A*vp2+wun*rho*A 0 0 0 -1 0;
   0 0 0 0 -1 G1 0 0;
   0 0 0 -1 0 (D/4)*sin(abs(teta)/2) 0 0;
   0 0 0 G2 0 0 -1 0;
   0 0 0 0 0 D^2/8.0*(1-cos(abs(teta))) 0 -1];

ff=[vp2-vu(iimax)+(g/a)*hp2-(g/a)*hu(iimax)+g*dtP*(Sf2-S0);
    vp1-v(1)-(g/cp1)*yp1+(g/c(1))*y(1)+g*dtF*(Sf1-S0);
    A*vp2-Ap1*vp1-wun*(A-Ap1);
    rho*g*(hp2-0.5*D)*A-App1-rho*g*A*ha-rho*vp2*A*(vp1-vp2)+rho*wun*A*(vp1-
vp2);
```

```
    -cp1+sqrt(g*D/8)*sqrt((abs(teta)-sin(abs(teta)))/sin(abs(teta)/2));
    -yp1+(D/2)*(1-cos(abs(teta)/2));
    -App1+(rho*g/12)*((3*D^2-4*D*yp1+4*yp1^2)*sqrt(yp1*(D-yp1))-3*(D^2)*(D-
2*yp1)*atan(sqrt(yp1/(D-yp1))));
    -Ap1+((D^2)/8)*(abs(teta)-sin(abs(teta)))];

vp2m=vp2;    hp2m=hp2;    vp1m=vp1;    yp1m=yp1;    cp1m=cp1;    tetam=teta;
App1m=App1;    Am=Ap1;

df=J\ff;

vp2=vp2-df(1);
hp2=hp2-df(2);
vp1=vp1-df(3);
yp1=yp1-df(4);
cp1=cp1-df(5);
teta=teta-df(6);
App1=App1-df(7);
Ap1=Ap1-df(8);

resv2=abs(vp2m-vp2);
resh2=abs(hp2m-hp2);
resv1=abs(vp1-vp1m);
resy1=abs(yp1-yp1m);
resc1=abs(cp1m-cp1);
rest=abs(tetam-teta);
resAp=abs(App1m-App1);
resA=abs(Am-Ap1);
end

if (~isreal(vp2) || ~isreal(hp2) || ~isreal(vp1) || ~isreal(yp1) ||
~isreal(cp1) || ~isreal(teta) || ~isreal(App1) || ~isreal(App1))

tol=1e-16;
teta=2*acos((D/2-y(1))/(D/2));
AF(1)=((D^2)/8)*(abs(teta)-sin(abs(teta)));
Ap(1)=(rho*g/12)*((3*D^2-4*D*y(1)+4*y(1)^2)*sqrt(abs(y(1)*(D-y(1))))-
3*(D^2)*(D-2*y(1))*atan(sqrt(abs(y(1)/(D-y(1))))));

resv1=10.0;resy1=10.0;resv2=10.0;resh2=10.0;resc1=10.0;rest=10.0;resAp=10.0;re
sA=10.0;

vp1=v(1)+tol;yp1=y(1)+tol;cp1=c(1)+tol;App1=Ap(1)+tol;Ap1=AF(1)+tol;
vp2=vu(iimax)+tol;hp2=hu(iimax)+tol;teta=3.0;

wun=(A*vu(iimax)-AF(1)*v(1))/(A-AF(1));
Pt=abs(teta)*(D/2);
Rs=abs(Ap1/(abs(Pt)+delta));

Sf1=abs(((n^2)*(v(1)^2))/(Rs^(4/3)));
Sf2=f/(2*D)*vu(iimax)*abs(vu(iimax));

F=@(x) [x(1)-vu(iimax)+(g/a)*x(2)-(g/a)*hu(iimax)+g*dtP*(Sf2-S0);
    x(3)-v(1)-(g/cp1)*x(4)+(g/c(1))*y(1)+g*dtF*(Sf1-S0);
    A*x(1)-Ap1*x(3)-wun*(A-Ap1);
```

```
    rho*g*(x(2)-0.5*D)*A-x(7)-rho*g*A*ha-rho*x(1)*A*(x(3)-
x(1))+rho*wun*A*(x(3)-x(1));
    -x(5)+sqrt(g*D/8)*sqrt((abs(x(6))-sin(abs(x(6))))/sin(abs(x(6))/2));
    -x(4)+(D/2)*(1-cos(abs(x(6))/2));
    -x(7)+(rho*g/12)*((3*D^2-4*D*x(4)+4*x(4)^2)*sqrt(x(4)*(D-x(4)))-
3*(D^2)*(D-2*x(4))*atan(sqrt(x(4)/(D-x(4)))));
    -x(8)+((D^2)/8)*(abs(x(6))-sin(abs(x(6))))];

x0=[vp2;hp2;vp1;yp1;cp1;teta;App1;Ap1];
[x] = fsolve(F,x0)
end

end
```

4. Function called : 'flxT1' :

```
function [vp2,hp2,wun]=flxT4(y,v,vu,hu,ha,iimax,wu,rho,a,c,dtF,dtP)

global D g A S0 f n

tol=1e-16;
resv=10.0;resh=10.0;resw=10.0;
vp2=vu(iimax)+tol;   hp2=hu(iimax)+tol;   wun=wu+tol;kk=1;

teta=2*acos((D/2-y(1))/(D/2));
AF(1)=((D^2)/8)*(abs(teta)-sin(abs(teta)));
Ap(1)=(rho*g/12)*((3*D^2-4*D*y(1)+4*y(1)^2)*sqrt(abs(y(1)*(D-y(1))))-
3*(D^2)*(D-2*y(1))*atan(sqrt(abs(y(1)/(D-y(1))))));

while((resv>tol || resh>tol || resw>tol) && (kk<1000))
kk=kk+1;
Sf2=f/(2*D)*vu(iimax)*abs(vu(iimax));

J=[1 g/a 0;
   A 0 -(A-AF(1));
   rho*A*v(1)-wun*rho*A rho*g*A rho*A*(v(1)-vp2)];

ff=[vp2+g/a*hp2-vu(iimax)-g/a*hu(iimax)+g*dtF*(Sf2-S0);
    A*vp2-AF(1)*v(1)-wun*(A-AF(1));
   rho*g*(hp2-0.5*D)*A-Ap(1)-rho*g*A*ha-rho*A*v(1)*(v(1)-vp2)+wun*rho*A*(v(1)-
vp2)];

df=J\ff;

vpm=vp2;
hpm=hp2;
wm=wun;

vp2=vp2-df(1);          hp2=hp2-df(2);          wun=wun-df(3);
resv=abs(vp2-vpm);    resh=abs(hp2-hpm);      resw=abs(wun-wm);
end
end
```